2010

Theoretical studies of H-passivated silicon nanowires, silicon surface systems and Si/Ge core/shell nanowires

Ning Lu
Iowa State University

Theoretical studies of H-passivated silicon nanowires, silicon surface systems and Si/Ge core/shell nanowires

by

Ning Lu

A dissertation submitted to the graduate faculty

in partial fulfillment of the requirements for the degree of

DOCTOR OF PHILOSOPHY

Major: Condensed Matter Physics

Program of Study Committee:
Kai-Ming Ho, Major Professor
Robert McQueeney
Adams Kaminski
Curtis Struck
Matthew Kramer

Iowa State University

Ames, Iowa

2010

Table of Contents

LIST OF TABLES

LIST OF FIGURES

Abstract

Global structural optimization with Genetic Algorithm and first principle analysis have been performed on the Silicon nanowires, Ag induced Si surface reconstruction systems and Si/Ge core/shell nanowires. By using genetic algorithm combined with ab-initio calculation, we determined the atomic structures H-passivated <110> and <112> silicon nanowires. we found that at certain values of the hydrogen chemical potential the nanowires can take relatively stable structures in <112> SiNWs with rectangular cross sections bounded by monohydride {110} and {111} facets with dihydride wire edges. In <110> SiNWs cross section of the nanowire evolves from chains of six-atom rings to fused pairs of such chains to hexagons bounded by {001} and {111} facets. Second, with the structural models of SiNWs, we further analyzed their electronic properties. We showed that the <112> SiNWs have an indirect to quasi-direct band gap transition with the increasing sizes and the band gap properties under uniaxial stress and different aspect ratios. Third, we did a Ag-induced Si(111) (rt3xrt3) and (3x1) surface reconstruction search with our variablenumber GA with ab-initio relaxation. The (rt3xrt3) global search found the Inequivalent Triangle (IET) structure as the lowest energy. A model of combination of pure Ag films and IET structure is proposed to explain the islands-to-holes ratio (R_{IH}) equals 3 situation observed in experiments. For the (3x1) reconstruction, a model with 2/3 ML Ag and 1Ml Si coverage has been found and it has lower surface energy than the widely accepted HCC model with only 1/3 ML Ag coverage. Finally, we did some DFT calculation on the Si/Ge and Ge/Si core/shell [112] nanowires. The charged localization inside the NWs reveals that the electrons and holes are seperated. The quantum confinement effect in the NWs is strongly modified by the band offsets. An indirect to quasi-direct band gap transition can be obtained with a compressive strain, and the depth of the quantum wells can be modulated by the aspect ratios.

Chapter 1. INTRODUCTION

Silicon is the most important materials in semiconductor industry. As nano-devices shrink in size, the conventional understanding of electronic devices are no longer applicable as quantum effects start to play an important role in the behavior of the devices. At the same time, when structures are approaching atomic scale, the precise fabrication by lithographic techniques, for example, are not even applicable. Very often, the fabrication of regular structures rely on self-assembly which is susceptible to fluctuations. Therefore, a deeper understanding to exploit the quantum behavior of nano-devices and precise control of building nano-structures are highly desired.

Naturally, physical systems tend to stay at their most stable states after thermal annealing. The most stable state is defined as the structure of a physical system that has the lowest total energy compared to all other possible structures. The physical properties of the systems could be derived theoretically from the structure with the lowest total energy. However, structural determination for a complex physical system is a big challenge. It would take years even decades of effort to determine the lowest energy structure of a complex system. Conventional methods of structural determination in theoretical studies create candidate structures manually relying on human intuition. Adopting a systematic global structural optimization is an alternative way to solve the problem. Among different global structural optimization methods, the genetic algorithm (GA) is one of the most efficient methods. Earlier successful applications of the genetic algorithm have been able to discover new low total energy structures for a number of atomic silicon clusters [1]. The properties of these isomers are calculated and compared well with the experimental data.

The total energy of a system can be calculated within the framework of first principle calculations. The answer to any given physical system can be obtained by solving the *Schrodinger*'s equations and calculating the total energy of that system. Density functional theory (DFT) [2] provides a framework for solving the Hamiltonian (*Schrodinger*'s equation) and calculating the total energy of realistic physical systems[5,6].

The correct match between theoretical predictions and experimental observations relies on the correct structure which is calculated theoretically using first-principles calculations. Scanning tunneling microscopy (STM) [3] invented by Binning, Rohrer, Gerber, and Weibel in 1982 is one of the experimental

techniques to study the surface by probing the electronic structure of a surface. The Nobel Prize was later awarded to Binning and Rohrer in 1986. The simulated STM images [4] derived from the calculated electronic structure of a correct surface topology should match the experimental STM images. In this dissertation, we apply the genetic algorithm (GA) technique to study several interesting problems in nanoscale systems of nanowires and surfaces reconstruction.

In Chapter 3, the use of a genetic algorithm to perform a global search of H-passivated Si nanowires will be presented. Si nanowires, possibly doped, can act as nanoscale devices or as interconnects. Si nanowires fabricated in experiments are mostly passivated by oxide or hydrogen, and nanowires with various diameters(as small as 1.3 nm) and different axis orientations can be made. However, theoretical prediction of the structure of Si nanowires are still at a beginning stage, and attempts being made are mostly based on manual construction without exploring the vast configurational space. Hence, we designed an efficient optimization procedure based on a genetic algorithm (GA) to investigate the structures of H-passivated Si nanowires with the axes along the <110> and <112> direction. The GA is coupled to a Si-H empirical potential which facilitates fast exploration of the configurational space, followed by structural refinements at the density functional theory level. We found that the structures of H-passivated Si nanowires are bulk-like down to sub-nanometer wire dimensions. In addition, we recognized several structural motifs of “magic” nanowires with chain-like and hexagonal-shaped cross sections in <110> SiNWs and rectangular cross sections in <112> direction. As the diameters of the SiNWs increase, the difficulty of global searching increases exponentially, so is the DFT calculations. We constructed the big size SiNWs in <110> ,<112> and <111> directions by using Wulff construction, giving us the same structural motif as the Genetic Algorithm (GA) in the lower sizes limit.

In Chapter 4, with the atomic geometries retrieved via global search using genetic algorithm in Chapter 3, we investigated the electronic properties of H-passivated <112> Si nanowires. We used first-principles calculations within density functional theory. We showed that <112> SiNWs have an indirect band gap in the ultrathin diameter regime, whereas the energy difference between the direct and indirect fundamental bandgaps progressively decreases as the wire size increases, indicating that larger [112] SiNWs could have a quasi-direct band gap. We further show that this quasi-direct gap feature can be

enhanced when applying uniaxial compressive stress along the wire axis. Moreover, our calculated results also reveal that the electronic band structure is sensitive to the change of the aspect ratio of the cross sections.

In Chapter 5, we did a global search with our variable number GA with ab-initio relaxation for Ag-induced Si(111) 3x1 and rt3xrt3 surface reconstruction. In the searching process every structure is precisely relaxed by the DFT. This GA-DFT can overcome the defects of the previous GA with empirical potentials. In the Ag/Si(111)-3x1 surface, a model with 2/3 ML Ag and 1Ml Si coverage has been found and it has lower surface energy than the widely accepted Honeycomb Chain (HCC) model with only 1/3 ML of Ag coverage. We also found the optimized HCC model with 1/3 ML Ag coverage as the 2^{nd} lowest energy structure. In the rt3xrt3 surface reconstruction, we presented all the structures with Ag and Si coverage varying from 1/3 ML to 2 ML. We found that the commonly known Inequivalent Triangle (IET) structure with 1 ML Ag and 1ML Si has the lowest surface energy, which agrees well with all experimental observations.

In Chapter 6, we presented our ab-initio calculations on 3 different Ag films: free standing, on a Si(111) bilayer substrate and on a Si (111) missing-top-layer substrate. Our studies show that the surface energy oscillates in free standing films with Ag layers, while it has a minimum value at 2 layers on Si (111) substrate.

In chapter 7, Strain-dependent electronic properties of [112] Ge/Si and Si/Ge core/shell NWs are studied using first-principles calculations within DFT. We show that the transition from indirect to quasi-direct gap can be obtained by applying compressive strain and the width of the band gap can be tuned by strain. The analysis of the projected density of states indicates that the quasi-direct gap is strongly influenced by the atoms in the {111} facets. Several possible applications have been discussed based on their distinguished electronic properties.

References for Chapter 1

[1] K. M. Ho, A. A. Shvartsburg, B. Pan, Z. Y. Lu, C. Z. Wang, J. G. Wacker, J. L. Eye, and M. F. Jarrold, Nature 392, 582 (1998).

[2] P. Hohenberg and W. Kohn, Phys. Rev. 136, B864 (1964); W. Kohn and L. J. Sham, Phys. Rev. 140, A1135 (1965).

[3] G. Binning, H. Rohrer, C. Gerber, and E. Weibel, Phys. Rev. Lett. 49, 57 (1982).

[4] J. Tersoff and D. R. Hamann, Phys. Rev. B 31, 805 (1985).

[5] P. Hohenberg and W. Kohn, Phys. Rev.B 136, 864(1964);

[6] W. Kohn and L. J. Sham, Phys. Rev.B 140, A1135(1965).

Chapter 2. CALCULATION METHODS

2.1 First-Principles Calculation

A many particles system that consists of atomic nuclei and electrons can be calculated precisely with the Born Oppenheimer (adiabatic) approximation. The nuclei are considered as fixed at their instantaneous positions when the electrons are estimated with quantum mechanics by Schrodinger equation. The electrons can be treated as a many body quantum system while the nuclei can be classical particles.

The Schrodinger equation of the many body problem can be expressed as below:

$$\left\{\sum_{i=1}^{N}\left[-\frac{h^2}{2m}\nabla^2 + v(\vec{r_i})\right] + \frac{1}{2}\sum_{i\neq j=1}^{N}\frac{e^2}{|\vec{r_i}-\vec{r_j}|}\right\}\varphi(\vec{r_i},..,\vec{r_N}) = E\ \varphi(\vec{r_i},..,\vec{r_N}) \quad (2.1)$$

The $\vec{r_i}$ is the position of ith electron, N is the total number of electrons, v is the external field, and E is the total electronic energy. As we can see, the equation (2.1) can not be solved in that it depends on 3N electrons coordinates. However in 1964, Hohenberg and Kohn [1] proved that the electroni density ρ(r) of the ground state determines uniquely the external potential v so that uniquely determines the ground state properties. In 1965 , Kohn and Sham [2] showed that it is possible to approximate the many-electron energy functional by an equivalent set of one-electron equations with an appropriate choice of the exchangecorrelation potential to model the many-electron interaction, and the set of equation can be solved self-consistently. Under this approach, the total energy can be written as

$$E = E_K + E_H + E_{XC} + E_{ion\text{-}e} + E_{ion\text{-}ion} \quad (2.2)$$

In eq(2.2) above, E_K is the kinetic energy, E_H is the Hartree electron-electron energy, E_{XC} is the exchange correlation, $E_{ion\text{-}e}$ is the ion-electron interaction, and $E_{ion\text{-}ion}$ is the ion-ion iteraction energy.

E_{XC} is the function of electron density ρ(r), but the form is unknown. Under local density approximation (LDA) the exchange correlation energy E_{xc} can be expressed as below, considering the slowly varying density system as uniform electron gas system locally.

$$E_{XC} = \int \epsilon_{XC}(\rho)\rho(\vec{r})d\vec{r} \quad (2.3)$$

Where $\varepsilon_{xc}(\rho)$ is the exchange correlation energy per electron of a uniform electron gas with density ρ. The variation of ρ(r) is neglected in this approximation. The generalized gradient approximation(GGA) can be used which takes into account the gradient of the electron density in addition to the local electron density.

The Kohn Sham equation is still impossible to solve without the eigen wave functions. Therefore the wave functions are usually expanded in the basis of plane wave functions. As in almost all cases the physical properties are determined by the valence electrons instead of core electrons, pseudopotential is introduced to model the interaction between valence electrons and cores. The pesudopotential requires much less plane wave basis functions and hence makes the computation significantly faster. By using pseudopotentials the computation costs are dramaticaly reduced [5,6]. A useful detailed review of the total energy pseudopotential method can be found in article by Payne, Teter, Allan, Arias, and Joannopoulos [7].

2.2 Empirical potential for Silicon

A very popular empirical potential for semiconductors (for example C, Si and Ge) is the Tersoff potential [3,4]. It is written as a pairwise sum of interaction energy between atom i and j with a Morse-like form:

$$E = \frac{1}{2}\sum_{i,j\neq i} fc(\tau_{ij})(Aexp\,(-\lambda_1 r_{ij}) - B_{ij}exp(-\lambda_2 r_{ij})) \qquad (2.4)$$

Where fc is a cut-off function in which the interaction between two atoms is zero beyond certain chosen cut-off distance. The first term in Eq. (2.4) is repulsive, which represents repulsion due to the Pauli principle or orthogonalization, and the second term is the attractive part due to bonding. The parameter B_{ij} depends on the environment around the atoms i and j, for example bond length, bond angles and bond order. Although the Tersoff potential form is pairwise, it is in fact implicitly beyond two-body through the parameters, and hence it can be fitted to describe open structures like semiconductor crystal. The parametrization can be extended to include multi-component systems in which the parameters A and B_{ij} not only depend on the coordinates of the atoms, but also on the types of atoms.

2.3 Genetic Algorithm

Genetic algorithm (GA) has been successfully used in global structural optimizations of 0-dimension systems such as C60 [8] and silicon clusters [9], 1-dimension systems like silicon nanowires [10,11] , and 2-dimension systems like silicon surfaces [12]. The genetic algorithm used in present study is applied for 1D and 2D systems. The procedures are described as follows: In generation zero, a population pool of certain structures are generated by means of putting *n* atoms randomly in a simulation cubic box with a appropriate length. The structures are relaxed to their local minima with the conjugate gradient or steepest descent method.

In each subsequent generation, a mating process is used to generate some new structures. Then, those new structures are relaxed to their nearest local minima. The population pool is updated if the newly relaxed structures have energies lower than those in the pool and their structures are not identical to any one inside the population pool. The structural optimizations with a genetic algorithm were proceeded up to hundreds and thousands of generations. Finally, the energetically favorable structures retained in the population pool are further optimized using first-principle total energy calculations if the relaxation was calculated with Tight-binding or other empirical potentials. In some cases, we used first-principle calculations for each newly generated structure in every generation.

In the mating operation, both parents A and B are randomly rotated about their centers of mass which are set to be the origin. Then, by simply cutting the parents structures through a random plane and permuting the lower-halves of the parent structures A and B, two new offspring structures C and D can be created. If the number of atoms in the new structure does not match that in the parent, parents A and B are shifted in order to achieve the correct number of atoms. In the present study, two structures from the population pool are picked as parents and a child structure is generated by mating lower-half of parent A with upper-half of parent B. In order to maintain the diversity in the population pool, it is crucial to have a structural comparison algorithm when updating the population pool.

References of Chapter 2

[1] P. Hohenberg and W. Kohn, Phys. Rev.B 136, 864 (1964).

[2] W Kohn and LJ Sham, Phys. Rev. B **140,** A1135(1965).

[3] J. Tersoff and D. R. Hamann, Phys. Rev. B 31, 805 (1985).

[4] J. Tersoff, Phys. Rev. Lett., **56,** 632(1986).

[5] J. C. Phillips, Phys. Rev. 112, 685 (1958).

[6] M. L. Cohen and V. Heine, Solid State Physics, 24, 37 (1970)

[7] M. C. Payne, M. P. Teter, D. C. Allan, T. A. Arias, and J. D. Joannopoulos, Reviews of Modern Physics, 64, 1045 (1992).

[8] D. M. Deaven and K. M. Ho, Phys. Rev. Lett. 75, 288 (1995)

[9] K. M. Ho, A. A. Shvartsburg, B. Pan, Z. Y. Lu, C. Z. Wang, J. G. Wacker, J. L. Eye, and M. F. Jarrold, Nature 392, 582 (1998).

[10] N Lu, C Ciobanu, T.L. Chan, F.C. Chuang, C.Z Wang and K.M. Ho, J. Phys. Chem. C 111,7933 (2007)

[11] T.L. Chan, C Ciobanu, F.C Chuang, N Lu, C.Z. Wang and K.M. Ho, Nano Lett 6, 277 (2006)

[12] F.C. Chuang, C Ciobanu, V.B. Shenoy, C.Z Wang and K.M. Ho, Surf. Sci. 573, 375 (2004)

Chapter 3. GLOBAL SEARCH FOR H-PASSIVATED SILICON NANOWIRES STRUCTURAL MODELS

This chapter consists of two parts. The first part 3.1 is our paper *The structure of ultrathin H-passivated [112] Silicon nanowires* published on Journal of Physical Chemistry C, 2007, 111, 7933, by Ning Lu, Cristian Ciobanu, Tzu-liang Chan, Feng-Chuan Chuang, Cai-zhuang Wang and Kai-Ming Ho. I did the major contribution to this work, including doing the genetic algorithm (GA) search with empirical potentials, verified the final structures with DFT calculation, making the simulated STM images and structural motifs conclusion. The second part 3.2 is our another paper *Magic structures of H-passivated <110> silicon nanowires* published on Nano Letters, 2006,6,277, written by Tzu-Liang Chan, Cristian Ciobanu, Feng-Chuan Chuang, Ning Lu, Cai-Zhuang Wang and Kai-Ming Ho. I did the work of verifying the accuracy of Hansen-Vogle empirical potential by comparing it with DFT calculations and conducting DFT calculations to verify the final structures.

3.1 The structures of ultrathin H-passivated [112] Silicon nanowires

3.1.1 Introduction

In recent years, the fundamental and technological efforts toward viable uses of nanostructures have markedly switched from carbon nanotubes to semiconductor nanowires, as the latter allow for a more diverse range of structures and, hopefully, for more control over their properties. Fervent strides are underway to synthesize nanoscale wires for nanoelectronics applications [1] because of the realization that such wires can operate both as nanoscale devices and as the leads that connect them. [2] Silicon nanowires (SiNWs) offer, in addition to their appeal as building blocks for nanoscale devices, the benefit of simple fabrication techniques compatible with the currently well-developed silicon technology.

Currently, the widely used methods of synthesis [3-6] can produce SiNWs with diameters ranging from several tens of nanometers down to 1 nm. The SiNWs are usually crystalline with a prismatic shape bounded by facets that are parallel to the axis of the wire. [4-8] While remarkable progress has been achieved on the front of synthesis and characterization, atomic-scale structural information remains

necessary for a better understanding of the physics and potential applications of SiNWs. At small diameters, the resolution of scanning probing microscopy techniques may not be sufficient to unambiguously identify the positions of the atoms at the surface of the wire. Moreover, the current theoretical approaches do not routinely rely on exhaustive searches of the configuration space of nanowires for two reasons: (i) global search methodologies for quasi one-dimensional structures are not widely developed and used, and (ii) any global search method requires inexpensive ways to evaluate the energy of the system, which come in the form of empirical potentials. The empirical potentials may not always have sufficient accuracy to capture subtler wire configurations with similar energies and different structures. Therefore, numerous recent studies rely on heuristically proposed NW structures as a starting point for stability studies of SiNWs at the ab initio level. [9-14] Because the experimental techniques to date yield wires that are passivated either with oxides [15,16] or with hydrogen, [6,7] theoretical studies have recently started to address the structure and properties of hydrogenated nanowires. [17-23]

Experimental work by D.D.D. Ma et al. [6] has revealed that ultrathin nanowires with effective diameters [24] in the range of 1 to 7 nm can be produced by HF etching of the oxide sheath that covers the wire after the oxide-assisted growth procedure. Although the HF-etching process is initially dominated by kinetics, at the end of it the wire remains virtually free of surface defects and has facets with low-energy orientations. This observation has enabled us to simulate the formation of the ultrathin H-passivated [110] SiNWs through a process of minimization of the formation energy per atom, with results [23] that were strikingly close to the experimental ones. [6]

Here, we investigate the low-energy structures of hydrogenated ultrathin nanowires oriented along the [112] direction. We focus on the shape evolution of the cross-section as the number of Si atoms per length increases, and we also assess the influence of the hydrogen environment on the cross-sectional shape. For hydrogen environments where monohydride terminations are favorable, we have found (via global configuration search) that the cross-sections of the stable or metastable wires are perfectly rectangular. However, the aspect ratio of the rectangles is not that given by the thermodynamic Wulff construction, which predicts that the distance from the wire axis to any given facet is strictly proportional to the surface energy of that facet orientation. [25] The structures corresponding to relatively deep local minima of the

formation energy are called magic structures and are characterized by monohydride-facetted [112] wires with complete (111) bilayers. These magic NW structures have certain specific numbers of Si atoms, called magic numbers. When the number of Si atoms per wire length is increased, the length of the (111) bilayers grows first, before additional bilayers are formed. We have also found that variations in the chemical potential of hydrogen trigger changes in the wire shape and facet terminations, as well as in the relative energetics of the local minima of the formation energy per silicon atom.

3.1.2 Genetic Algorithm Methods

To search for nanowire structures with low formation energies, we have employed a genetic algorithm (GA) because this methodology has proved to be versatile and efficient for a variety of silicon-based low-dimensional systems [23,26] The SiNWs are modeled using a supercell that is periodic in one dimension with the periodic length along the wire set according to experimental reports.[6] We have chosen the Hansel−Vogl (HV) interatomic potential because the HV model reproduces well the energies of hydrogenated phases of the Si(001) surface.[27] The global optimization procedure has been recently put forth in ref 29, and we will only briefly describe it below.

During a GA optimization run, a pool of at least 60 structures is evolved by performing genetic operations (cross-overs). For this nanowire system, the crossover operation consists in randomly selecting two structures (parents) from the pool, cutting them with the same plane parallel to the wire axis, then combining parts of the parents that lie on the opposite sides on the cutting plane to create a new structure (child). The new structure is then fully passivated with H atoms and relaxed using the HV interatomic potential. [33] We include the child structure in the genetic pool based on its formation energy *f*, defined as

$$f = (E - \mu_H n_H)/n - \mu \qquad (3.1)$$

where E is the total energy of the supercell with n Si atoms and n_H hydrogen atoms, μ is the (reference) bulk cohesive energy of Si in the diamond phase, and μ_H is the chemical potential of hydrogen. The (variable) number of H atoms is determined by the requirement of having complete passivation of the wire surface, but n is kept fixed during the crossover operations by rejecting any child that has a different number of Si atoms than its parents.

The H chemical potential (μ_H) at the empirical interactions level [33] is chosen such that the experimentally relevant passivation reactions at surfaces are thermodynamically possible during the optimization. This means that μ_H is set such that certain hydrogenated surfaces have lower energies than the surface energies of the same orientations prior to the considered hydrogenation reaction. Guided by experiments, [6] we focus only on two surface orientations, Si(111) and Si(110), and determine the range of H chemical potentials for which the following reactions are thermodynamically allowed: (a) formation of monohydride Si(111) from clean, unreconstructed Si(111), (b) formation of monohydride Si(110) from clean Si(110), and (c) formation of trihydride Si(111) from monohydride Si(111). The ranges of allowable μ_H (at the HV level) for each of these three reactions are shown in Figure 3.1a. Within the μ_H range that is common to all three reactions, we choose two values (Figure 3.1a) that are close to the lower bound of μ_H, because this choice readily ensures (i) that the desired hydrogenation reactions are all allowed, and (ii) that the calculations are as far away as possible from the total etching regime in which the system could decompose in silane or disilane.

The genetic pool is divided into two equal subsets, corresponding to the two chosen values μ_H (Figure 3.1a). The crossover operations are performed both with parents in the same subset and with parents in different subsets, to ensure a superior sampling of the potential energy landscape. The genetic operation is carried out 15 times during a generation, and a typical GA run has 50000 generations. At the end of each run, all structures in the pool are relaxed using the VASP software;[28,29] this is a well-developed, broadly used package and, as such, it may ensure that the results presented here could be more widely reproduced. The chemical potential μ_H that we have used for computing the density functional theory (DFT) formation energies was determined by maximizing the correlation with the HV formation energies for 235 configurations of [112] H-passivated SiNWs [refer to Figure 3.1(b)]. A least-squares fit through the 235 data points yields the relation $f_{DFT} = f_{HV} - \delta$ between the formation energies at the DFT and HV levels, where $\delta = 0.1$ eV/atom. Because of this simple relationship, in Figure 3.1b we have shown the difference $f_{HV} - \delta$ on the horizontal axis, rather than showing f_{HV}. While some energetic reordering occurs upon performing the DFT calculations, most of the low- energy structures found with the HV potential remain relevant at the DFT level, which gives confidence in the combined GA−DFT approach used here.

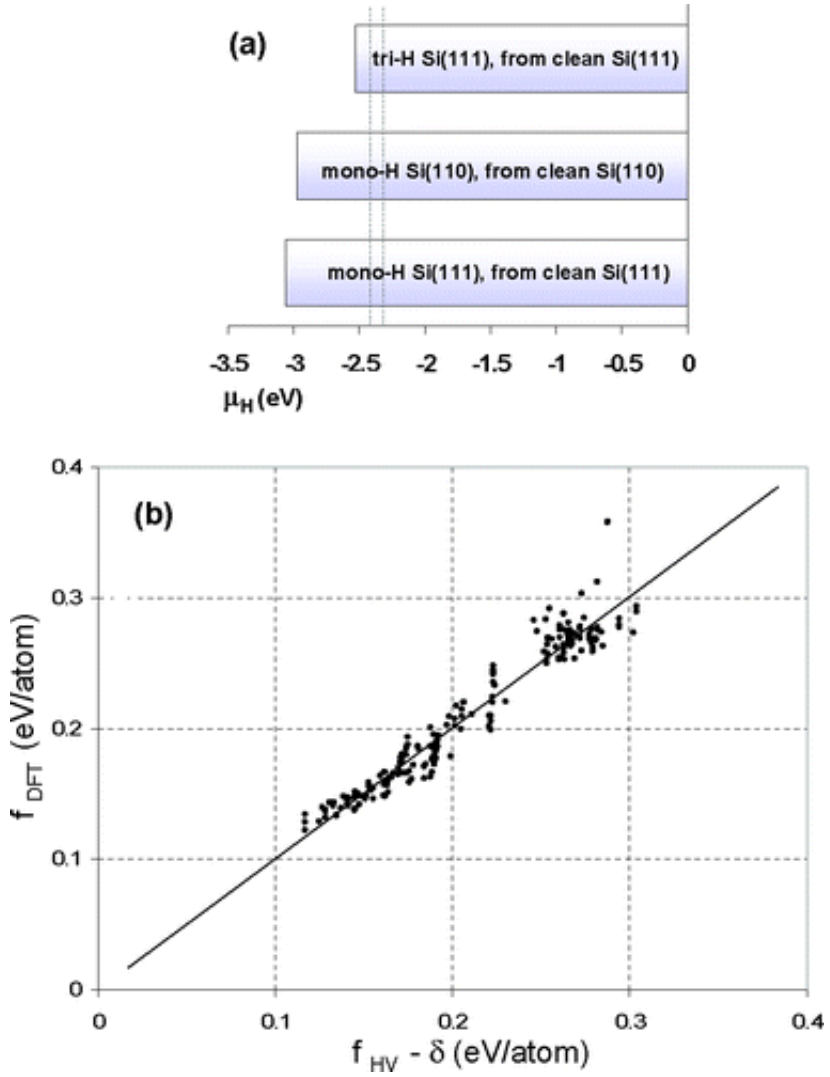

Figure 3.1 (a) Allowable HV chemical potential ranges for the three relevant hydrogenation reactions described in text. Two μ_H values ($\mu_H = -2.42$ eV and $\mu_H = -2.32$ eV, vertical dash lines) have been chosen close to the lower bound of the common μ_H range where all three passivation reactions are thermodynamically allowed. (b) DFT formation energies[28] (f_{DFT}) of 235 H-passivated [112] SiNWs plotted versus the HV formation energies corresponding to $\mu_H = -2.42$ eV. A least-squares fit yields $f_{DFT} = f_{HV} - \delta$ (where $\delta = 0.1$ eV/atom) for a DFT chemical potential of $\mu_H = -3.48$ eV.

3.1.3 Structural models from global search

The structures found to have the lowest formation energy (eq 1) after the combined GA optimization and DFT relaxation are shown in Figure 3.2a,b for $16 \leq n \leq 30$ and for H chemical potentials of $\mu_H = -3.48$ and -3.38 eV, respectively. As can be seen in Figure 3.2, the two subsets of the genetic pool corresponding to the two H chemical potential values retrieved mostly different structures at each number n of Si atoms per unit cell. This result is markedly different from the one obtained for [110]-oriented nanowires,[23] where the best structures retrieved for even n values were the same for the small μ_H variation (0.1 eV) considered and where the odd-n structures differed only in the position of one peripheric atom.

At the lower chemical potential ($\mu_H = -3.48$ eV), the nanowires tend to have 90^o edges whenever the number of atoms n allows, with the most stable wire having perfectly rectangular cross sections. For example, at $n = 16$ the atoms arrange themselves so that they form a rectangle with (111) facets that are longer than its (110) facets. The aspect ratio of the rectangle is not solely dictated by the ratio of surface energies as would be expected from the Wulff construction [25] but is strongly affected by the presence of dihydride corners and by the small number of atoms that prevents the formation of large (110) facets. As the number of atoms is increased, the extra atoms dispose themselves around the $n = 16$ core in such a way as to increase the length of the full (111) mono-H facets first (i.e., growth in the [110] direction). After $n = 24$, the wire also begins to grow along the [111] direction as the larger n can accommodate wider (110) facets to minimize the overall formation energy. The first perfect rectangle with more than two (111) planes (complete bilayer structures) appears at $n = 30$, as seen in Figure 3.2a.

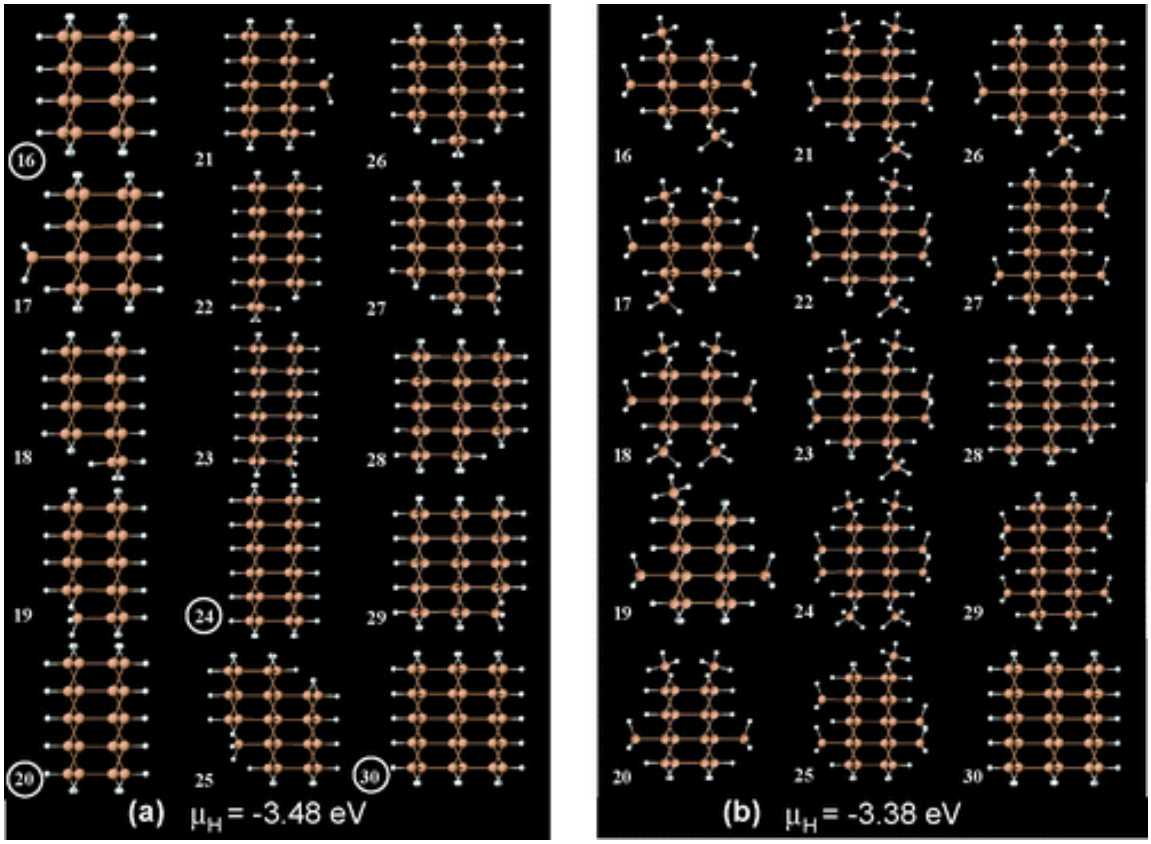

Figure 3.2 Nanowire structures (axial view along the [112] direction) with n = 16−30 silicon atoms per unit cell and H DFT chemical potential values of $\mu_H = -3.48$ eV (a) and $\mu_H = -3.38$ eV (b), found to have the lowest formation energy per atom (eq 1) after the genetic algorithm optimization and subsequent DFT relaxations. The H atoms are the smaller white spheres. The values n that correspond to magic nanowires (i.e., structures that correspond to pronounced local minima of the formation energy per atom) are circled.

For the larger H chemical potential ($\mu_H = -3.38$ eV), there is no clear preferential growth pattern, and we have not found any particularly stable structures. At this chemical potential, there are more trihydride species on the wires leading to a variety of floppy structures (e.g., the surface of the nanowire with $n = 18$). The existence of many such structures with very similar energies prevents the emergence of a systematic or clear evolution pattern of the cross section of the wire. While in Figure 3.2a for $n > 24$ the wires tend to form three complete (111) bilayers with mono-H coverage, in the case of $\mu_H = -3.38$ eV (Figure 3.2b) the (111) facets are covered by a mixture of trihydrides and monohydrides that results in a variety of NW structures that have incomplete (111) layers.

The formation energy f of the most stable structures that we found for $16 \leq n \leq 30$ is plotted in Figure 3.3 as a function of n. When trihydrides are strongly disfavored ($\mu_H = -3.48$ eV), the formation energy displays clear local minima at $n = 16$, 20, 24, and 30 with the structures identified in Figure 3.2a. These local minima structures have rectangular cross-sections, are fully covered in monohydrides, and their facet edges consist of dihydrides (SiH_2). Because of their relatively low-formation energies, we may call these structures magic nanowires. In the ultrathin regime, the aspect ratio of the cross-section of the magic wires does not vary monotonically (as can be seen by inspecting Figure 3.2a) but settles at the value predicted by the surface energy ratio[25] in the limit of a very large number of atoms n (i.e., for thick nanowires). At the higher value of μ_H, the formation energy does not display pronounced local minima (Figure 3.3). The two minima located at $n = 21$ and $n = 27$ do not have symmetric structures, and they are not deep minima either. The $\mu_H = -3.38$ eV structures displayed as insets at $n = 18$, 24, and 30 are symmetric but are not local minima (Figure 3.3).

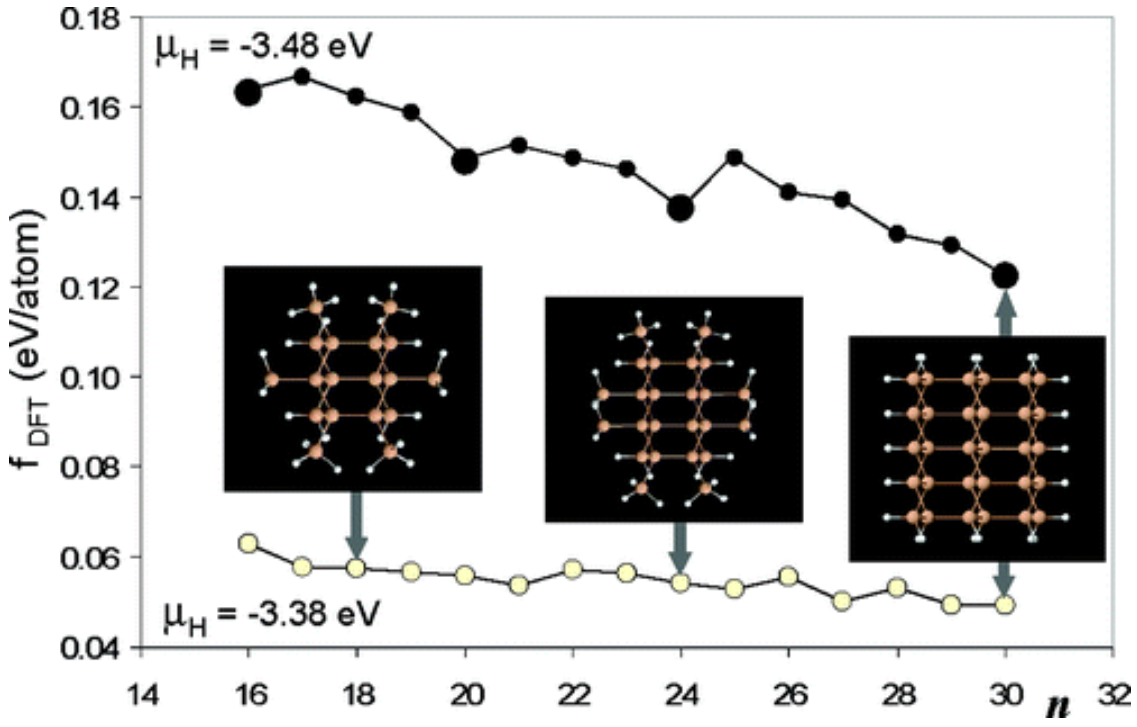

Figure 3.3 DFT formation energies for two values of the H chemical potential $\mu_H = -3.48$ eV (solid dots) and $\mu_H = -3.38$ eV (open circles), plotted as a function of the number n of Si atoms. When mostly monohydrides cover the nanowire surface, the formation energy displays several pronounced local minima (large solid dots on the $\mu_H = -3.48$ eV curve) at n = 16, 20, 24, and 30 (magic numbers). If a significant amount of trihydrides are formed (which happens for $\mu_H = -3.38$ eV), then deep minima of the formation energies do not occur; in this case, the much smaller variations of the formation energy are due to a large number of competing configurations with both mono- and trihydrides on the surface. The insets show that even structures with clear spatial symmetry do not give local minima on the $\mu_H = -3.38$ eV formation energy curve.

We have therefore evidenced that a (slight) change in μ_H can have a large effect on the wire structure in that it can determine whether magic structures could be identified or not. The higher H chemical potential ($\mu_H = -3.38$ eV) does not yield magic structures because the trihydrides on the (111) facets are able to relax in the vicinity of monohydrides and dihydride edges, thus allowing for numerous low-energy combinations of SiH_x species on the wire surface. In contrast, for $\mu_H = -3.48$ eV the surface energy of the tri-H/Si(111) surface is very high (more than twice the value corresponding to mono-H/Si(111) surfaces) because of the larger absolute value of the chemical potential and irrespective of the relaxation of the trihydrides. By this reasoning, we should be able to tune μ_H to values that render the monohydride (111) surfaces completely unfavorable. We tested μ_H values of −3.28 eV and higher and have found that the trihydrides indeed become the preferred species on the (111) wire facets.

The above discussion has focused on whether or not we can observe magic nanowires for different chemical potentials μ_H, and we identifyed rectangular wires with (110) and (111) facets. The (111) facets can be covered by mono or trihydrides for the most favorable structures at $\mu_H = -3.48$ and −3.28 eV, respectively. These types of wires have simple geometries, characterized by the number of N of (110) layers and the number M of complete (111) bilayers (Figure 3.4). In the trihydride case, there are $(M - 1)$ complete bilayers inside the wire plus one-half of a bilayer on each of the two (111) facets that bound the wire and are subject to passivation (Figure 3.4b). The total number of Si atoms and the number of hydrides of each kind for rectangular nanowires made of complete bilayers are summarized in Table 3.1.

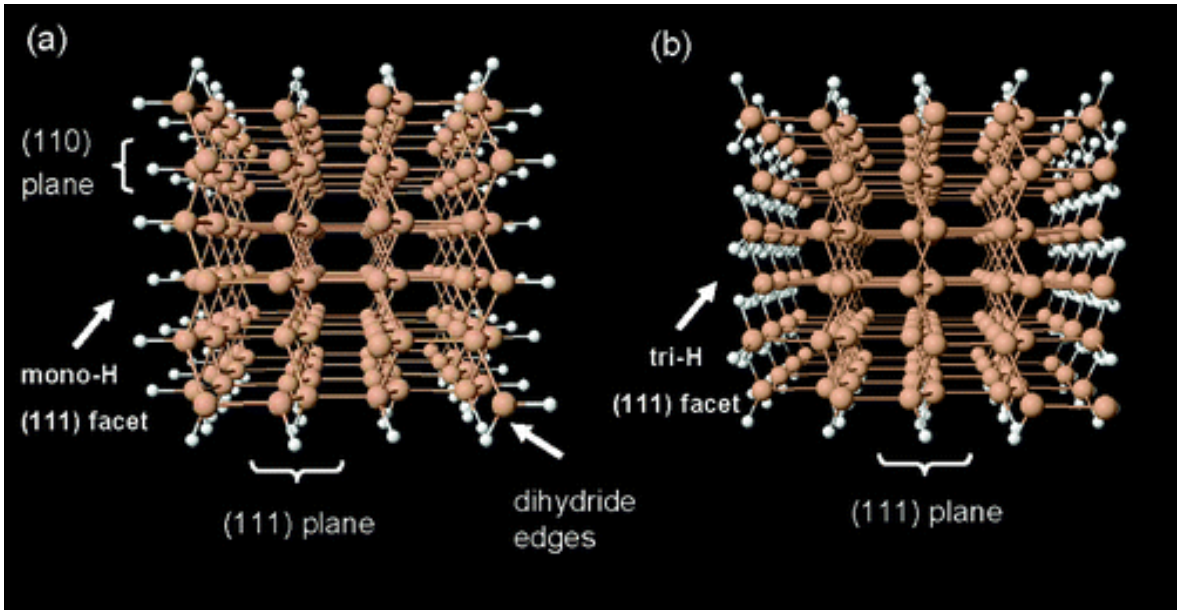

Figure 3.4 Perspective view along the axis of [112] H-passivated Si nanowires with monohydride (a) and trihydride (b) (111) facets. The (110)-type facets are covered with monohydrides in both cases. The nanowires shown (a,b) correspond to N = 6 planes parallel to (110), and M = 4 complete (111) bilayers. The trihydride-terminated wire (b) has one-half of a complete bilayer on each of the two (111) nanofacets. Structures of the type (a) have been identified as magic (refer to text and to Figures 2 and 3).

Table 3.1: Constituents of the [112] Hydrogenated Si Nanowires with Perfectly Rectangular Cross Sections Made of N (110)-oriented Planes and M (111) Planes (complete Bilayers).

structure	Si atoms, n	mono-H	di-H	tri-H
Figure 4a	$2NM$	$2(N+M-2)$	4	0
Figure 4b	$2NM$	$2(M-1)$	0	$2N$

In the recent experiments [6] on H-passivated [112] SiNWs with diameters of 2 nm, the (111) facets are passivated with trihydrides, which correspond to low-energy structures found for chemical potentials μ_H greater than −3.28 eV in our simulations (refer to Figure 3.4b and Table 3.1). To our knowledge, passivated [112] SiNWs that have monohydride (111) facets have not been reported so far. The results of the global optimization presented here (Figures 3.2 and 3.3) indicate that the magic structures with mono-H/Si(111) should be experimentally observable, perhaps under different conditions than those reported in ref 12. The pioneering work of Higashi et al.[31] in the field of aqueous HF etching of silicon surfaces reported perfect mono-H coverage of Si(111) wafers, thus lending strong support to the above prediction of monohydride-facetted [112] nanowires.

In the diameter regime addressed here, the surface passivation (mono versus trihydride) can very likely have a strong effect on the electronic properties, because the number of atoms that are passivated is relatively large. The actual trends exhibited by structure, stability, band gap, and conductivity of [112] H-SiNWs as functions of the degree of hydrogenation are yet to be explored, as is the sensitivity of these trends with respect to possible random defects (vacancies) in the mono or trihydride coverage pattern. At equal areal density of missing hydrogen atoms, we would naturally expect the monohydride-terminated surfaces to be more sensitive to the presence of H-vacancies because a missing H atom in a monohydride-terminated wire generates a highly reactive Si site on the surface. Finally, we note that low levels of the H coverage can determine surface reconstructions (Si−Si bonding), whose energetics are determined, at least in certain μ_H regimes, by the number of passivated bonds per surface area.[32]

An interesting issue to address is whether one can create experimentally wires with a preset or controlled aspect ratio of the cross-section. The reason why this might be of interest is that in the ultrathin diameter regime where most of the atoms are at the surface, the interplay between the relative numbers of atoms on the (111) and (110) surfaces and their degree of H-passivation is likely to result in new (and

perhaps useful) ways to control the band structure and optical properties of the nanowires. For example, the extent of band gap and band structure variations with the aspect ratio taken (at constant effective wire diameter) is still unknown and is likely be addressed in the near future. If experimental conditions could be achieved so as to favor thermodynamics over the kinetics of the H-passivation process, the results presented here indicate that in such conditions the aspect ratios of the [112] Si NWs are determined only by the number of silicon atoms per unit length (cross-sectional area) and the effective H chemical potential attained in experimental conditions. On the other hand, because thermodynamics is not the only factor influencing the wire formation process we may expect to see broad distributions of aspect ratios, possibly with frequency distribution peaks located at ratios that correspond to the magic structures shown in Figure 3.2a. Because the few reported statistics on nanowires concern the effective wire diameters in relation to their growth direction [7,8] but do not address the aspect ratio, we believe it would be very interesting to pursue studies that can shed more light on the aspect ratio distributions of ultrathin hydrogenated nanowires of different diameters and axis orientations.

References of Chapter 3.1

[1] Appell, D. *Nature* (London) **2002**, *419*, 553.

[2] Cui Y.; Lieber, C. M. *Science* **2001**, *291*, 851.

[3] Morales A. M.; Lieber, C. M. *Science* **1998**, *269*, 208.

[4] Zhang, R. Q.; Lifshitz, Y.; Lee, S. T. *Adv. Mater.* **2003**, *15*, 635.

[5] Holmes, J. D.; Johnston, K. P.; Doty, R. C.; Korgel, B. A. *Science* **2000**, *287*, 1471.

[6] Ma, D. D. D.; Lee, C. S.; Au, F. C. K.; Tong, S. Y.; Lee, S. T. *Science* **2003**, *299*, 1874.

[7] Wu, Y.; Cui, Y.; Huynh, L.; Barrelet, C. J.; Bell, D. C.; Lieber, C. M. *Nano Lett*. **2004**, *4*, 433.

[8] Schmidt, V.; Senz, S.; and Gösele, U. *Nano Lett.* **2005**, *5*, 931.

[9] Menon M.; and Richter, E. *Phys. Rev. Lett*. **1999**, *83*, 792.

[10] Zhao Y.; Yakobson, B. I. *Phys. Rev. Lett.* **2003**, *91*, 035501.

[11] Bai, J.; Zeng, X. C.; Tanaka, H.; Zeng, J. Y. *Proc. Natl. Acad. Sci. U.S.A.* **2004**, *101*, 2664.

[12] Rurali R.; Lorente, N. *Phys. Rev. Lett.* **2005**, *94*, 026805.

[13] Kagimura, R.; Nunes, R. W.; Chacham, H. *Phys. Rev. Lett.* **2005**, *95*, 115502.

[14] Cao, J. X.; Gong, X. G.; Zhong, J. Z.; Wu, R. Q. *Phys. Rev. Lett.* **2006**, *97*, 136105.

[15] Cui, Y.; Gudiksen, L. J.; Wang, M. S.; Lieber, C. M. *Appl. Phys. Lett*. **2001**, *78*, 2214.

[16] Wang, N.; Tang, Y. H.; Zhang, Y. F.; Lee, C. S.; Bello, I.; Lee, S. T. *Chem. Phys. Lett.* **1999**, *299*, 237.

[17] Zhang, R. Q.; Lifshitz, Y.; Ma, D. D. D.; Zhao, Y. L. Frauenheim, Th.; Lee, S. T.; Tong, S. Y. *J. Chem. Phys.* **2005**, *123*, 144703.

[18] Beckman, S. P.; Han, J. X.; Chelikowsky, J. R. *Phys. Rev. B* **2006,** *74*, 165314.

[19] Singh, A. K.; Kumar, V.; Note, R.; Kawazoe, Y. *Nano Lett.* **2006**, *6*, 920.

[20] Tang Z.; Aluru, N. R. *Phys. Rev. B* **2006**, *74*, 235441.

[21] Jing, M. W.; Ni, M.; Song, W.; Lu, J.; Gao, Z. X.; Lai, L.; Mei, W. N.; Yu, D. P.; Ye, H. Q.; Wang, L. *J. Phys. Chem. B* **2006**, *110*, 18332.

[22] Zhao, X.; Wei, C. M.; Yang, L.; Chou, M. Y. *Phys. Rev. Lett*. **2004**, *92*, 236805.

[23] Chan, T. L.; Ciobanu, C. V.; Chuang, F. C.; Lu, N.; Wang, C. Z.; Ho, K. M. *Nano Lett.* **2006**, *6*, 277.

[24] The effective diameter is defined here as the diameter of the thinnest cylinder that includes all the silicon atoms of the wire.

[25] Pimpinelli A.; Villain, J. *Physics of Crystal Growth*; Cambridge University Press: New York, 1998; Chapter 3.

[26] (a) Ho, K. M.; Shvartsburg, A. A.; Pan, B. C.; Lu, Z. Y.; Wang, C. Z.; Wacker, J.; Fye, J. L.; Jarrold, M. F. *Nature* **1998**, *392*, 582.

(b) Chuang, F. C.; Ciobanu, C. V.; Shenoy, V. B.; Wang, C. Z.; Ho, K. M. *Surf. Sci.* **2004**, *573*, L375.

(c) Ge, Y. B.; Head, J. D. *J. Phys. Chem. B*. **2004**, *108*, 6025.

(d) Chakraborty, N.; Prasad, R. *Bull. Mater. Sci.* **2003**, *26*, 127.

[27] Hansen U.; Vogl, P. *Phys. Rev. B* **1998,** *57,* 13295.

[28] (a) VIENNA ab initio simulation package (VASP); Universität Wien, 1999.

(b) Kresse G.; Hafner, J. *Phys. Rev. B* **1993**, *47*, R558.

(c) Kresse G.; Furthmüller, J. *Phys. Rev. B* **1996**, *54*, 11169.

[29] The ab initio calculations are performed within the generalized gradient approximation.The kinetic energy cutoff is set at 11 Ry, and the Brillouin zone is sampled using 16 *k*-points. The SiNW is positioned at the center of a supercell with a vacuum space of 12 Å separating the periodic images of the wires. Each SiNW structure is relaxed until the magnitude of the force an any atom is smaller than 0.01 eV/Å.

[30]Perdew, J. P. In *Electronic Structure of Solids '91*; Ziesche, P., Eschrig, H., Eds.; Akademie-Verlag: Berlin, 1991.

[31] Higashi, G. S.; Chabal, Y. J.; Trucks, G. W.; and Raghavachari, K. *Appl. Phys. Lett.* **1990,** *56*, 656**.**

[32] Ciobanu C. V.; and Briggs, R. M. *Appl. Phys. Lett.* **2006,** *88*, 133125**.**

3.2 Magic Structures of H-Passivated <110> Silicon Nanowires

3.2.1 Introduction

The continuous miniaturization in the electronics industry has reached the limit in which the interconnection of the devices in a reliable and controllable way is particularly challenging. Fervent strides are underway in the preparation of nanoscale wires for molecular and nanoelectronics applications: [1] such wires (possibly doped or functionalized) can operate both as nanoscale devices and as interconnects. [2] Silicon nanowires (SiNW) offer, in addition to their appeal as building blocks for nanoscale electronics, the benefit of simple fabrication techniques compatible with the currently well-developed silicon technology.

The current growth methods (e.g., refs 41-44) can yield wires with diameters ranging from several tens of nanometers down to 1 nm. These SiNWs are usually crystalline with only a few axis orientations observed and have a prismatic shape bounded by facets that are parallel to the wire axis [4-8] While remarkable progress has been achieved in terms of preparation and characterization of SiNWs, atomic-level knowledge of the structure remains necessary for a complete understanding the device properties of these wires. At present, attempts to predict the structure of SiNWs are affected by the lack of robust methodologies (i.e., algorithms coupled with model interactions) for searching the configuration space, and most studies to date rely on heuristically proposed structures as the starting point for stability studies of SiNWs at the ab initio level. Electronic structure calculations are too computationally demanding to be used in a thorough sampling of the potential energy surface of SiNWs. On the other hand, most of the empirical potentials for Si are fast but are not sufficiently transferable to capture accurately the structure and energetics of various wire configurations. Despite these obstacles, the current theoretical efforts to find the structure of SiNWs have been very vigorous and have lead to the identification of a number of low-energy configurations for pristine SiNWs. [9-13] In comparison, the structure of passivated nanowires has received much less attention from a theoretical perspective, although most of the experimental techniques to date yield wires that are passivated either with oxides [14,15] or with hydrogen. [6,7]

3.2.2 Genetic Algorithm calculation methods

Motivated by the scanning tunneling microscopy (STM) experiments of Ma et al., [6] we have investigated the structure of thin H-passivated nanowires oriented along the [110] direction. To this end, we have designed a robust and efficient optimization procedure based on a genetic algorithm (GA), followed by structural refinements at the density functional theory (DFT) level. We have found that in the presence of hydrogen, the silicon atoms of the nanowire can maintain their bulklike bonding environment down to sub-nanometer wire dimensions. Furthermore, our calculations reveal that, as the number of atoms per length is increased, there emerge three distinct types of wire configurations with low formation energies (magic wires). Two of these structures have a platelike aspect in cross section, which have not been observed so far. The third one has a hexagonal section, which is consistent with recent experiments for Si and Ge wires [6,16] Given their extremely small diameters, the magic structures found here by the combined GA-DFT optimization procedure cannot be predicted by thermodynamic considerations based on the Wulff construction. [17] The procedure described below is generally applicable for finding the structure of any ultrathin nanowire provided that suitable models for the atomic interactions are available and that the spatial periodicity along the wire axis is known.

The choice of GA for the present work was motivated by previous findings that search procedures inspired by the genetic evolution can successfully be used to determine the structure of Si clusters [18] and surfaces.[19,20] The SiNW are modeled using a supercell that is periodic in one dimension, with the period set according to experiments.[6] We choose the Hansel−Vogel (HV) potential to describe the atomic interactions, for this model has been shown to reproduce well the energies of hydrogenated phases of the Si(001) surface. [21]

The algorithm for SiNW optimization is similar to that which we recently designed for high-index Si surfaces,[19] so we focus here on the departures from ref 57. During a GA optimization run, a pool of at least 60 structures (which are initially just random collections of atoms) is evolved by performing mating operations; such operations consist in selecting two random structures (parents) from the pool, cutting them

with the same plane parallel to the wire axis, and then combining parts of the parent structures that lie on the opposite sides on the cutting plane to create a new structure (child). [19] The child structure is passivated by satisfying all its dangling bonds with H atoms and then relaxed with the HV model. [21] We include the child structure in the genetic pool based on its formation energy *f* defined in eq (3.1) as where *E* is the total energy of the computational cell with *n* silicon atoms (*n* is kept fixed during a GA run) and n_H hydrogen atoms, μ is the (reference) bulk cohesive energy of Si in its diamond structure, and μ_H is the chemical potential of hydrogen. The H chemical potential is set such that certain hydrogenation reactions at surfaces are thermodynamically possible. These reactions are shown in Figure 3.1a, along with our two chosen values for μ_H. The pool is divided into two equal subsets, one for each value of μ_H. The mating operations are performed both with parents in the same subset and with parents in different subsets, to ensure a superior sampling of the potential energy landscape. The mating is carried out 15 times during a generation, and a typical GA run has 50000 generations. At the end of each run, all structures are relaxed using the VASP package.[22,23] The chemical potential μ_H used to compute DFT formation energies is determined so that it maximizes the correlation with the HV formation energies for a few hundred configurations (refer to Figure 3.1b). Therefore, while some energetic reordering does occur after the DFT calculations, most of the low-energy structures found with the HV model remain relevant at the DFT level, especially in the range of DFT formation energies below 0.15 eV/per atom.

3.2.3 <110> Si nanowires structural motifs

The most stable structures (DFT level) that we found through the above procedure using $\mu_H = -3.45$ eV are shown in Figure 3.5 for different numbers of Si atoms in the range $10 \leq n \leq 30$. The second half of the genetic pool (corresponding to $\mu_H = -3.35$ eV (DFT)) retrieved the same structures for all even values of *n*. In the case of odd *n*, the two sides of the pool found structures that are different only in the position of one peripheral Si atom. As Figure 3.5 reveals, the GA-DFT optimization finds stable structures that are made of six-atom rings (viewed along the SiNW axis), with some of the rings incomplete depending on the value of *n*. The six rings can arrange themselves in chains (e.g., $n = 12$, $n = 16$ in Figure

3.5); for $n > 16$ the rings form fused pairs of such chains (n = 18, 24, 30), which we call double chains. Structures similar to the double chains shown in Figure 3.5 have also been considered in recent studies of quantum confinement in SiNWs. [63]The formation energy of the most stable structures for $10 \leq n \leq 30$ retrieved is plotted in Figure 3.6 as a function of n. When the value of n increases, the formation energy assumes an overall decreasing trend while displaying odd−even oscillations. The relatively larger formation energy of the odd-n structures corresponds to configurations where one Si atom protrudes from the surface of the wires, thus creating a somewhat unfavorable bonding environment.

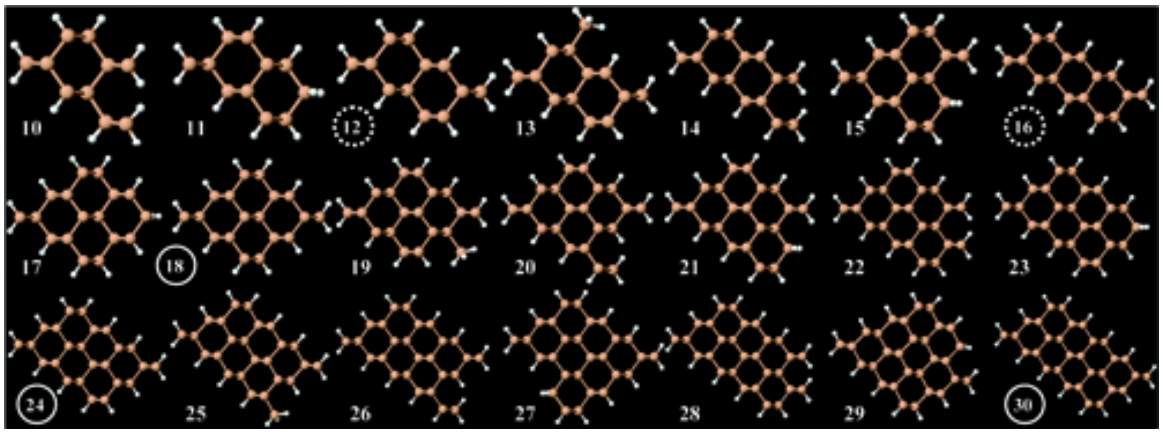

Figure 3.5 Nanowire structures (axial view) with n = 10 to n = 30 silicon atoms per unit cell, found after genetic algorithm optimizations and the subsequent DFT relaxations. The H atoms are the smaller white spheres. The values n that correspond to magic wires are indicated by dashed and solid circles for chain and double-chain SiNWs, respectively.

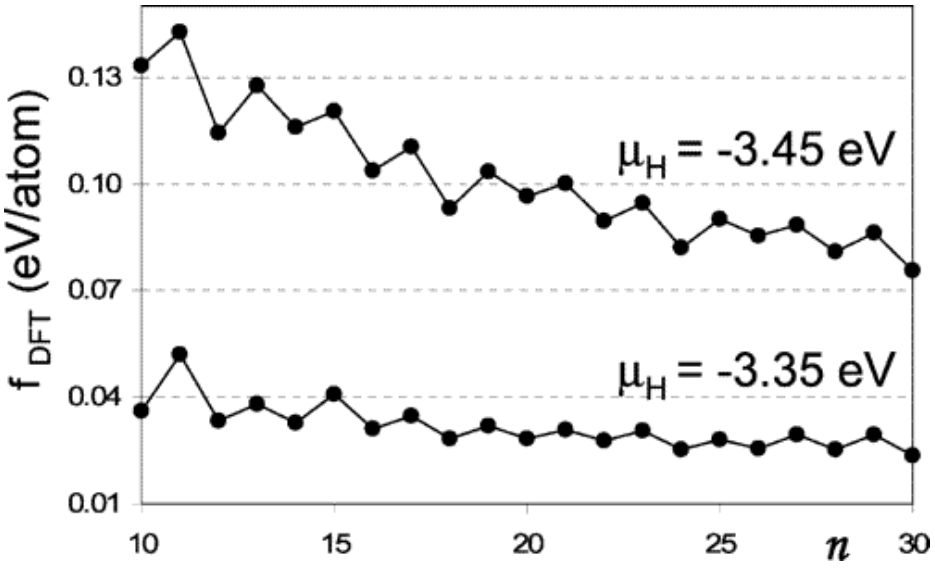

Figure 3.6 DFT formation energies per Si atom for two values of the H chemical potential, plotted as a function of n. Structures with even n are local minima at both the empirical [21] and ab initio [22] levels.

As shown in Figure 3.5, the ground state for each n has a bulklike structure with no significant reconstructions. The absence of reconstruction is due to the hydrogen environment at chemical potentials μ_H that favor no less than five hydrogenation reactions (refer to Figure 3.1). The use of smaller μ_H values can lead to understanding the interplay between reconstruction and hydrogen coverage on the SiNW facets, an investigation which we will address in subsequent studies. For smaller values of n ($n < 17$), the common motif present in lowest energy structures is the six-atom ring. When chains of complete six-atoms rings are formed, the structures become particularly stable, as is the case of $n = 12$ and $n = 16$ SiNWs, which are made of $R = 2$ and $R = 3$ complete rings, respectively. The six-atom ring chains expose two {111} facets with monohydride terminations. Another common feature of all (complete) chain structures is the presence of two dihydridres with the SiH_2 planes oriented perpendicular to the wire axis. For $n > 17$, the most favorable structures are the double chains described above (and illustrated in Figure 3.5), whose building blocks we call double rings. These blocks are readily identifiable in the case of $n = 18$, 24, and 30, which correspond to a number of $D = 2$, 3, and 4 full double rings (respectively). The double chains expose a total of four {111} nanofacets which form parallelogram-shaped SiNW cross sections. The complete double chains also contain two dihydrides, identical to those capping the chain SiNWs.

We have conducted further optimization studies for $n > 30$ using, however, only even atom numbers n. We found that starting at $n = 60$, structures with hexagonal cross section becomes stable over the double-chain SiNWs described above. Even the smallest hexagonal SiNW ($n = 28$) has a formation energy that is only slightly higher (by 0.005 eV/atom) than that of the double chain with the nearest size ($n = 30$). The hexagonal wires are bounded by two {001} and four {111} facets and can be described by their number of completed concentric layers L of six-atom rings. Due to the relative stability and structural closure of the chain, double-chain, and hexagonal SiNWs, we name these configurations *magic*. The shapes of prototype magic SiNWs are illustrated in Figure 3.7, and a description of their building blocks and numbers of atoms is summarized in Table 3.2. The formation energies of magic SiNWs were separately plotted as a function of n in Figure 3.7 at both levels of theory. [21,22] The plot reflects the structural trends described above, namely, the transition between chain and double chain at $n = 16$ and the transition between double-chain

and hexagonal SiNWs, which starts at $n \sim 29$. It should be noted that *incomplete* hexagons appear frequently in the range $28 < n < 60$; therefore the latter shape transition is not as well defined as the former.

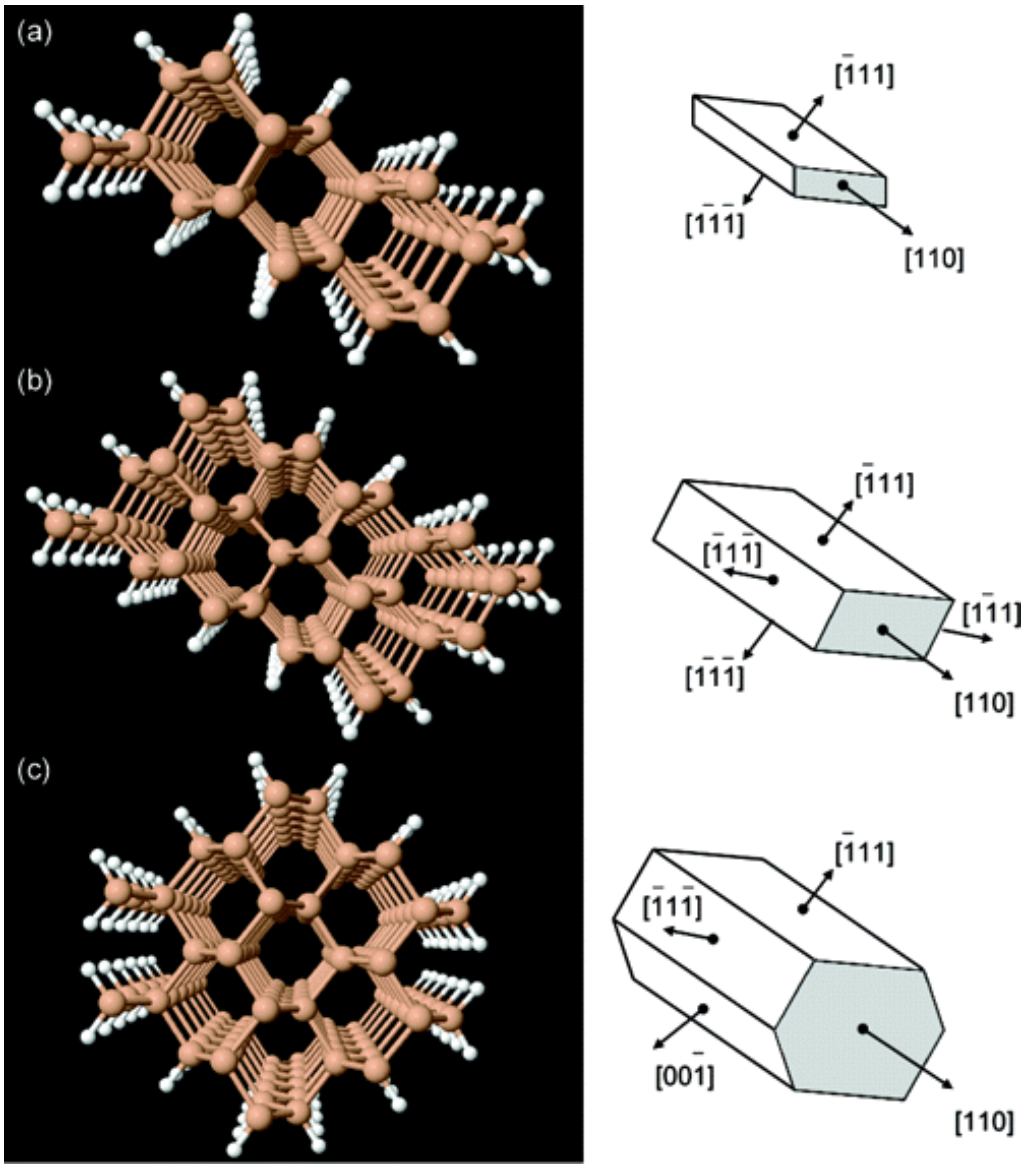

Figure 3.7 Magic nanowires (perspective view) found as minima of the formation energy per atom. The chain (a) and double chain (b) are characterized by the number of complete six-atom rings *R* and double rings *D*, respectively (also refer to Table 3.2). The configurations with hexagonal cross section have a number *L* of full concentric layers ($L = 2$ in panel (c) above) of six rings and are consistent with recent observations of H-passivated SiNWs.[44,45] The facet orientations of magic wires are shown on the right.

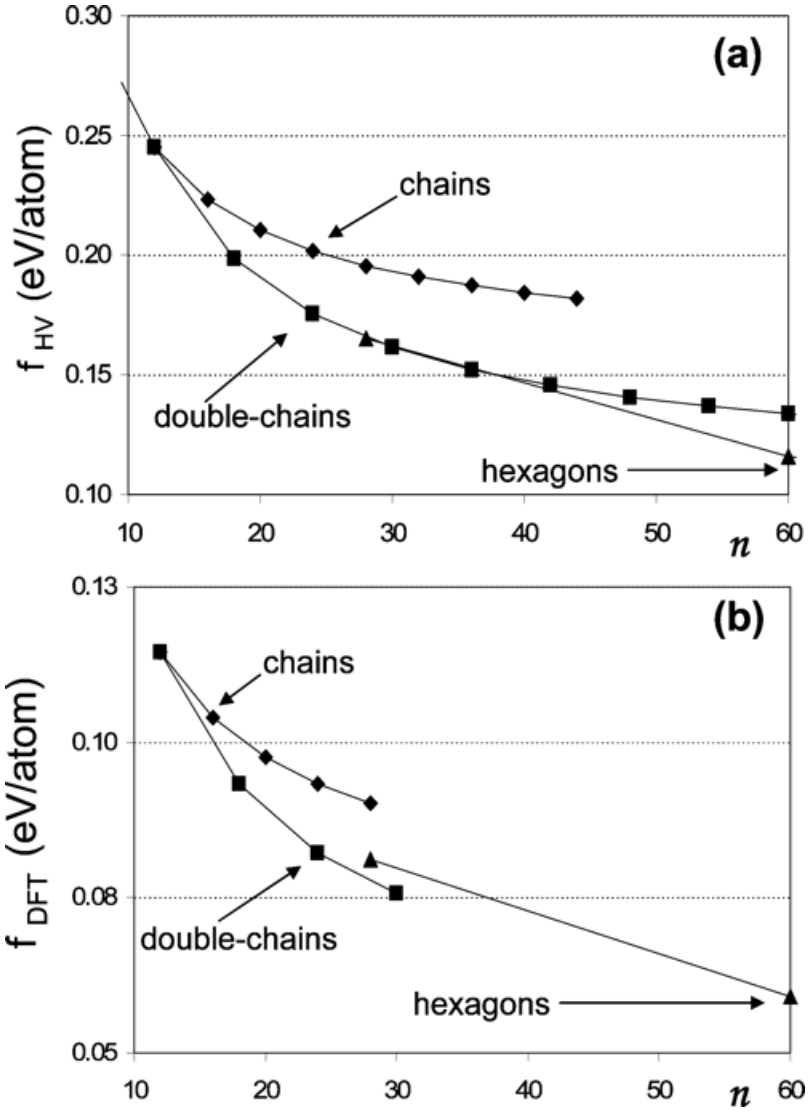

Figure 3.8 Formation energies per Si atom computed for specific structures of the H-passivated [110] nanowires: chain (diamonds), double chain (squares), and hexagonal (triangles up), computed at the level of HV potential[21] with $\mu_H = -2.42$ eV (a) and of DFT calculations [22] with $\mu_H = -3.45$ eV (b).

Table 3.2 Building Blocks and Magic Numbers (n) of Si Atoms Corresponding to the Different Types of Low-Energy SiNWs Found in the Global Optimization. The last two columns show the number of mono- and dihydrides in each case.

structure	building units	n	mono-H	di-H
chain	rings, R	$4(R+1)$	$2(R+1)$	2
double chain	double rings, D	$6(D+1)$	$2(D+2)$	2
hexagon	layers, L	$2L(3L+1)$	$4L$	$2L$

We note that even in the absence of reconstruction, the shape of SiNWs (refer to Figure 3.7) departs markedly from the equilibrium crystal shape predicted by the constrained minimization[17] of the overall surface energy. The reason for this departure is that the number of surface Si atoms is larger than, or comparable to, the number of bulklike atoms (refer to Table 3.2). For the chain and double-chain SiNWs, the polygonal shape itself is not preserved as only two or four facets are exposed instead of the expected six.[6,7] For the ultrathin hexagonal wires, the departure from the Wulff construction [17] is more subtle. Although the cross section is hexagonal, the relative size of the {100} and {111} facets is not predicted by the surface energies because the interactions of facet edges are significant for wires thinner than 2 nm.

To our knowledge, chain and double-chain wires have not been observed so far for SiNWs, perhaps because the diameters achieved in the laboratory are larger than those which are favorable for platelike structures to form.[6] Recent experiments were successful in isolating and characterizing [110] SiNWs with hexagonal section and diameters between 1.3 and 7 nm.[6] The thinnest hexagonal wire in our work (L = 2 in Table 3.2) has a diameter of approximately 1.2 nm, as estimated by the distance between its {001} facets. The first hexagonal wire that we find to be more stable than any double-chain magic wire is about 1.8 nm in diameter, i.e., already in the range of the experimentally reported hexagonal SiNWs.[6] Pursuing further the comparison between the hexagonal wires found here and those in ref 44, we have computed STM images for the facets of the L = 5 hexagon. The simulated images are shown in Figure 3.9a

for a {111} facet covered with monohydride and for a {001} facet covered with dihydride. Our calculations are in agreement with the STM experiments, which also showed the exclusive presence of dihydride species on the {001} facets of [110] SiNWs. Furthermore, the resemblance (Figure 3.9) between the simulated STM image and the experimental one brings strong support to the predictive power of the theoretical methodology presented here.

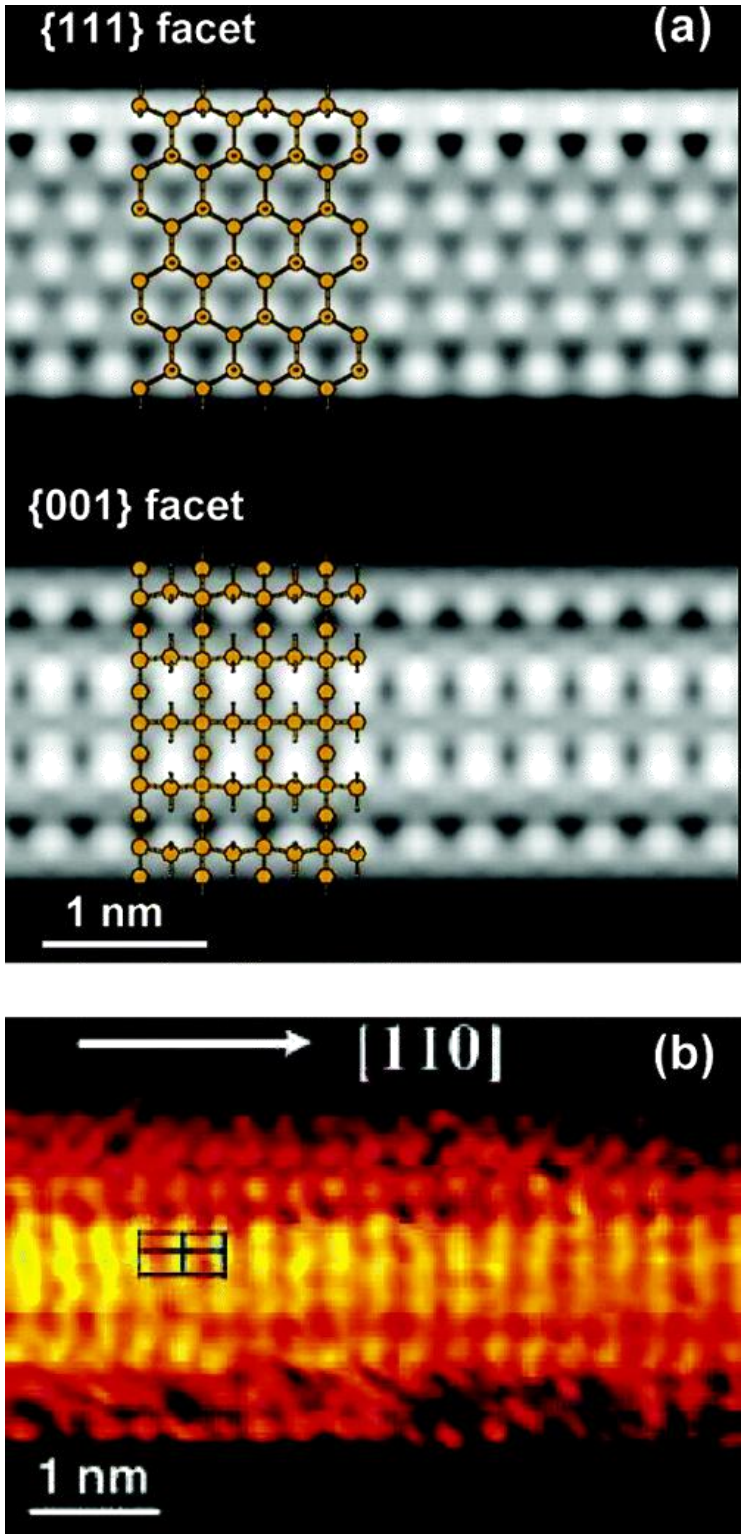

Figure 3.9 Simulated empty-state STM images (bias of +2.0 V) of {111} and {001} facets of an $L = 5$ hexagonal nanowire. (b) Actual STM image of a {001} facet (from ref 6) taken at the same bias voltage.

3.2.4 Conclusion

In conclusion, we described a combined GA-DFT procedure to search for the structure of [110] passivated SiNWs and presented our results for [110] nanowires with up to 60 atoms per unit cell. Subject to the availability of reasonable empirical potentials, this GA-DFT procedure can be adapted quite readily for finding the structure of any type of nanowire that exhibits atomic-scale periodicity along its axis. For H-passivated [110] silicon wires, the genetic search revealed three types of magic structures (shown in Figure 3.7), chain, double-chain, and hexagonal SiNWs. Our results for hexagonal wires are consistent with recent experiments.[6] Given this agreement with experiments at diameters larger than 1.8 nm, it is conceivable that the chain and double-chain structures proposed here can be observed experimentally upon pursuing the preparation of SiNWs thinner than 1.3 nm.

References of Chapter 3.2

(1) Appell, D. *Nature* (*London*) **2002**, *419*, 553.

(2) Cui, Y.; Lieber, C. M. *Science* **2001**, *291*, 851 .

(3) Morales, A. M.; Lieber, C. M. *Science* **1998**, *269*, 208.

(4) Zhang, R.-Q.; Lifshitz, Y.; Lee, S.-T. *Ad*V. *Mater.* **2003**, *15*, 635.

(5) Holmes, J. D.; Johnston, K. P.; Doty, R. C.; Korgel, B. A. *Science* **2000**, *287*, 1471.

(6) Ma, D. D. D.; Lee, C. S.; Au, F. C. K.; Tong, S. Y.; Lee, S. T. *Science* **2003**, *299*, 1874.

(7) Wu, Y.; Cui, Y.; Huynh, L.; Barrelet, C. J.; Bell, D. C.; Lieber, C.M. *Nano Lett.* **2004**, *4*, 433.

(8) Schmidt, V.; Senz, S.; Go ̈sele, U. *Nano Lett.* **2005**, *5*, 931.

(9) Menon, M.; Richter, E. *Phys. Re*V. *Lett* **1999**, *83*, 792.

(10) Zhao, Y.; Yakobson, B. I. *Phys. Re*V. *Lett.* **2003**, *91*, 035501.

(11) Bai, J.; Zeng, X. C.; Tanaka, H.; Zeng, J. Y. *Proc. Natl. Acad. Sci. U.S.A.* **2004**, *101*, 2664.

(12) Rurali, R.; Lorente, N. *Phys. Re*V. *Lett.* **2005**, *94*, 026805.

(13) Kagimura, R.; Nunes, R. W.; Chacham, H. *Phys. Re*V. *Lett.* **2005**, *95*, 115502.

(14) Cui, Y.; Gudiksen, L. J.; Wang, M. S.; Lieber, C. M. *Appl. Phys. Lett.* **2001**, *78*, 2214.

(15) Wang, N.; Tang, Y. H.; Zhang, Y. F.; Lee, C. S.; Bello, I.; Lee, S.T. *Chem. Phys. Lett.* **1999**, *299*, 237.

(16) Hanrath, T.; Korgel, B. A. *Small* **2005**, *1*, 717 .

(17) Refer to, e.g.: Pimpinelli, A.; Villain, J. *Physics of crystal growth*; Cambridge University Press: Cambridge, 1998; Chapter 3.

(18) Ho, K. M.; Shvartsburg, A. A.; Pan, B. C.; Lu, Z. Y.; Wang, C. Z.; Wacker, J.; Fye, J. L.; Jarrold, M. F. *Nature* **1998**, *392*, 582.

(19) Chuang, F. C.; Ciobanu, C. V.; Shenoy, V. B.; Wang, C. Z.; Ho, K. M. *Surf. Sci.* **2004**, *573*, L375.

(20) Chuang, F. C.; Ciobanu, C. V.; Predescu, C.; Wang, C. Z.; Ho, K. M. *Surf. Sci.* **2005**, *578*, 183.

(21) Hansen, U.; Vogl, P. *Phys. Re*V. *B* **1998**, *57*, 13295.

(22) VIENNA ab initio simulation package, Technische Universita ̈t Wien,1999; Kresse, G.; Hafner, J. *Phys. Re*v. *B* **1993**, *47*, R558; Kresse, G.; Furthmuller, J. *Phys. Re*V. *B* **1996**, *54*, 11169.

(23) The ab initio calculations are performed within the generalized gradient approximation.24 The kinetic energy cutoff is set at 11 Ry, and the Brillouin zone is sampled using 16 *k* points. The SiNW is positioned at the center of a supercell with a vacuum space of 12 Å separating the periodic images of the wires. Each SiNW structure is relaxed until the magnitude of the force on any atom is smaller than 0.01 eV/Å.

(24) Perdew, J. P. In *Electronic Structure of Solids '91*; Ziesche, P., Eschrig, H., Eds.; Akademie-Verlag: Berlin, 1991.

(25) Zhao, X.; Wei, C. M.; Yang, L.; Chou, M. Y. *Phys. Re*V. *Lett.* **2004**, *92*, 236805. NL0522633

Chapter 4. SIZE AND STRAIN DEPENDENT ELECTRONIC STRUCTURES IN H-PASSIVATED [112] SILLICON NANOWIRES

This chapter is our paper *Size and Strain Dependent Electronic Structures in H-Passivated Si [112] Nanowires* published on Journal of Physical Chemistry C, 2008,112, 15680, by Li Huang, Ning Lu, Jia-An Yan, M.Y. Chou, Cai-Zhuang Wang and Kai-Ming Ho. In this work I did the ab-initio calculation for the electronic properties of [112] Si nanowires and observed the relationship between the size and strain to the band gaps. Jia-An Yan and Mei-Yin Chou from Georgia Institute of Technology did some DFT calculation with GW corrections and provided all the data that marked with GW.

4.1 Introduction

Si nanowires (SiNWs) have attracted great attention as they could be one of the most promising building blocks for future nanoscale devices due to their compatibility with currently well developed Si-based technology. Recent experimental results have already demonstrated applications of SiNWs as electrical devices, including field-effect transistors,[1-3] p−n junctions,[4] and chemical and biological sensors.[5,6] This wide range of applications can be achieved because of their novel electronic and optical properties arising from the quantum confinement, which allows for modifications by precise control of the wire structures and stoichiometries during synthesis and manufacturing processes, for example, the thickness, crystal orientation, surface passivation, and doping.

A detailed understanding of the electronic properties of SiNWs and the various possible ways to modify it are of primary importance to the development of new applications. It could be extremely difficult to get this information from experiments. To our knowledge, so far only one experimental work has been reported on the study of the orientation and diameter dependence of the electronic band gap of SiNWs.[7]

However, the interpretation of the experimental observations is still up for some debate and needs further verification from calculations. A number of computational studies have been devoted to address the structure−property relationship in hydrogenated SiNWs, mostly on [001], [110], and [111] oriented NWs,[8-14] whereas much less attention has been paid to [112] SiNWs, [15, 16] although most of the experimental measurements of the electronic band gap are available for this growth orientation. Moreover, almost all previous studies just used heuristically proposed NW structures as a starting point.

Recently, we have employed a genetic algorithm (GA) approach [17] combined with density functional theory (DFT) calculations to determine the structures of ultrathin H-passivated SiNWs oriented along the [112] directions. [18,19] We found that the cross sections of the [112] SiNWs are perfectly rectangular bounded by monohydrated {110} and {111} facets with dihydride edges. The aspect ratio of the cross section of the magic wire geometries retrieved by the GA-DFT optimization procedure in the ultrathin diameter regime cannot be predicted by the thermodynamic considerations based on the Wulff construction.[20]

4.2 First principle calculation methods for electronic properties

In this paper, we focus our investigation on the modification of electronic properties of H-passivated SiNWs oriented along the [112] direction. We study, using first-principles calculations, (1) how the electronic structures evolve as the number of atoms per unit length increases with diameters ranging from subnanometer to 3 nm, (2) the effects of the uniaxial strain along the wire axis on its band structure, and (3) how the electronic band structure responds to the change of the aspect ratio of the cross section of SiNWs.

Our calculations are carried out using the VASP code[21] based on DFT with ultrasoft pseudopotenitals[22] and plane-wave basis sets. The exchange-correlation functional is treated within the

local density approximation (LDA). The energy cutoff for plane waves is set equal to 19 Ry. One primitive unit cell of the wire is used to create an effectively infinite wire by periodic repetition of this unit cell along the wire axis. More than 18 Å vacuum space is used in lateral directions to avoid any interactions between the image NWs in neighboring cells. Five Monkhorst−Pack[23] *k* points are used to sample the essentially one-dimension Brillouin zone along the wire axial direction. The atomic positions and lattice parameters along the wire axis are then fully optimized with no symmetry constraints until the forces on each atom become less than 0.01 eV/Å, and the total energy converged to the order of 10^{-4} eV per cell. Tests have been performed to make sure that all of the results are fully converged with respect to the energy cutoff, *k*-point sampling, and vacuum spacing.

As is well-known, the conventional DFT-LDA calculations suffer from the systematic underestimation of the band gap. In this work, the LDA gaps at the Γ point in two thinnest SiNWs are therefore rectified by using the many-body perturbation method based on the *GW* approximation,[14] which is highly computationally intensive, especially for larger diameter wires. The technical details of the *GW* calculations can be found in ref [14]. The *GW* corrections increase the gap to the approximately correct value. Nevertheless, the general trend of the band gap variation as a function of the wire size and the energy dispersion close to the gap region are reliably reproduced by the DFT-LDA calculations.[25]

Following our previous work in ref [19], the geometry of [112] SiNWs are characterized by the number of (110) layers (*M*) and the number of complete (111) bilayers (*N*). Here we denote this as an (*M*,*N*) wire. Shown as an example in Figure 4.1 is the top and side views of the geometric structure of the (7,3) wire. In Table 4.1, we summarize the diameters and stoichiometries of the selected magic wires retrieved by the global genetic search. The diameter of each (*M*,*N*) wire is determined by $d = 2(A/\pi)^{1/2}$, where *A* is the area of the rectangular cross section of the H-passivated SiNWs. As can been seen in Table 4.1, the aspect ratio ($M \times d_{110}$:$N \times d_{111}$) of the cross-section of the magic wires does not vary monotonically in the ultrathin diameter regime, and is not given by the thermodynamic Wulff construction,[19] which predicts that the distance from the wire axis to any given facet is strictly proportional to the surface energy of the facet orientation. Band structure calculations are then performed for these fully relaxed geometries.

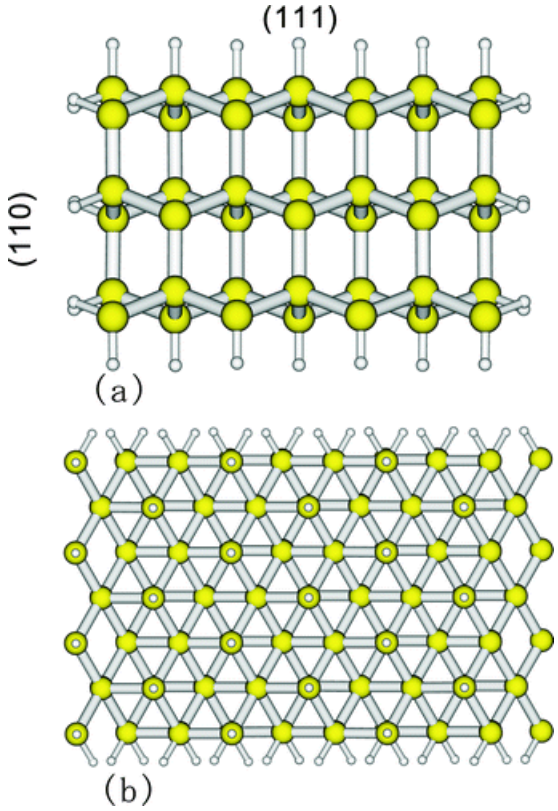

Figure 4.1. (a) Top view and (b) side view of the (7,3) SiNW, corresponding to $M = 7$ planes parallel to (110) and $N = 3$ complete (111) bilayers. Passivating hydrogen atoms are shown by small spheres.

Table 4.1. Diameter (d, in nm) and the Number of Si and H Atoms in the Unit Cell for the [112] SiNWs Obtained by a Global Genetic Search and Investigated in This Work

(M,N)	d	Si	H	(M,N)	d	Si	H
(4, 2)	0.85	16	16	(9, 4)	1.73	72	34
(5, 2)	0.95	20	18	(8, 5)	1.81	80	36
(6, 2)	1.03	24	20	(10,5)	2.02	100	40
(5, 3)	1.14	30	22	(11,5)	2.12	110	42
(7, 3)	1.34	42	26	(10,6)	2.21	120	44
(7, 4)	1.53	56	30	(12,7)	2.60	164	52
(8, 4)	1.63	64	32	(14,8)	2.98	224	60

4.3 Results and discussion

Several typical band structures for the [112] SiNWs are shown in Figure 4.2. The overall features of the band structure for the other wires investigated are quite similar. The energy dispersion near the gap region of [112] SiNWs is characterized by the well-resolved valence band maximum (VBM) at the Γ point and the conduction band minimum (CBM) near the *Z* point (zone edge), leading to an indirect nature of the band gaps. This is in sharp contrast to the band gaps of [100], [110], and [111] SiNWs, all of which exhibit a transition to direct band gaps in the same diameter regime.[13,14,28] A projected band structure from the bulk is also shown for comparison. When the bulk bands are projected along the [112] direction, quite a few high-symmetry points are projected to the center of the one-dimensional Brillouin zone, including *X*, *L*, *K*, *W*, and *U*. Other *L* and *X* points are projected to the zone boundary *Z*. It turns out the six conduction band minima are projected to two different locations in the one-dimensional Billouin zone [see Figure 4.2f]. When the rectangular wires are formed, confinement effects are different for the two sides, raising one minimum more than the other, but the feature of an indirect band gap remains.

Figure 4.3 shows the size dependence of the direct and indirect band gaps, together with the *GW*-corrected direct band gaps for the (4,2) and (5,2) wire. As expected from the quantum confinement effect, the band gap generally decreases with increasing wire size. The *GW* corrections for the two thinnest [112] wires turn out to be 2.17 eV (= 5.16−2.99) and 2.14 eV (= 4.80−2.66), respectively. These are much larger than that found in the bulk, which is about 0.5 eV (= 1.08−0.58). This finding thus supports our previous observations in SiNWs grown in other orientations that the self-energy correction is strongly enhanced with decreasing wire size.[13,14]

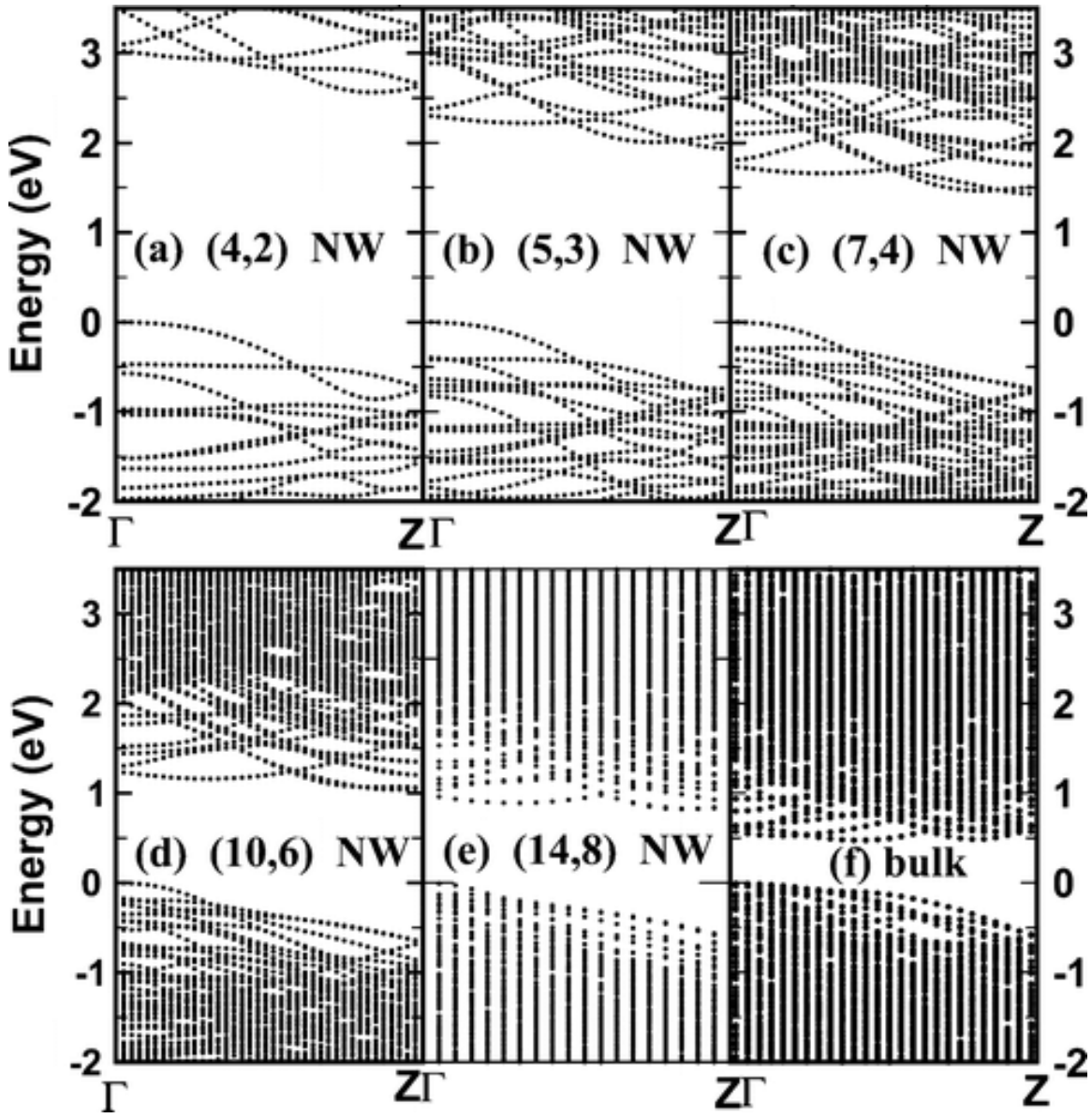

Figure 4.2. Energy band structures of selected [112] SiNWs: (a) (4,2) NW with $Si_{16}H_{16}$; (b) (5,3) NW with $Si_{30}H_{22}$; (c) (7,4) NW with $Si_{56}H_{30}$; (d) (10,6) NW with $Si_{120}H_{44}$; and (e) (14,8) NW with $Si_{224}H_{60}$. (f) The band structure of bulk Si projected in the [112] direction. The energy zero is set arbitrarily at the valence band maximum (VBM).

Also shown in Figure 4.3 are the band gaps of [112] wires measured by tunneling spectroscopy.[7] For a better comparison between the experimental and calculated band gaps, we fit the calculated (measured) data points with an approximate function of $E_{g,bulk} + C(1/d)^{\alpha}$,[26] where $E_{g,bulk}$ is the corresponding bulk gap value and C and α are fitting parameters. The diameter exponent α 2 for the experimental values is in accordance with the prediction by using an effective-mass particle-in-a-box model with an infinite barrier height. The α value is smaller for the calculated data (see fits in Figure 4.3 and Table 4.2). It is apparent that the dependence of the *GW* gaps on the wire size is somewhat different as compared with the experimental results. Nevertheless, it is important to note that the LDA gaps follow closely their *GW* counterparts. In addition, the quantitative difference here might also be attributed in part to the facts that the fitting procedures are based on only a few data points and that the definition of the wire diameters is somehow arbitrary. It is also noted that the diameter quoted in ref [7] is likely to be the width of the (111) facet, instead of the "effective diameter" defined by the cross-sectional area used in Figure 4.3. Therefore, the experimental points may not be plotted correctly according to the definition of diameter used in this paper.

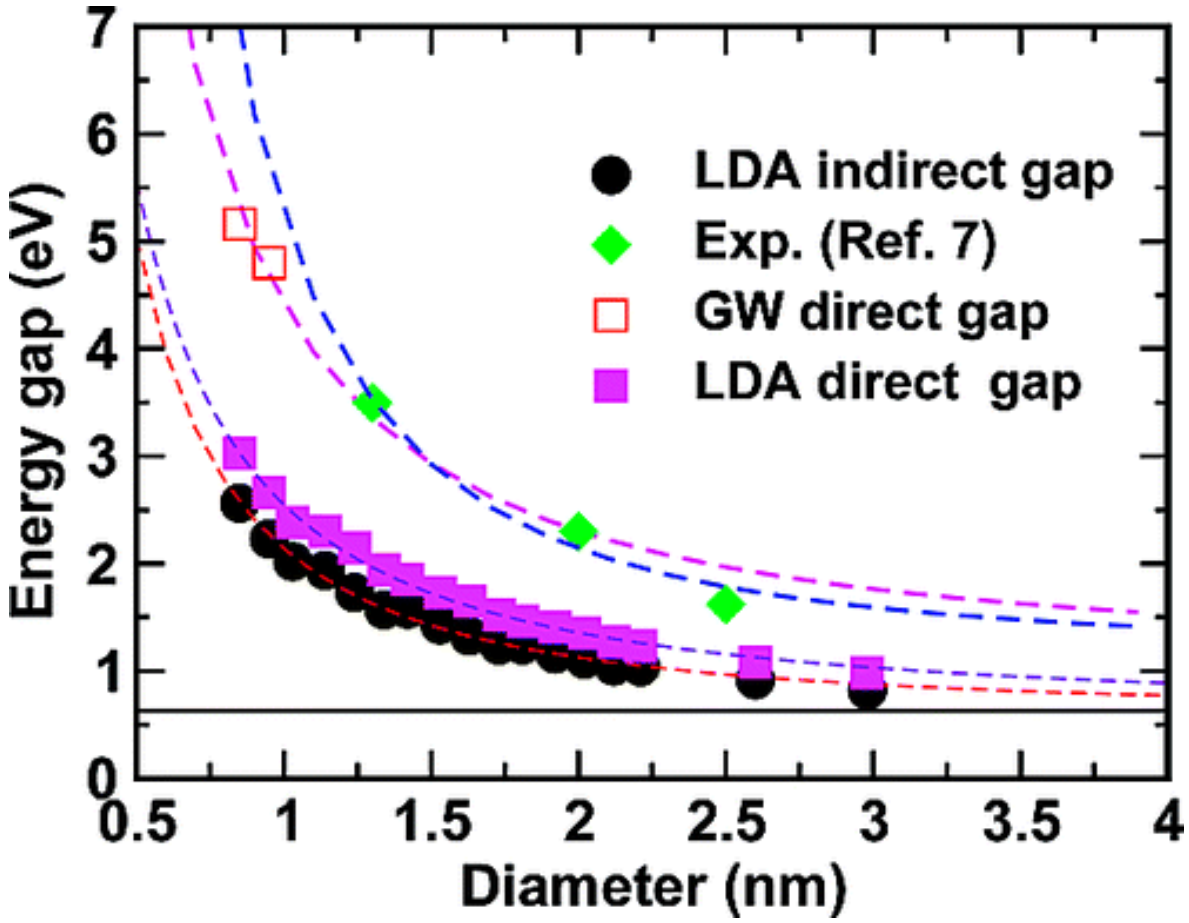

Figure 4.3. Calculated indirect (solid circles) and direct (solid squares) energy band gaps with LDA and direct band gaps with GW (empty squares) versus the diameter for [112] SiNWs. For comparison the measured band gaps of [112] wires by Ma et al.(7) (diamonds) are plotted. The solid horizontal line indicates the LDA gap of bulk Si. The dashed lines is fitted to the data points (see text). The fitting results are listed in Table 4.2.

Table 4.2. Fitting Parameters for Theoretical and Experimental Band Gaps As a Function of Diameter, The fitting has included the corresponding bulk value as the limit.

parameter	LDA (indirect)	LDA (direct)	GW	exp.[7]
C	1.56	1.97	3.32	4.04
α	1.51	1.35	1.44	2.06

Besides the indirect band gap, we also analyze the direct gap at Γ point, which is more relevant to the optoelectronic applications for SiNWs. For comparison purposes, the direct fundamental band gap is also included in Figure 4.3. It is interesting to observe that the energy difference between the direct and indirect fundamental gaps progressively decreases as the wire size increases. This feature can be traced back to the band structure of bulk Si projected in the [112] direction since the band gap and band edge states of a large SiNW with a small surface−volume ratio involved should develop toward its asymptotic bulk value. As shown in Figure 4.2f, the energy difference of the direct and indirect band gaps is only 0.1 eV in the projected band structure. This trend suggests that the larger [112] SiNWs could have a quasidirect band gap. We note that this feature has also been found in other two studies very recently.[15,16]

We now proceed to show that uniaxial stress may have an effect on the relative size of the direct and indirect band gaps. Presented as an illustrative example in panels a−c in Figure 4.4 are the band structures of the (10,6) wire under compressive, zero, and tensile uniaxial stress, respectively. It is evident that the energy difference between the indirect fundamental band gap and the direct one reduces with the increase of the compressive strain. This observation is also valid for other [112] SiNWs with different diameters. Starting from the projected band structure from the bulk, where the direct and indirect band gaps differ by only 0.1 eV, the rectangular confinement breaks the local cubic symmetry, and, in most cases we studied, raises the direct band gap more than the indirect one. The axial strain in turn adds another variational degree of freedom in changing the relative magnitude of these gaps. Similarly, varying the aspect ratio may accomplish the same effect.

As we have mentioned earlier, the aspect ratio of the rectangular cross section is not solely dictated by the ratio of surface energies as would be expected from the Wulff construction in the thin NWs where most of the atoms are at the surface. It is thus interesting to explore how the interplay between the relative number of atoms on the [111] and [100] surfaces modifies, if possible, the electronic properties of the nanowires.

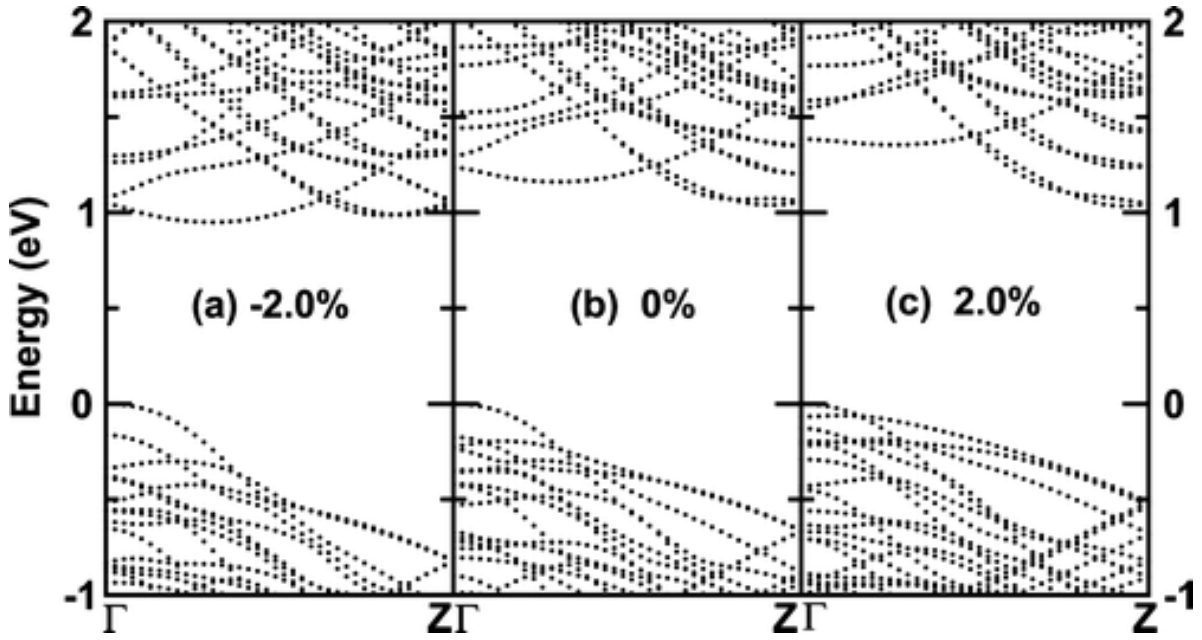

Figure 4.4. Energy band structures of the (10,6) SiNW with a diameter of 2.21 nm: (a) with 2% compressive strain along the wire axis; (b) free of axial strain; and (c) with 2% tensile strain along the wire axis. The strain is defined as the ratio of the lattice constant of a strained SiNW to that of a strain-free SiNW. The VBM has been shifted to zero.

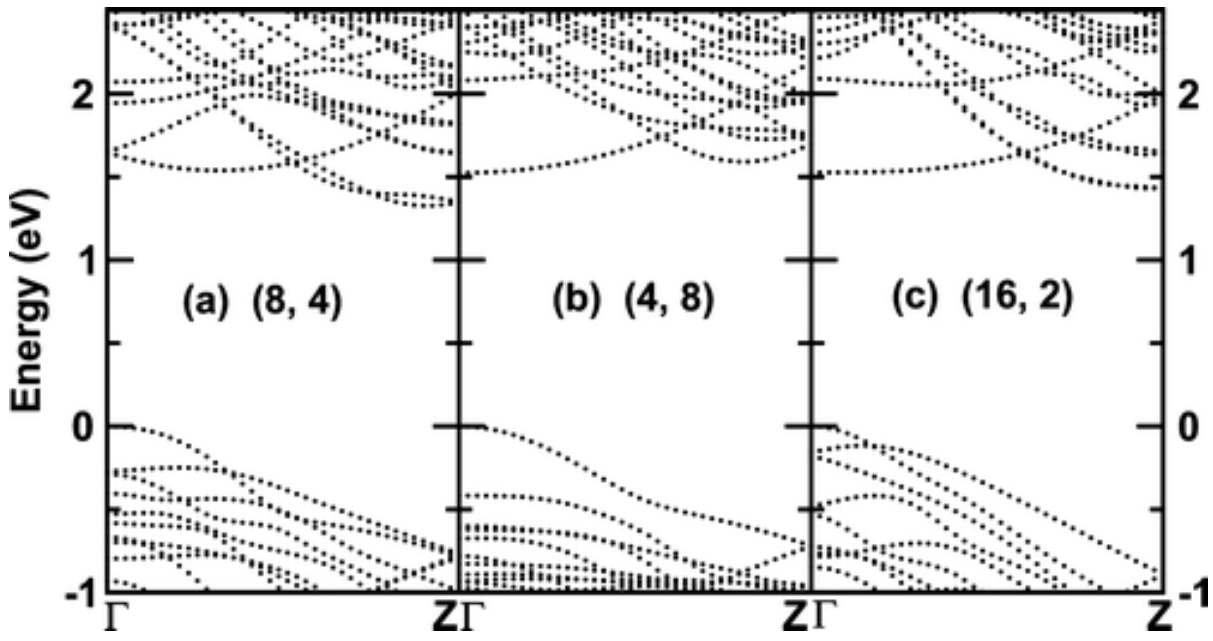

Figure 4.5. Representative energy band structures of SiNWs with the same number of Si atoms ($2MN = 64$) but different aspect ratios ($M \times d_{110}$:$N \times d_{111}$) of (a) 1.21, (b) 0.37, and (c) 4.60, respectively. The diameters are about 1.6 nm. The VBM has been shifted to zero.

To evaluate the effects of different aspect ratios of the cross section of SiNWs on its band structure and band gaps, we have performed calculations on the (4,8) and (16,2) wires, which are not energetically favorable wire geometries as compared to the (8,4) wire (the magic wire of the same 64 Si atoms per unit length). The resulting electronic structures are shown in Figure 4.5. It can be seen that the three [112] SiNWs with quite different aspect ratios do show noticeable differences in their band structures, as far as both band gap energy and dispersions of valence and conduction band are concerned. The (4,8) SiNW even shows a clear direct band gap, essentially different from the indirect band gap feature of the (8,4) and (16,2) SiNWs. It is noted that this observation for the [112] wire here is in good agreement with the finding by Migas in ref [27], where the [100] SiNWs with similar diameters but different cross sections were found to have distinctly different band gap size. However, we also note that this is not the case for the [110] wire according to the calculations by Ng et al. in ref [28], where they found that the different patterns of the cross section did not cause significant band gap changes for those [110] SiNWs with the same cross-sectional area.

4.4 Conclusion

In summary, the electronic properties of H-passivated [112] SiNWs with the atomic geometries retrieved via the global search using genetic algorithm are investigated from first-principles calculations. We show that [112] SiNWs have an indirect band gap in the ultrathin diameter regime, whereas the energy difference between the indirect fundamental band gap and the direct one progressively decreases as the wire size increases, indicating that relatively thick [112] SiNWs could have a quasi-direct band gap. We further show that this quasidirect gap feature can be enhanced when applying uniaxial compressive stress along the wire axis. Moreover, our calculated results also reveal that the electronic band structure of SiNWs is sensitive to the change of the aspect ratio of the cross sections. These findings could have important implications for the use of SiNWs in nanoscale devices as experimentally [112] nanowires have been found to grow abundantly with application-relevant thicknesses.

References of Chapter 4

(1) Cui, Y.; Zhong, Z.; Wang, D.; Wang, W. U.; Lieber, C. M. *Nano Lett.* **2003**, *3*, 149.

(2) Koo, S. M.; Li, Q. L.; Edelstein, M. D.; Richter, C. A.; Vogel, E. M. *Nano Lett.* **2005**, *5*, 2519.

(3) Goldberger, J.; Hochbaum, A. I.; Fan, R.; Yang, P. D. *Nano Lett.* **2006**, *6*, 973.

(4) Cui, Y.; Lieber, C. M. *Science* **2001**, *291*, 851.

(5) Cui, Y.; Wei, Q. Q.; Park, H. K.; Lieber, C. M. *Science* **2001**, *293*, 1289.

(6) Hahm, J.; Lieber, C. M. *Nano Lett.* **2003**, *4*, 51.

(7) Ma, D. D. D.; Lee, C. S.; Au, C. K.; Tong, S. Y.; Lee, S. T. *Science* **2003**, *299*, 1874.

(8) Vo, T.; Williamson, A. J.; Galli, G. *Phys. Re*V. *B* **2006**, *74*, 45116.

(9) Ponomareva, I.; Menon, M.; Richter, E; Andriotis, A. N. *Phys. Re*v.*B* **2006**, *74*, 125311.

(10) Niquet, Y. M.; et al. *Phys. Re*V. *B* **2006**, *73*, 165319.

(11) Li, J.; Freeman, A. J. *Phys. Re*V. *B* **2006**, *74*, 75333.

(12) Rurali, R.; Lorente, N. *Phys. Re*V. *Lett.* **2005**, *94*, 26805.

(13) Zhao, X.; Wei, C. M.; Yang, L.; Chou, M. Y. *Phys. Re*V. *Lett.* **2004**, *92*, 236805.

(14) Yan, J. A.; Yang, L.; Chou, M. Y. *Phys. Re*V. *B* **2007**, *76*, 115319.

(15) Lu, A. J.; Zhang, R. Q.; and Lee, S. T. *Nanotechnology* **2008**, *19*,35708.

(16) Rurali, R.; Aradi, B.; Frauenheim, T.; Gali, A. *Phys. Re*V. *B* **2007**,*76*, 113303.

(17) Ho, K. M.; Shvartsburg, A. A.; Pan, B. C.; Lu, Z. Y.; Wang, C. Z.; Wacker, J.; Fye, J. L.; Jarrold, M. F. *Nature* **1998**, *392*, 582.

(18) Chan, T. L.; Ciobanu, C. V.; Chuang, F. C.; Lu, N.; Wang, C. Z.; Ho, K. M. *Nano Lett.* **2006**, *6*, 277.

(19) Lu, N.; Ciobanu, C. V.; Chan, T. L.; Chuang, F. C.; Wang, C. Z.;Ho, K. M. *J. Phys. Chem. C* **2007**, *111*, 7933.

(20) Pimpinelli, A.; Villain, J. *Physics of Crystal Growth*; Cambridge University Press: New York, 1998; Chapter 3.

(21) Kresse, G.; Hafner, J. *Phys. Re*V. *B* **1994**, *49*, 14251. Kresse, G.; Furthmu ̈ller, J. *Comput. Mater. Sci.* **1994**, *6*, 15.

(22) Vanderbilt, D. *Phys. Re*V. *B* **1990**, *41*, 7892. Kresse, G.; Hafner, *J. Phys.: Condens. Matter* **1994**, *6*, 8245.

(23) Monkhorst, H. J.; Pack, J. D. *Phys. Re*V. *B* **1976**, *13*, 5188.

(24) Hybertsen, M. S.; Louine, S. G. *Phys. Re*V. *B* **1986**, *34*, 5390, and references therein.

(25) Williamson, A. J.; Grossman, J. C.; Hood, R. Q.; Puzder, A.; Galli, G. *Phys. Re*V. *Lett.* **2002**, *89*, 196803.

(26) Delerue, C.; Allan, G.; Lannoo, M. *Phys. Re*V. *B* **1993**, *48*, 11024.

(27) Migas, D. B. *J. Appl. Phys.* **2005**, *98*, 54310.

(28) Ng, M. F.; Zhang, L.; Yang, S. W.; Sim, L. Y.; Tan, V. B. C.; Wu, P. *Phys. Re*V. *B* **2007**, *76*, 155435.

Chapter 5. STRUCTURAL MODELS OF AG INDUCED SI(111) SURFACE RECONSTRUCTION DETERMINED BY GLOBAL OPTIMIZATION METHODS

This chapter consists of two parts. The first part is composed of 5.1,5.2,5.3,5.4, which is our paper *Islands and Holes as Measures of Mass Balance in Growth of the (√3x√3)R30^o Phase of Ag on Si(111)* by Alex Belianinov, Barış Ünal, Ning Lu, Min Ji, K.-M. Ho, C.-Z. Wang, M. C. Tringides, and P. A. Thiel, which is to be submitted. Chap 5.2 is the experimental work done by Alex Belianinov, Barış Ünal and P. A. Thiel, including the fabrication of Ag on Si(111) reconstruction in the lab and measurement of STM. I did the theoretical part including the variable-number GA search of √3x√3 A/Si(111) structures, structural mitifs analysis and simulation of STM images. The second part is in 5.6, which is about a new structural model for Ag/Si(111)-(3x1) surface reconstruction. It's a theoretical prediction done by me with the variable-number GA search process.

5.1 Introduction

The (√3x√3)R30^o surface phase of Ag on Si(111)—called √3 herein—is an important structure that has been studied intensely,[1] since it was first reported in 1967.[2] It is established that conversion of the (7x7) to the √3 in the presence of adsorbed Ag is an activated process, occurring in the range of about 500 - 900 K. It is also known that the areal density of Si is not preserved when the (7x7) converts to the √3. This change in Si density, in the presence of limited diffusion on large terraces, causes the √3 to partition locally into regions above the (7x7), i.e. "islands", and regions below the (7x7), i.e. "holes."[3-7] These features are illustrated schematically in Fig. 5.1A, and by experimental data in Fig. 5.1B. A similar partitioning occurs during the development of the √3 structure of Au on Si(111).[7,8]

Because of Si mass balance, the areal ratio of islands to holes (R_{IH}) can be, and has been,[5-7] used to deduce the density of Si in the √3 phase. (See Appendix.) Using scanning tunneling microscopy (STM), both Shibata et al.[5,7] and Wan et al.[6] measured $R_{IH} \approx 1$ and deduced the Si surface density to be 1 atom per (1x1) unit cell area, i.e. 1 monolayer (ML). This means that one full layer of Si is missing in the √3 relative to the unreconstructed Si surface.

These results helped to shape and support the current model for the √3. This model is known as the Inequivalent Triangle (IET) model,[9,10] and can be viewed as an asymmetrical variation of the Honeycomb Chain Trimer (HCT) model.[11] Accordingly, some groups report that structures with IET symmetry transform reversibly to apparent HCT symmetry around 300 K, due to thermal fluctuations in the IET structure.[12-14] However, Zhang et al. report that both structures can co-exist statically even at room temperature.[15,16] In the present work, we observe only the apparent HCT structure.

We pose two questions: Does the measured value of R_{IH} depend on the conditions under which the √3 is prepared? If so, since R_{IH} is determined by the Si coverage in the √3 phase, is it possible that there is more than one type of √3 phase with different Si and Ag coverages? We employ both STM and density functional theory (DFT) to find the answers.

5.2 Experimental Motivation

In our STM experiments, residual (7x7) always coexists with islands and holes because the Ag coverage is deliberately adjusted to be in the submonolayer range, i.e. insufficient for complete conversion. The two parameters that we vary systematically are (i) the temperature at which Ag is deposited, T_{dep}; and (ii) the time, t_{ann}, of annealing after deposition ends. Focusing first on the deposition temperature, Fig. 5.2 is a series of STM images after deposition of 0.4 to 0.6 ML Ag at varying temperatures, followed by annealing for 1-2 minutes. The fractional area of 7x7 that remains unconverted ranges from 0.6 to 0.4 in these experiments. We count the elevated regions as islands, regardless of the structure (or lack thereof) on top of the island. The dark areas—holes—are so small that they are barely evident in Fig. 5.2A, but they become larger as T_{dep} increases.

Inspection of the islands and holes indicates that under some conditions, especially for $R_{IH} > 3$ and/or $T_{dep} < 600$ K, the island tops contain substantial disordered regions. Other authors have identified the disordered phase as Ag which is a precursor to the √3.[3,4] Its variation during the transformation to √3 will be discussed elsewhere.[114]

The ratio R_{IH} varies both with T_{dep} and t_{ann}. Fig. 5.3 shows the variation with T_{dep}. R_{IH} is as high as 6 after Ag deposition at 500 K. It falls to $R_{IH} \approx 1$ at $T_{dep} = 800$ K. For annealing, Fig. 5.4A shows that R_{IH} falls from an initial value of 2.7, and approaches 1 at long t_{ann}, following deposition at 600 K. From both

the deposition and annealing experiments, we conclude that $T_{dep} < 800$ K can easily lead to $R_{IH} > 1$, but $R_{IH} \approx 1$ is the limiting value.

Is the decrease in R_{IH}—e.g. in Fig. 5.3 and 5.4A—attributable to decreasing area (A) of the islands, increasing area of the holes, or both? Figure 5.5 shows the changes in absolute areas during annealing at 600 K, where the initial value of R_{IH} is 2.7 (cf. Fig. 5.4A). During annealing, A_{hole} increases by a factor of 4, and this is compensated by a decrease in the area of the 7x7. The variation in A_{island} is much less than the other two variables. Therefore, the decrease in R_{IH} is predominantly due to an increase in the denominator, A_{hole}, with a concomitant decrease in the (7x7) area. In other words, the holes expand and consume the 7x7. A reservoir of Ag must exist that feeds the holes during annealing, and correspondingly, a sink must exist to consume the displaced Si.

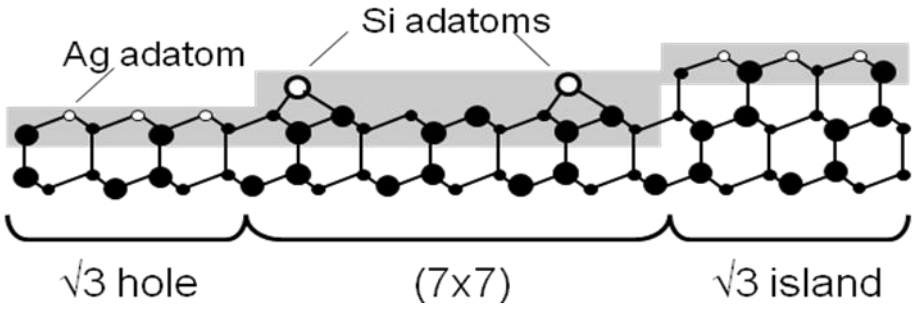

(a)

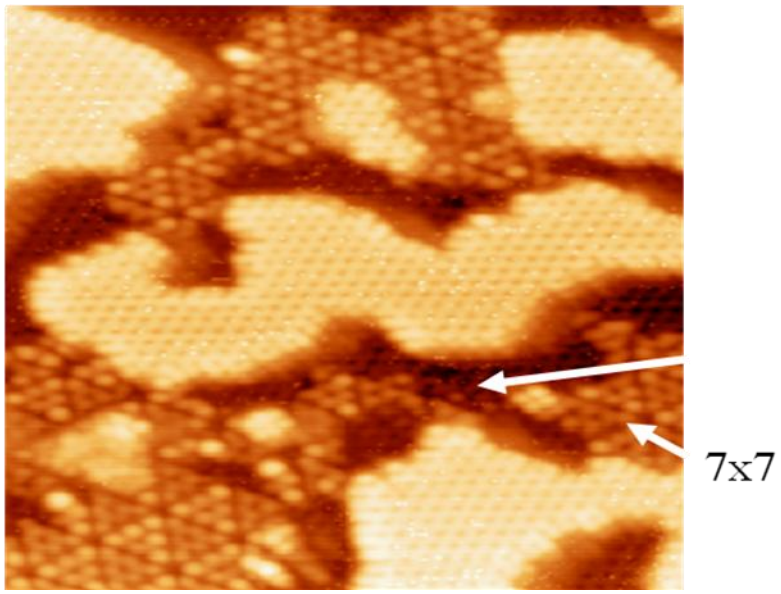

(b)

Figure 5.1. (a) Schematic of the Si(111) surface, illustrating the formation of √3 islands and holes from the (7x7). The shaded regions represent the depth over which atoms are counted for calculating atom densities in the Appendix, after Ref. [5,6]. Black circles are Si atoms, small open circles are Ag atoms, and large white circles are Si adatoms in the (7x7). Reproduced from Ref.[5]. (b) STM image illustrating √3 islands, √3 holes, and (7x7) phase. The surface was prepared by depositing 0.69 ML Ag at 615 K and then annealing for 2 minutes. Image size is 25 x 25 nm^2. Tunneling conditions are bias voltage (V_T) = -1.0 V and tunneling current (I_T) = 0.2 nA.

(STM done by Alex Belianinov, Baris Unal and Pat Thiel)

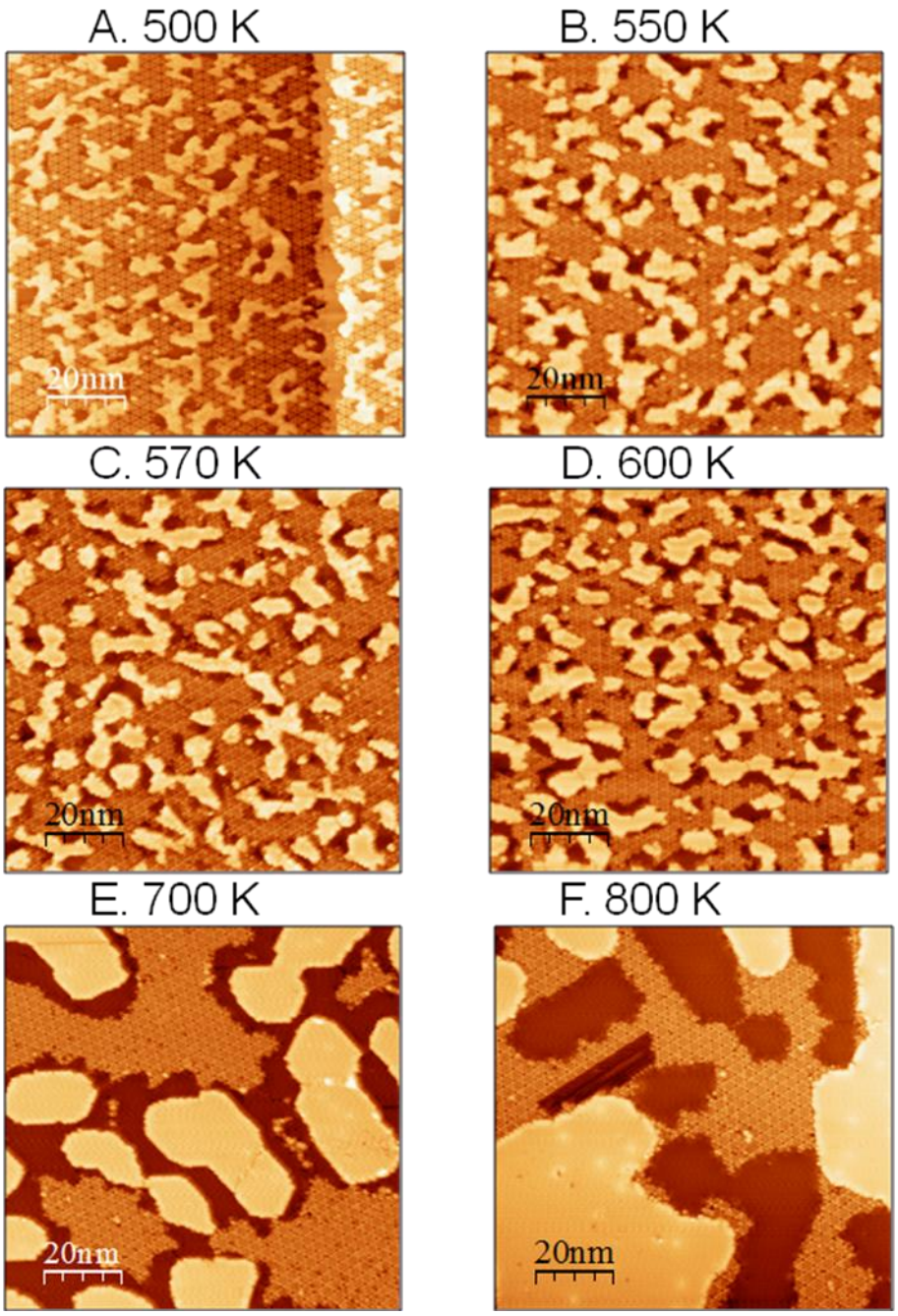

Figure 5.2. STM images after Ag deposition at various temperatures. All images are 100 x 100 nm^2. Unless noted otherwise, V_T = -1.0 V and I_T= 0.2 nA. Values of R_{IH} are averages over multiple images. (A) T_{dep} = 500 K, 0.49 ML Ag, R_{IH} = 5.4. (B) T_{dep} = 550 K, 0.46 ML Ag, R_{IH} = 3.8. (C) T_{dep} = 570 K, 0.44 ML Ag, R_{IH} = 3.5. (D) T_{dep} = 600 K, 0.53 ML Ag, R_{IH} = 3.0. (E) T_{dep} = 700 K, 0.73 ML Ag, R_{IH} = 1.7, V_T = -2.0 V, I_T= 0.5 nA. (F) T_{dep} = 800 K, 0.53 ML Ag, R_{IH} = 1.0, V_T = -1.0 V, I_T= 2 nA.

(STM done by Alex Belianinov, Baris Unal and Pat Thiel)

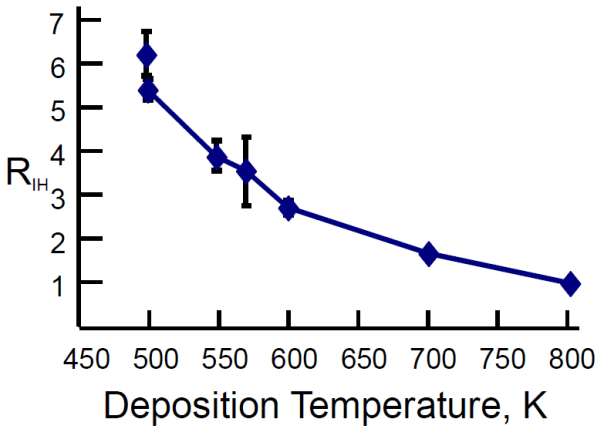

Figure 5.3. R_{IH} as a function of deposition temperature. The sample was held for 1 minute at T_{dep} after deposition finished, with the exception of the first point, R_{IH} = 6.2 at 500 K, where the ratio was measured immediately after deposition. Values are averages over multiple images, and error bars are standard deviations. If no error bars are visible, they are obscured by the symbol.

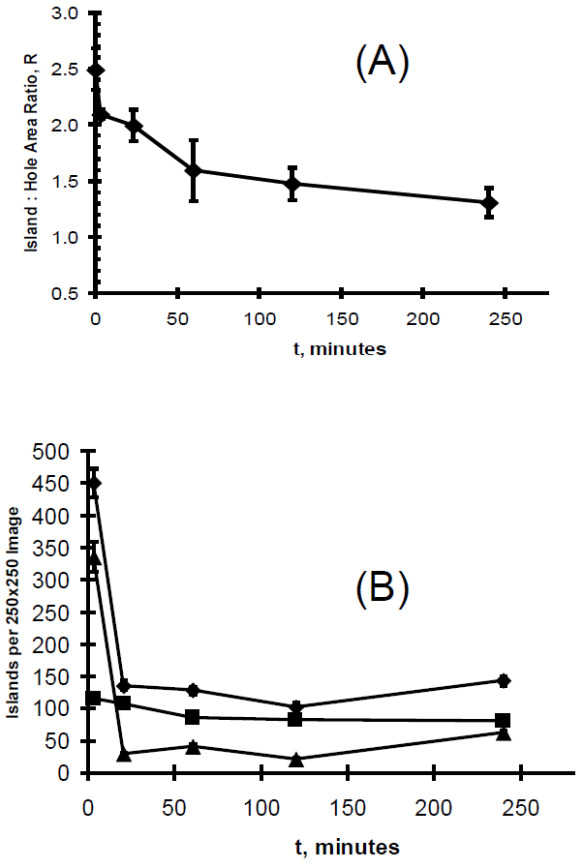

Figure 5.4. (A) R_{IH} as a function of t_{ann} at 600 K. At t_{ann} = 0, deposition has just ended. Values are averages over multiple images, and error bars are standard deviations over images within a single run. (B) Densities of islands as a function of t_{ann} at 600 K. The diamonds show all islands, triangles show islands with individual areas $\leq$ 50 nm^2, and squares show larger islands. Error bars show the standard deviation of the island density in various images. Images are weighted according to their size. When error bars are not visible, they are covered by the individual data point.

Shibata et al. have reported that Ag nucleates into islands that serve as precursors to the √3. From data taken with *in situ* STM, and working at temperatures of 440-525 K, they concluded that these Ag islands can convert to √3, but only if they are above a critical size of two 7x7 unit cells (about 12 nm^2). We therefore consider the possibility that small islands are Ag-rich, and that they can provide the Ag needed for expansion of the holes. Indeed, we see small islands in the STM images, and they disappear during annealing. However, their disappearance is only partially correlated with the change in R_{IH}. Figure 4B shows the number density of islands in two size ranges during annealing. Most islands in the range below 50 nm^2 disappear very quickly, long before the value of R stabilizes. We conclude that the small islands may contribute some of the Ag needed, especially early in the process, but certainly not all.

When surfaces are prepared by deposition of Ag at 600 K, a good √3 structure exists both on island tops and in holes throughout the range $3 \geq R_{IH} \geq 1$. This statement is based upon STM inspection of many islands and holes. The existence of √3 throughout the range $3 \geq R_{IH} \geq 1$, and not just at $R_{IH} \approx 1$ as predicted by the IET model, naturally leads one to question whether there might be different types of √3 structures—perhaps including metastable phase(s) with high Ag:Si ratios. However, high-resolution images of the √3, measured on both islands and holes for different values of R_{IH}, do not support this hypothesis. Some of the STM images are shown in Fig. 5.6. For comparable tunneling conditions, there is no apparent difference in the structure. Thus, these data support only a single type of √3.

A further characterization of the √3 is the vertical separation between islands, holes, and (7x7) regions for different T_{dep}. (Note that only 2 of the 3 separations are independent.) Because the separations measured with STM can depend upon electronic as well as topographic variations, we measure separations at different tunneling bias. Results are shown in Fig. 5.7, derived from pixel height histograms. Data are only shown for surfaces where $3 \geq R_{IH} \geq 1$. The vertical separation between islands and holes, averaged over bias voltages between $\pm$2 V and over the 3 experiments where $3 \geq R_{IH} \geq 1$, is 0.293 $\pm$ 0.026 nm. This compares well with 0.314 nm, which is the bulk separation between equivalent Si(111) planes and which is expected based upon Fig. 5.1A. From this, it appears that the heights are primarily topographic. The measured island-to-(7x7) separation (not shown), taken as an average over the same range of bias voltage (V_T) and the same 3 experiments, is 0.148 $\pm$ 0.048 nm. This is half the former value—as it should be if the

structure on the island tops is the same as in the holes. We conclude that, within experimental error, the average heights of islands and holes does not depend significantly on preparation conditions or R_{IH}-value, under conditions where a good √3 exists on both features. This lack of variation is again consistent with a single type of √3 structure.

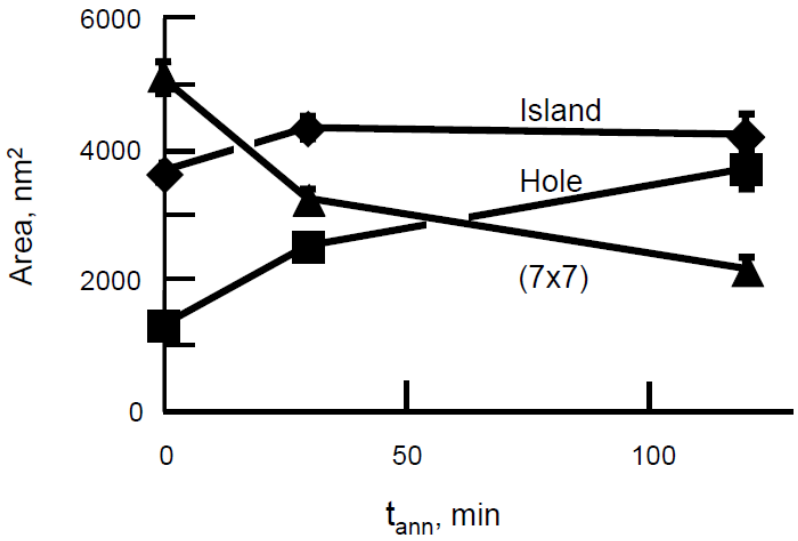

Figure 5.5 Graph illustrating the change in areas of Si(111)-7x7 phase (triangles), √3 islands (diamonds) and √3 holes (circles) with annealing time at 600 K. Values are averages over multiple images, and error bars are standard deviations. Most error bars are obscured by the symbols.

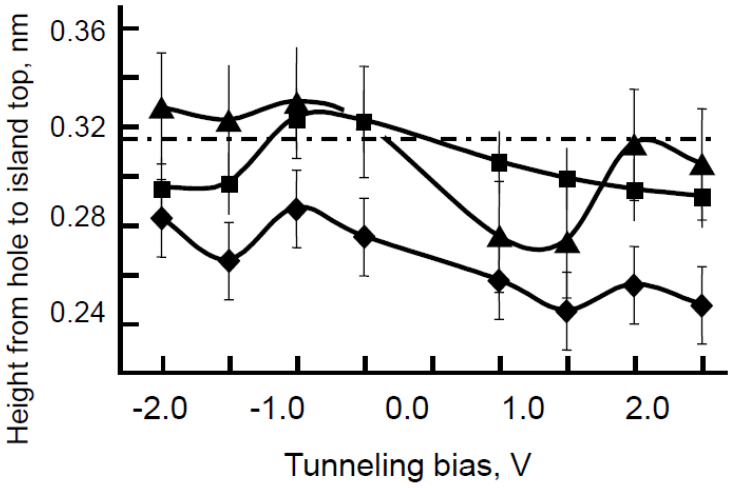

Figure 5.7 Heights measured from height histograms of STM images as a function of tunneling bias, V_T. The three curves represent samples prepared under three conditions: (i) by deposition at 600 K (triangles), R_{IH} = 2.7; (ii) the same followed by annealing for 30 minutes at 600 K (squares), R_{IH} = 1.7; and (iii) by deposition at 600 K followed by annealing for 2 minutes at 800 K (diamonds), R_{IH} = 1.0. The horizontal dashed line shows the value expected for two layers of Si (see Fig. 5.1A). Error bars show the full-width at half-maximum of peaks in the pixel height histogram.

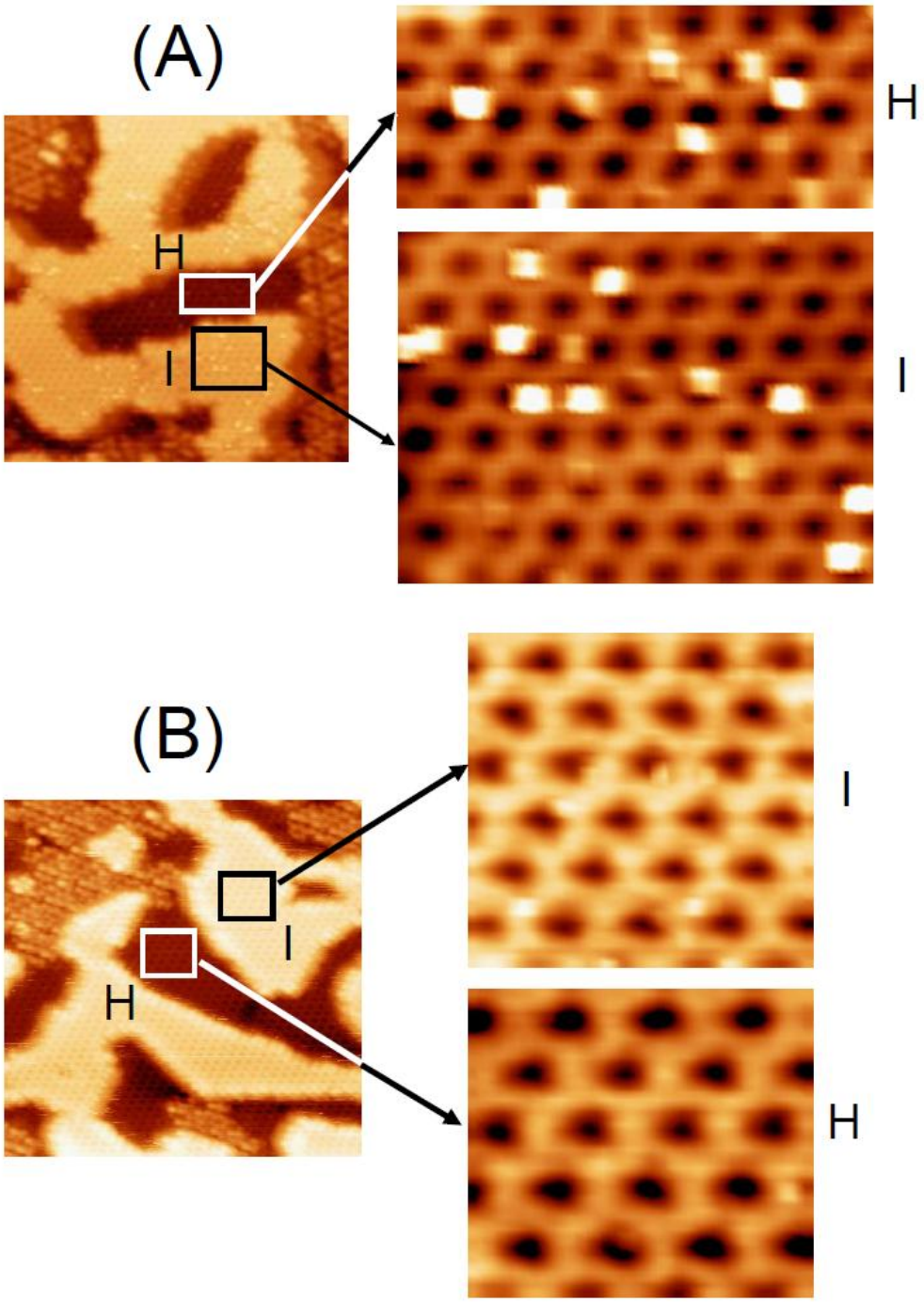

Figure 5.6 STM images of the √3 structure in islands and holes, after preparation at different conditions. (A) Ag deposited at 615 K, no annealing, R_{IH} = 2.8. Tunneling conditions are V_T = -1.4 V, I_T= 0.2 nA. Image sizes are 25 x 25 nm^2 (left), 5.6 x 2.4 nm^2 (top right), and 5.8 x 4.3 nm^2 (lower right). (B) Prepared as in (A), plus annealing at 615 K for 2 minutes. R_{IH} = 2.0. V_T = -1.0 V, I_T= 0.2 nA.

(STM done by Alex Belianinov, Baris Unal and Pat Thiel)

5.3 Variable-Number Genetic Algorithm with DFT Methods

Genetic Algorithm (GA) has been successfully applied in structural optimization for surfaces, nanowires and clusters, and the search procedure is from the idea of evolutionary approach in which the members of a generation (pool of models for surface) mate with the goal of producing the best specimens, i.e. lowest energy reconstructions. We tried an improved variable-number GA with DFT, which gives a comprehensive and accurate structural optimization. First the new GA has a pool of variable number of both Ag and Si atoms, and it covers all the possible combination of all coverage. Compared with the traditional GA that only searches the structures with fixed number of atoms, the Variable-Number GA can gives a more general global minimum search, given the real situations that atoms numbers are unknown in most cases. Moreover, the Variable-Number GA can accelerate the convergence of global structure search [25]. Second, the new GA is using ab initio calculation to relax the structures in each generation, instead of the empirical or tight binding potentials. In our previous GA search, we only used DFT methods to evaluate the final structures found by GA with classical potentials. We had to risk missing global optimization during the search due to the inaccuracy and defects from the non-DFT potentials, given the limited computational resources. With improvement in computers, we are now able to precisely evaluate the surface energies for every newly generated structure. With the robust GA, we can achieve the global optimized structures accurately and quickly.

The calculations were carried out within the local density approximation of density functional theory using projector-augmented-wave (PAW) potentials [21], as implemented in Vienna ab initio Simulation Package (VASP) [22]. The kinetic energy cutoff was set to 250 eV and the 4x4 Monkhorst-Pack grid was used for the surface Brillouin zone (BZ). The rt3xrt3 Ag/Si(111) surfaces were of the unit cell based on Si bulk constant of around 5.40 A. The surface was modeled by a periodically repeated slab of two fixed Si bilayers, one hydrogen passivated layer in the bottom, a reconstructed Ag/Si layer on the top, and a vacuum gap of ~8 A. The Si-H distance was set to be 1.51A and kept fixed. The two silicon bilayers were kept fixed at the bulk crystalline positions. All the models were based on a (rt3 x rt3) supercell. The remaining Ag and Si atoms were relaxed until the residual force was smaller than 0.025 eV/A.

Given the total energies of the models, the surface energy, Ef, is calculated using Ef= Etot – Esub-Nsi*mu(si)-Nag*mu(Ag), where the Etot is the total energy, Esub is the substrate of two silicon bilayers and one hydrogen layer. The mu(Si) and mu(Ag) are the chemical potential of Si and Ag bulk phases, and Nsi and Nag are the Si and Ag atoms numbers on top of the fixed substrate.

5.4 Structural Models for Ag/Si(111)-(√3x√3)

For the metastable structures of the islands, there are 2 possibilities for them. The island could be a homogeneous and ordered surface with Ag and Si, or it could be disordered one, which may be the combination of different ordered surfaces.

5.4.1 Ordered surface models

The first situation we considered is the ordered case. Let's start with one of the experimental data that the area ratio between islands and the holes is 0.49:0.17, while the rest of the surface is still the 7x7 Si(111). Since the Ag coverage on the islands is difficult to determine, we'd like to start our discussion from the Si coverage. We could input the areas of both islands and holes into eq (5.1) and get the following expression

$$n1(Si)*0.49 + n2(Si) * 0.17= 2.08 *(0.49+0.17) \quad (5.1)$$

The n1(Si) and n2(Si) are Si coverage on islands and holes, and the value of 2.08 is the silicon coverage of 7x7 Si(111) surface. Since only rt3xrt3 structure was found on island and holes, we would assume the unknown surface still keeps the same unit cell. In a rt3xrt3 unit cell, each 1 Si atom constitute 1/3 ML coverage, therefore we only need to consider the solutions that are the multiples of 1/3 ML. The 5 possible combinations of silicon coverage on both islands and holes are listed below

Table 5.1 Si coverage for both islands and holes

N1 (ML)	2	2.08	2+1/3	2+2/3	3
N2 (ML)	2.31	2.08	1.35	0.39	-0.57

The 1st case is impossible that the islands have lower silicon coverage, and the holes are thereafter even higher than the islands. The 2nd solution of both 2.08 ML means the holes and islands remain a 7x7

reconstructed Si (111) surface, which still makes the islands and holes invisible. The rest of the 3 solutions may be the possible solution. The Si(111) has a period of Si bilayer, so we could subtract 2ML from each coverage that is bigger than 2. Therefore the 3 possible solutions are be simplified below

Table 5.2 Si coverage for islands and holes

N1(ML)	1/3	2/3	1
N2(ML)	1.35	0.39	-0.57

(1) 1/3ML islands and1.35ML holes

The 1st solution is that the Si coverage is 1/3 and 1.35 separately, which means the islands have 1 Si and holes have 4 Si atoms in each rt3xrt3 unit cell. We did a complete Genetic Algorithm (GA) search over all the possible coverage for both Ag and Si on a rt3xrt3 surface unit. The energies were precisely evaluated by ab initio calculations. The relaxation was done by conjugate gradient (CG), so those are the zero temperature formation energies. The number of silicon we searched is from 1 to 6, which covers the 6 possible coverages from 0 to 2ML. For each of the 6 coverage, we also searched the structures with 0 to 9 Ag atoms. We were hoping to get some metastable structures other than IET at some different coverage.

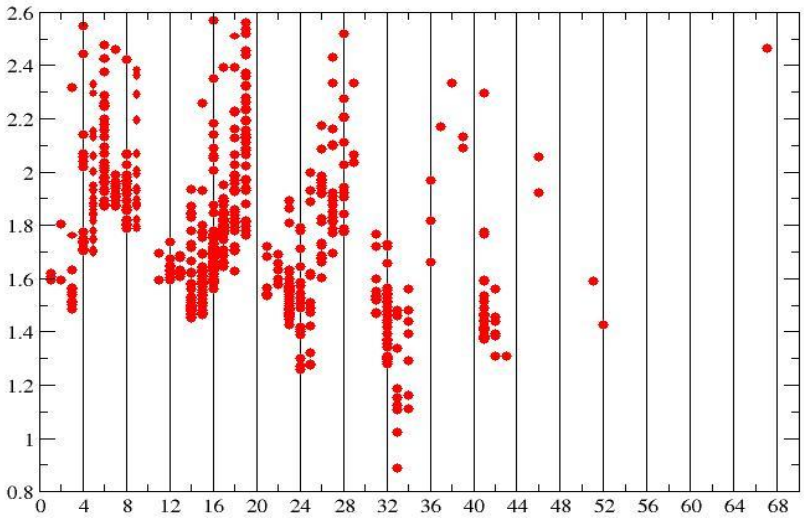

Figure 5.8. Formation energies for the rt3xrt3 Ag/Si(111) structures, the first digit is the Si atoms and 2nd is Ag atoms number within rt3xrt3 unit cell.

The GA results are shown in the graph above, each point representing a structure found by GA. In order to include both Si and Ag coverage, we introduce the 2-digit x axis, the 1st digit being the Si and 2nd being the Ag atoms per rt3xrt3. For example, the point with the lowest formation energy has a value of 33, which means it has 3 Si (1ML) and 3 Ag (1 ML) in a unit cell. This one is the Inequivalent Triangle (IET) structure, and it agrees well with all previous experimental observations that IET is the most stable structure in the rt3xrt3 unit cell in low temperature. The blue line is the formation energy of 7x7 Si (111) surface.

If our assumption of 1/3 ML islands and 1.35 ML holes is correct, we can choose the lowest structures with 1 Si and 4 Si ones. From the graph above, we would choose the one with 1 Si and 4 Ag for the islands. The formation energy is above 1.4 eV/unit^2, which is much higher than both Ag/Si IET and 7x7 Si (111) structures. In another word, the combination of both IET and 7x7 is more energetic favorable than this 1Si and 4 Ag rt3xrt3 structure. For the holes covered with 4 Si and 2 Ag atoms, the formation energy is much higher than the IET structure.

In conclusion, the model that islands have 1/3 ML and holes have 4/3 ML Si coverage does not have a energetic preference than the IET structure.

(2) 2/3 ML islands and 1/3 holes

The model of 2 Si atoms in the island and 1 Si in the holes is still not energetic favorable than the IET and 7x7 combination. The explanation is almost the same as the above model.

(3) 1ML islands and -0.57 ML holes

This model has a negative Si coverage for the holes, which means that the holes are deep into the silicon substrate. Although the substrate is more stable than the 2.08 ML surface Si atoms in the 7x7 Si(111) reconstructed structures, we still would like to discuss the possibility. Another problem is that the -0.57 ML Si coverage is not available in the rt3xrt3 unit cells. Since the area ratio of island and holes is not accurately measured, we could assume there's a 10% error in the experiments. Let's assume the real ratio is 3.3:1 for the island and holes, then the coverage of the holes is -0.956ML while the islands has 3ML Si coverage. In the substrate with 0.956 ML Si removed, we could assume it has coverage of 1 ML in the holes. Moreover,

the islands also have a 1ML Si coverage. It's the most desirable solution since both islands and holes could have a energetic stable IET structure.

Figure 5.9 presents the process of the surface evolution. At first, about 3ML Si atoms are removed and form the holes area. With those 3 ML Si atoms moved to the nearby areas, there comes the 3ML island with almost the 3 times of the area of the holes. Since both islands and holes are with a stable IET surface, this 3:1 islands and holes combination becomes a metastable structure. After long time's annealing, the nearby 7x7 Si(111) surface has their Si atoms moved into holes, making a higher holes with 3 times area as the metastable holes and also a 1:1 island-hole ratio.

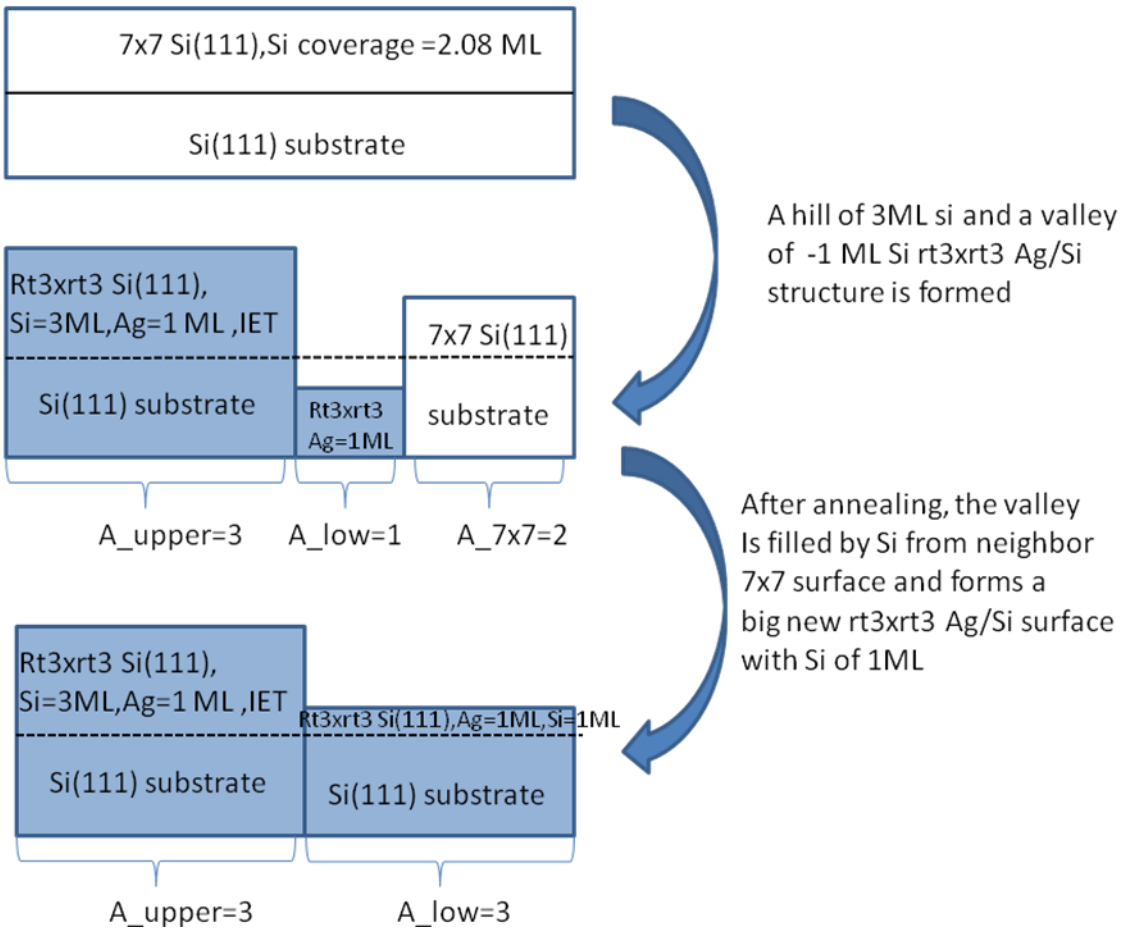

Figure 5.9 Surface evolution through -1ML holes to +1 ML holes

5.4.2 Disordered surface structural models

After analysis over all possible coverage of both Ag and Si, we could not find a satisfying model that gives the ordered Ag/Si(111) surface for the metastable state with R=3. Therefore we believe the surface may be a combination of at least 2 structures. Since the holes are very likely to be the rt3xrt3 IET surface according to the STM images, we assume only the islands are disordered.

Suppose we have both A area for the holes and islands in the final 1:1 ratio state, which are both IET Ag/Si(111) surfaces. There are 2/3A 7x7 Si(111) surface in the state of 3:1 that would be transformed into IET holes in the 1:1, thereafter the Ag are all from the islands. Hence the islands should be of an average 1.67ML Ag coverage in the 3:1 state. Considering the IET has the lowest surface energy and may be one phase in the islands, the unknown phase should be of a very high Ag coverage that's even higher than 2ML. We therefore proposed the rim of the islands may be pure Ag bulk structures.

In order to calculate the FCC Ag bulk on top of Si(111) surface without lattice mismatch, we used the 3x3 unit cell of Si (111), on top of which putting a 4x4 Ag(111) lattice. The mismatch between 4x4 Ag(111) and 3x3 Si(111) lattice constants is just 0.8%, which gives us a good unit cell for estimating the bulk Ag surface energy. The calculation was done by VASP with the same setup of parameters as the GA search and the K-points of 3x3x1.

The energies of 1layer and 2 layers Ag films on Si(111) substrate is presented in the Fig 5.10 below. The 16/9 ML and 32/9 ML Ag coverage is based on the Si(111) surface. We also added the 7x7 surface energy of 1.14 eV/1x1at 0 ML coverage. Fig 5.10 is another form of Fig 5.8 with no Si but only Ag coverage.

As we could clearly see from the graph above, all the possible rt3xrt3 Ag/Si(111) configurations other than the IET stand above the lines between 7x7 and IET when Ag coverage is below 1ML, and also the line between IET and 2 Ag FCC layers on Si(111) with Ag coverage is above 1ML.

We could claim that the combination of IET and 2 Ag FCC films on Si(111) is the energically favorable solution for the islands when the Ag coverage is higher than 1ML. Within the Ag coverage range between 1ML and 3.55 ML, no other rt3xrt3 Ag/Si(111) configuration can beat the combination. For those

structures with Ag coverage less than 1ML, a combination of IET and 7x7 Si(111) is the favorable solution by the same way.

With the proof of energy that the islands consist of IET and Ag bulk structures, we did some estimation of the bulk Ag structures on the rim of the islands. With the assumption that islands remain the same area from R=3 to R=1 states, we could calculate the area of Ag bulk structures based on the conservation of both Ag and Si atoms. The solution of the area is roughly 0.25 of the total islands area, both Ag and Si conservation equations giving similar solution.

The whole picture of the Ag/Si surface formation is shown in the Figure 5.11. We begin with a perfect 7x7 Si(111) surface with an area of 2A. After deposition at 600 K and 1 minute annealing, we got a metastable configuration with islands to holes ration of 3:1. The holes with 1/3A area have the IET surface, which gives a 1 ML coverage for both Ag and Si.The islands consist of IET and bulk Ag. The IET islands of 3/4A area are 1Si bi-layer higher than the IET holes, therefore they got a 3ML Si coverage and 1ML Ag coverage. The bulk Ag islands consists of 2 layers of FCC Ag(111), making it a Ag reservoir of 3.55ML Ag coverage. The bulk Ag islands is about 1.3 A lower than the IET islands, however the difference may not be that noticeable in STM because of the higher charge density in the Ag area. The bulk Ag islands stay at the rim of the islands according to the STM images. After a long time of annealing, about 2.55 ML of Ag on the ¼ A islands flow into the 2/3A7x7 Si(111) surface while 1ML of Si on that area flow onto the islands, forming a IET surface on both islands and holes surfaces.

5.5 Conclusion to the Ag/Si(111)-(√3x√3) islands and holes models

According to the STM images under different deposition temperatures for Ag induced Si(111) surface, we have shown that values of R_{IH} as high as 3 can be obtained under conditions where both islands and holes are covered by the √3 phase. A variable-number Generatic Algorithm global search has been performed on the √3x√3 unit cell and all the possible models have been discussed. The GA search found the most stable structure for √3x√3 Ag/Si(111) surface is still the Inequivalent Triangle (IET). However, inhomogeneous islands consisting of pure Ag films and IET surface are proved to be energetically stable for the R_{IH}=3 structures

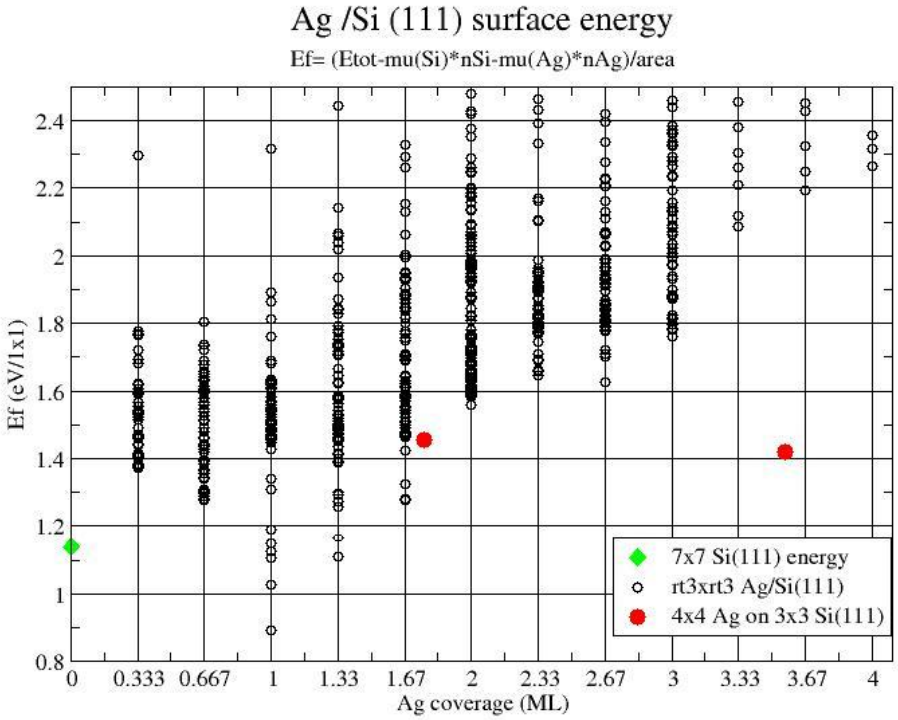

Figure 5.10 Surface energies for rt3xrt3 Ag/Si(111) reconstruction, Ag films on Si (111) surface and 7x7 Si(111). The Ag films on Si surface models are calculated on a unit cell of 4x4 Ag (111) FCC films on top of 3x3 Si(111) substrates

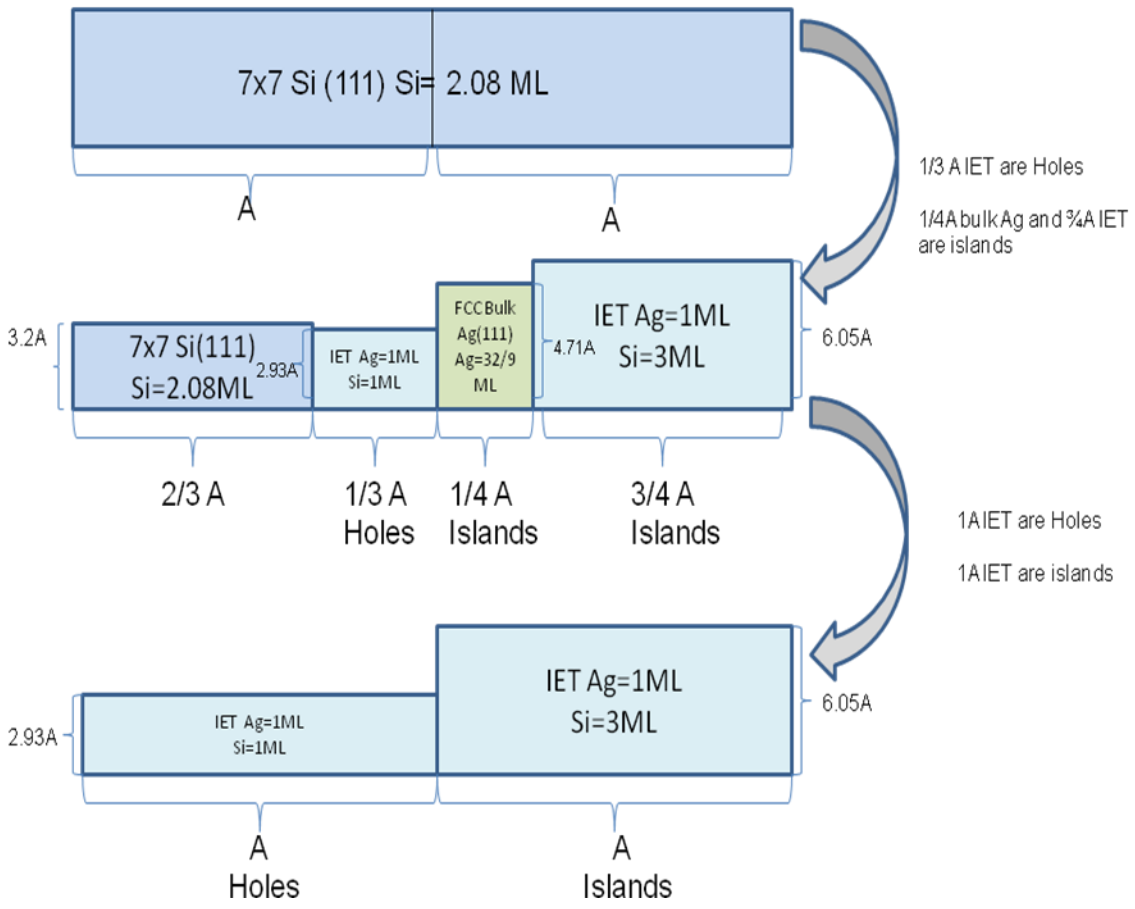

Figure 5.11 the evolution from 7x7 to R=3 and R=1 process. In the first step, the 7x7 Si(111) surface are transformed into a metastable interim state of holes and islands with R_{IH}=3. The Islands are composed of pure Ag films and IET reconstructed structure. The holes are just IET structure with 1ML less Si bilayer than the IET on the islands. Finally both islands and holes become the IET structure with R_{IH}=1.

5.6 Structure of Ag/Si (111)-(3x1) surface reconstruction

for decades. One prototype of the metal-induced silicon surfaces is the silver-silicon interface. The study of Ag/Si (111)-(3x1) has also gained many attentions, and many models have been proposed, such as honeycomb chain-channel (HCC) model, double-π-bonded chain (DπC) model and the '650650' model. In all the well-accepted models, the 3x1 phases of lowest surface energy are of the Ag coverage of 1/3ML and they were all built with known building blocks instead of global optimization. However, we found the surface energy for a model with Ag coverage of 2/3ML and Si coverage of 1ML is energetically more favorable than the HCC models. We conducted a global optimized structures search by using our variable-number Genetic Algorithm (GA) using first-principle calculation. In most of the surfaces reconstructions, the coverages sometimes are not clearly specified, and there may be many possible coverages. In this work, we searched the Ag/Si(111)-(3x1) structures with Ag coverages ranging from 1/3ML to 2 ML, and Si coverages from 1/3ML to 2ML. There are totally 36 combinations of Ag and Si coverages that have been gone through with the GA search.

Although in the experiments the 3x1 phase was observed by desorbing Ag from the Ag/Si(111)-rt3xrt3 phase with annealing around T> 893 K, the average Ag coverage must be less than 1 ML, however, we still went through the Ag coverage up to 2 ML in order to rule out the possible high coverages. The traditional GA normally relaxes the structures with classical potentials like tightbinding potentials and empirical potentials. The GA search may lose some good structures due to the defects of the classical potentials. We improved our GA by incorporating first-principle calculations into the structural relaxations. The first-principle calculations were carried out within the local density approximation (LDA) to density-functional theory (DFT) using projector-augmented-wave (PAW) potentials, as implemented in the Vienna ab-initio Simulation Package (VASP). The reference configuration of 3d104s1 is used for generating Ag PAW potential. The kinetic-energy cutoff was set to be 250 eVand the 1x3 Monkhorst-Pack grid was used to sample the surface Brillouin zone. The Si bulk lattice of 5.41A was used for all the calculations. The Ag/Si(111) surface was modeled by a repeating slab with a reconstructed layer , 2 Si bilayers passivated by

hydrogen at the bottom at a Si-H bond length of 1.51 A, and a vacuum layer of about 10 A along the direction normal to the

surface. The silicon atoms in the bottom 2 bilayers and hydrogen atoms are kept fixed at the crystalline positions and only the Si and Ag in the reconstructed layer are relaxed. The stop criterion of the forces is below 0.01 eV/A. After the relaxation, the surface energy was calculated as below

$$Esurf=(Etotal - Nsi \times \mu si - NAg \times \mu Ag - Esub)/3$$

The Etotal is the total energy of the system relaxed by VASP. Nsi and NAg are the number of Siand Ag in the reconstruction layer. μsi and μAg are the chemical potentials of Si and Ag, and they are all set to the bulk energy of Si. The Esub is the energy of the 2 Si bilayers and H monolayer. The final result is divied by 3 on order to get the surface energy per 1x1 unit cell. In each generation of the GA search, the surface energies are calculated and compared as scores for each structures.

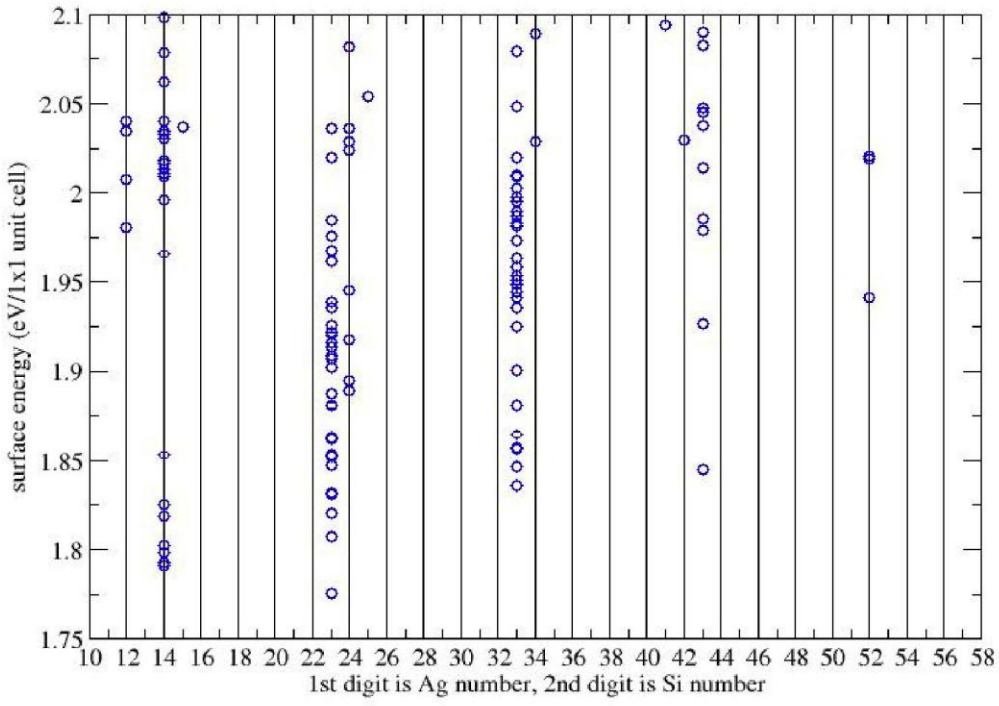

Figure 5.12. Formation energies for the 3x1 Ag/Si(111) structures, the first digit is the Si atoms and 2nd is Ag atoms number within 3x1 unit cell.

The energies of all the final structures with different Ag and Si coverages are presented in the graph above. The x axis labels consist of 2 digits, with 1st being the Ag number and 2nd being the Si atomsnumber inside the 3x1 unit cell, and the y-axis is the surface energy per 1x1 unit cell. For example, the points with 23 on x-axis have 2 Ag atoms and 3 Si atoms inside the 3x1 unit cell, which mean the Ag coverage of 2/3 ML and Si coverage of 1 ML. As we can see, the model with 2/3ML Ag coverage has lower surface energy than the one with 1/3 ML Ag. The one with 1/3 ML Ag coverage that has lowest surface energy is typical Honeycomb Chain-Channel (HCC), and we found it even better than the HCC model proposed by Steven Erwin. The HCC models have a Si honeycomb ring and a Ag adatom on the channel. The Ag adsorption site from the Erwin's model is at T4, and the one we found with GA is also the HCC model with Ag atom resided at âΓ site. The lowest surface energy model is the one with 2/3 ML Ag coverage and Si coverage of 1 ML, and it's about 20 meV lower in surface energy than the 1/3ML Ag coverage HCC model. The 2/3 ML Ag coverage model can be viewed as a 1/3ML Ag and 4/3ML Si with the Si atom next to the Ag replaced by another silicon atom and it also remain a honeycomb ring. The other model with Ag coverage higher than 1ML have a much higher surface energy and increase as the Ag coverage increases. The results are consistent with the general idea that Ag/Si(111)-(3x1) has less Ag coverage than the Ag/Si(111)-(rt3xrt3).

In conclusion, we did a Ag-induced Si(111) 3x1 surface reconstruction search with our variablenumber GA with ab-initio relaxation. A model with 2/3 ML Ag and 1Ml Si coverage has been found and it has lower surface energy than the widely accepted HCC model with only 1/3 ML Ag coverage. We also found the optimized HCC model with 1/3 ML Ag coverage as the 2nd lowest energy structure.

References of 5

[1] V.G. Lifshits, A.A. Saranin, and A.V. Zotov, *Surface Phases on Silicon: Preparation, Structures, and Properties* (John Wiley & Sons, Inc., West Sussex, England, 1994).

[2] K. Spiegel, Surface Sci. **7**, 125 (1967).

[3] A. Shibata, H. Kimura, and K. Takayanagi, J. Vac. Sci. Technol. **B 12**, 2026 (1994).

[4] A. Shibata, Y. Kimura, and K. Takayanagi, Surface Sci. **303**, 161 (1994).

[5] A. Shibata, Y. Kimura, and K. Takayanagi, Surface Sci. **275**, L697 (1992).

[6] K.J. Wan, X.F. Lin, and J. Nogami, Phys. Rev. B **47**, 13700 (1993).

[7] A. Shibata and K. Takayanagi, Jpn. J. App. Phys. **32**, 1385 (1993).

[8] I. Mochizuki, R. Negishi, and Y. Shigeta, J. Phys: Condens. Matter. **61**, 1056 (2007).

[9] H. Aizawa, M. Tsukada, N. Sato, and S. Hasegawa, Surface Sci. **429**, L509 (1999).

[10] N. Sato, T. Nagao, and S. Hasegawa, Surface Sci. **442**, 65 (1999).

[11] Y.G. Ding, C.T. Chan, and K.M. Ho, Phys. Rev. Lett. **67**, 1454 (1991).

[12] N. Yoshimichi, Y. Kondo, J. Nakamura, and S. Watanabe, Phys Rev. Lett. **87**, 156102 (2001).

[13] I. Matsuda, H. Morkawa, C. Liu, S. Ohuchi, S. Hasegawa, T. Okuda, T. Kinoshita, C. Ottaviani, A. Cricenti, M. D'angelo, P. Soukiassian, and G. Le Lay, Phys. Rev. B **68**, 005407 (2003).

[14] K. Sakamoto, T. Suzuki, K. Mawatan, K. Kobayashi, J. Okabayashi, K. Ono, N. Ueno, and M. Oshima, Phys. Rev. B **73**, 193303 (2006).

[15] H.M. Zhang, J.B. Gustafsson, and L.S.O. Johansson, J. Phys: Conf. Series **61**, 133 (2007).

[16] H.M. Zhang, J.B. Gustafsson, and L.S.O. Johansson, Phys. Rev. B **74**, 201304(R) (2006).

[17] B. Ünal, F. Qin, Y. Han, D.J. Liu, D. Jing, A.R. Layson, C. Jenks, J.W. Evans, and P.A. Thiel, Phys. Rev. B **76**, 195410 (2007).

[18] I. Horcas, R. Fernandez, J.M. Gomez-Rodriguez, J. Colchero, J. Gomez-Herrero, and A.M. Baro, Rev. Sci. Instr. **78**, 013705 (2007).

[19] W. Kohn and L.J. Sham, Phys. Rev. A **140**, 1133 (1965).

[20] P. Hohenberg and W. Kohn, Phys. Rev. B **136**, 864 (1964).

[21] G. Kresse and J. Joubert, Phys. Rev. B **59**, 1758 (1999).

[22] G. Kresse and J. Hafner, Phys. Rev. B **47**, 558 (1993).

[23] A. Belianinov, B. Ünal, N. Lu, K.-M. Ho, C.-Z. Wang, M.C. Tringides, and P.A. Thiel, in preparation (2010).

[24] K. Oura, V.G. Lifshits, A.A. Saranin, A.V. Zotov, and M. Katayama, *Surface Science. An Introduction.* (Springer, Berlin, 2003).

Chapter 6. ELECTRONIC PROPERTIES OF [112] SI/GE AND GE/SI CORE/SHELL NANOWIRES

In this chapter my works are divided into 3 parts. The first part is 6.1 and it's our paper *Charge localization in [112] Si/Ge and Ge/Si core/shell nanowires*, published on Journal of Physics D: Applied Physics, 2010, 275404, by Nuo Liu, Yan-Rong Li, Ning Lu, Yong-Xin Yao, Xiao-Wei Fang, Cai-Zhuang Wang and Kai-Ming Ho. In this part I constructed the structural models for core/shell nanowires based on silicon nanowires and calculated the electronic properties of the nanowires, including band gaps and charge spatial distribution. The second part is another paper *Strain effects in Ge/Si and Si/Ge core/shell nanowires*, by Nuo Liu, Ning Lu, Yong-Xin Yao, Yan-Rong Li, Cai-Zhuang Wang and Kai-Ming Ho, which has been submitted. In this paper, I did the DFT calculation of the nanowires under different strains, both compressive and tensile strains andalso analyzed the 2 facets' effects on the band structures based on PDOS results. The third part is the draft *Aspect ratio modulation effect in[112] Ge/Si core/shell nanowires*, by Ning Lu, Nuo Liu, Yong-Xin Yao, Yan-Rong Li, Cai-Zhuang Wang and Kai-Ming Ho which will be submitted soon. I also did some ab-initio calculations of the electronic properties like band structures for nanowires with different aspect ratios.

6.1 Charge localization of [112] Si/Ge and Ge/Si core/shell nanowires

6.1.1 Introduction

Nanowires (NWs), which exhibit quantum confinement effect (QCE) perpendicular to the growth direction and periodic band structures parallel to the axial direction, play an increasingly important role in nanotechnology for their use as building blocks in ballistic field-effect transistors [1-5], sensors [6-8], detectors [9,10], light-emitting diodes [11-13] and solar cells [14-17]. NWs of Si have been one of the focuses in experiments because they are easy to integrate into Si technology. Nevertheless, device performances are limited by two main factors [18]: (1) metal contacts to single-component NWs lead to Schottky barriers; (2) scattering from charge dopants decreases the mobility of the carriers. However, in 2005, Lu *et al* [2] demonstrated that low bias ballistic transport can be achieved in undoped Si/Ge (Ge/Si) core/shell NWs.

Recent advances in ‘bottom-up’ techniques have expanded the range of device fabrication to a wide variety of NW heterostructures which can be achieved at the individual defectfree device level in a vapour–liquid–solid process. Axial and radial NWs are considered to be very promising in many frontier fields among them. The potential application at the individual device level in a controlled fashion has triggered a surge of experimental and theoretical studies. Axial NWs, or NW superlattice, have been obtained in Si/Ge [1,19], InN/GaN [20,21] and InGaAs/GaAs [22]. Radial NWs such as Si/Ge (Ge/Si) [5]and GaN-based [13] InP/GaP core/shell [23] have been fabricated successfully. Among these NWs, Si/Ge (Ge/Si) core/shell NWs show a substantially higher performance as field-effect transistors and low-temperature quantum devices [1,24,25]. Optimization and application of nanodevices require the knowledge of electronic states and QCEs. Several computational studies using the first-principles method have been reported for structures, electronic states and spatial carrier confinement of hydrogen-passivated Si/Ge (Ge/Si) core/shell NWs along the [111], [110] and [100] orientations having cross-sections of cylindrical [26-28], hexagonal [129], square [2,30] and diamond shapes [28,29]. A type II band lineup for these core/shell NWs has also been reported [2,29]. It has also been shown that the electronic properties and QCE can be modulated by the size, geometry, orientation and composition of the core/shell NWs [26-32]. However, only a few studies have been carried out on [112] Ge/Si core/shell NWs and the experiments observed that the [112] crystallographic orientation is one of the most preferred directions for NW growth [33,34]. Motivated by the recent progress in experimental and theoretical studies, we have performed a first-principles study for Ge/Si and Si/Ge core/shell NWs along the [112] direction in order to study the electronic structures and QCE in these NWs. Such information is desirable from the point of view of fundamental physics and device applications.

6.1.2 Calculation Methods

All calculations were carried out using density-functional theory (DFT) with the plane wave based Vienna Ab-initio Simulation Package (VASP) [25,26]. The exchangecorrelation energy of DFT was treated in the local density approximation (LDA). The ionic potentials are described by Vanderbilt

pseudopotentials [27]. The calculations were performed for H-terminated [112] Si/Ge and Ge/Si core/shell NWs. The surface states are removed from the band gap with hydrogen passivation. The lattice constants of the tetragonal supercell in the *x–y* plane are taken as *a* and *b*, with *c* along the *axial* axis. Plane waves are included up to a kinetic-energy cutoff of 260 eV which is sufficient for both structure optimizations and analysis of the resulting electronic structures. A $1 \times 1 \times 6$ Monkhorst-Pack special *k* point grid is used for the Brillouin-zone integration with the Methfessel–Paxton smearing method [38] in total-energy calculations. The adopted smearing width is 0.1 eV for the atomic relaxation and 0.05 eV for the accurate band structure analysis and density of states (DOS) calculations. All atomic positions and lattice constants are optimized using the conjugate gradient method where total energy and atomic forces are minimized. The calculations are converged in energy to 10^{-4} eV. The unit cell is chosen so that the distance between the wire and its replica is more than 10 Å, so that their interactions are negligible.

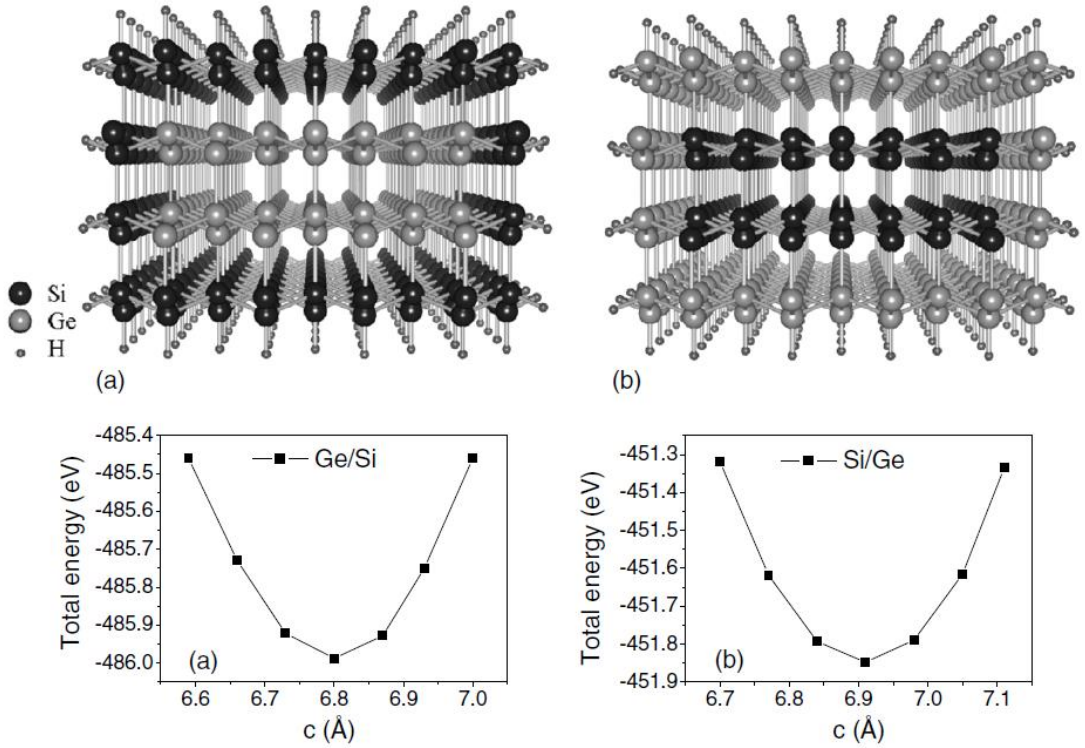

Figure 6.1 Perspective view of the structures of the hydrogen-passivated (*a*) Ge/Si and Si/Ge (*b*) core/shell NWs of eight unit cells along the axis direction. (*c*) and (*d*) are the total energy as a function of the axial lattice constant of a unit cell. Dark grey balls are Si atoms, light grey balls are Ge atoms and grey small balls are H atoms, respectively.

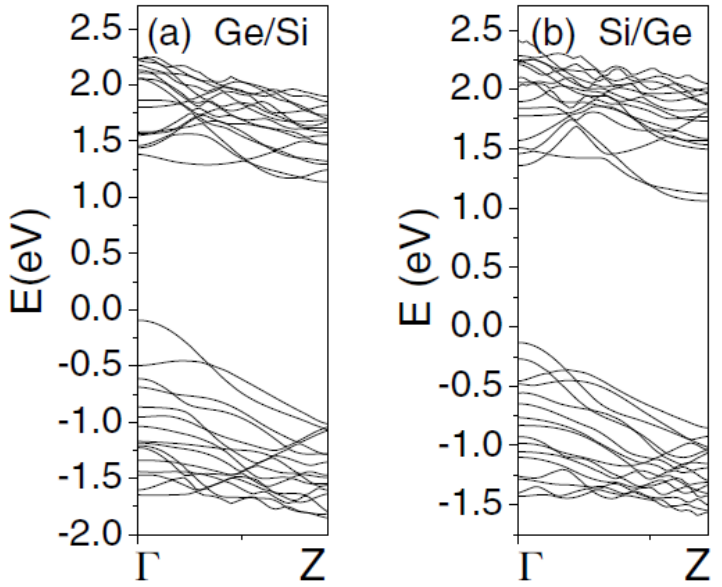

Figure 6.2. Band structures of the (*a*) Ge/Si and (b) Si/Ge core/shell NWs.

6.1.3 Structures for the core/shell nanowires

The geometries of hydrogen-passivated Ge/Si and Si/Ge core/shell NWs are based on the [112] silicon NW structures found by a global unbiased search with Genetic Algorithm in our previous works [39], as shown in figure 6.1. Note that the two structures have the same total number of atoms with *N*Si*(*Ge/Si*)* = *N*Ge*(*Si/Ge*)* and *N*Ge*(*Ge/Si*)* = *N*Si*(*Si/Ge*)*, where *N*Si and *N*Ge represent the number of Si and Ge atoms. The axial lattice constants of the core/shell NWs are optimized by minimizing the total energy of the NWs with respect to the axial lattice constants *c* while allowing all atoms in the NWs to relax by the technique of conjugate gradient. The total energy as a function of the axial lattice constant is shownin figures 6.1(*c*) and (*d*), respectively, for Ge/Si and Si/Ge core/shell NWs. The optimum axial lattice constants for the two structures are listed in table 6.1. For the two NWs studied in this work, we found that *c* is 6.80Å for the Ge/Si core/shell NW with a diameter (defined as the diagonal length in the cross-section of the NW) of 6.91Å and *c* is 27.62Å for the Si/Ge one with a diameter of 21.97 Å. This implies that the axial and radial expansion for the latter is larger than that for the former although the total number of atoms of the two structures is the same. Actually, there is about 4% mismatch between Si and Ge bulk lattice constants. For the Ge/Si core/shellNW, the core is compressed in all the directions and the radial stress in the Si shell is tensile. In contrast, the core is tensile in all the directions and the radial stress in the Si shell is compressive for the Si/Ge one. Thus, there is a pseudomorphic strain at the interface. Consequently, the strain relaxation modifies the bond length and angle in order to accommodate the lattice constant mismatch.

Table 6.1. Calculated optimized lattice constant *c* along the [1 1 2] direction in this work: *d* is the diameter of the NWs; *E*g the effective band gap; m_n^* and m_p^* are the predicted effective masses of electron and hole; *N*Si and *N*Ge are the number of Si atoms and Ge atoms in the given NWs, respectively. *d* is defined as the largest distance between two atoms in the same cross-sectional plane.

Core/shell NW	*c* (Å)	*d* (Å)	E_g (eV)	m_n^* (m_0)	m_p^* (m_0)	N_{Si}	N_{Ge}	Type of band gap
Ge/Si	6.80	20.549	1.232	0.26	−0.22	52	20	Indirect
Si/Ge	6.91	21.965	1.193	0.30	−0.23	20	52	Indirect

6.1.4 Results and discussion

Electronic band structures for the Ge/Si and Si/Ge core/shell NWs from our calculations are plotted in figure 6.2. The band gaps are found to be indirect in both NWs (*E*g = 1.23 eV for Ge/Si and 1.19 for Si/Ge core/shell NWs, respectively). The slightly larger band gap in the Ge/Si core/shell NW could be attributed to the relatively larger number of Si atoms in the Ge/Si NW than that in the Si/Ge NW, since the band gap of the bulk Si is larger than that of the bulk Ge. The band gaps in the NWs are also larger than the bulk band gaps of Si and Ge apparently due to QCE. The indirect gaps indicate that the NWs may not be efficient in light emitting and absorption. The effective masses for the holes and electrons are estimated using the bands near the top of the valence band at the Γ point (the centre of the Brillouin zone) and the bottom of the conduction band near the Z point (the boundary of the Brillouin zone), respectively. Table 6.1 shows that the effective masses of holes (m_p^*) for the Ge/Si and Si/Ge core/shell NWs are smaller than that of electrons. The effective masses of the holes in the NWs are also smaller than that of the holes in the bulk Si and Ge crystals. The results of m_p^* and m_n^* for the Ge/Si NW obtained from our calculations are similar to the results of Pekoz *et al* [31] for [111] and [110] oriented Ge/Si NWs with diamond-shaped cross-section.

The electronic DOS are plotted in figure 6.3. For the Ge/Si core/shell NW (see figure 6.3(*a)),* the valence states consist of mainly the Si 3p states, and the conduction states near *EF* are mainly Si 3s and 3p. This is due to the fact that the number of Si atoms in this NW is much larger than that of Ge atoms (*N*Si/*N*Ge = 52/20*)*. There are also Ge 4p contributions to the total valence states and Ge 4s and 4p to the conduction states near the *EF* due to a Si–Ge hybridization.

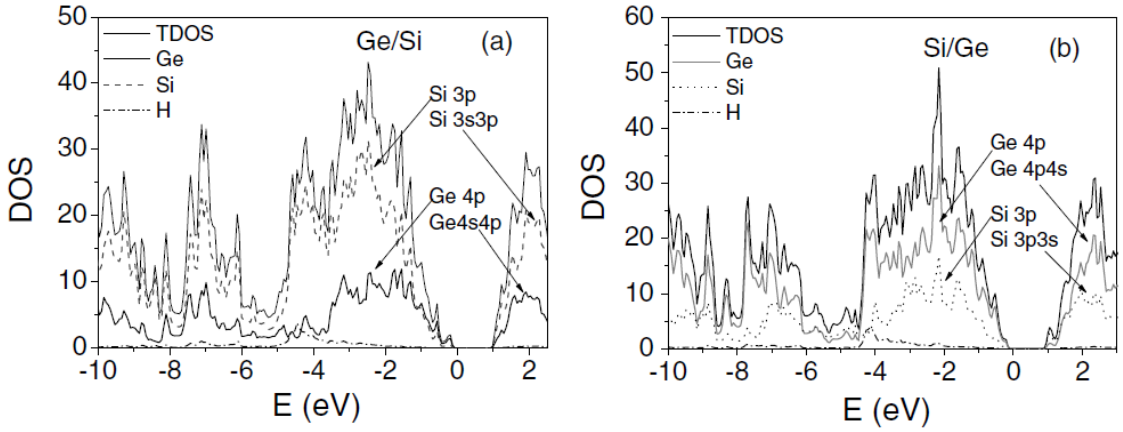

Figure 6.3. DOS (black solid line) in the NWs: total density of states (TDOS, black solid line), Ge atoms (grey solid line), Si atoms (dashed line) and H atoms (dash dot line); (*a*) Ge/Si core/shell NW and (*b*) Si/Ge core/shell NW.

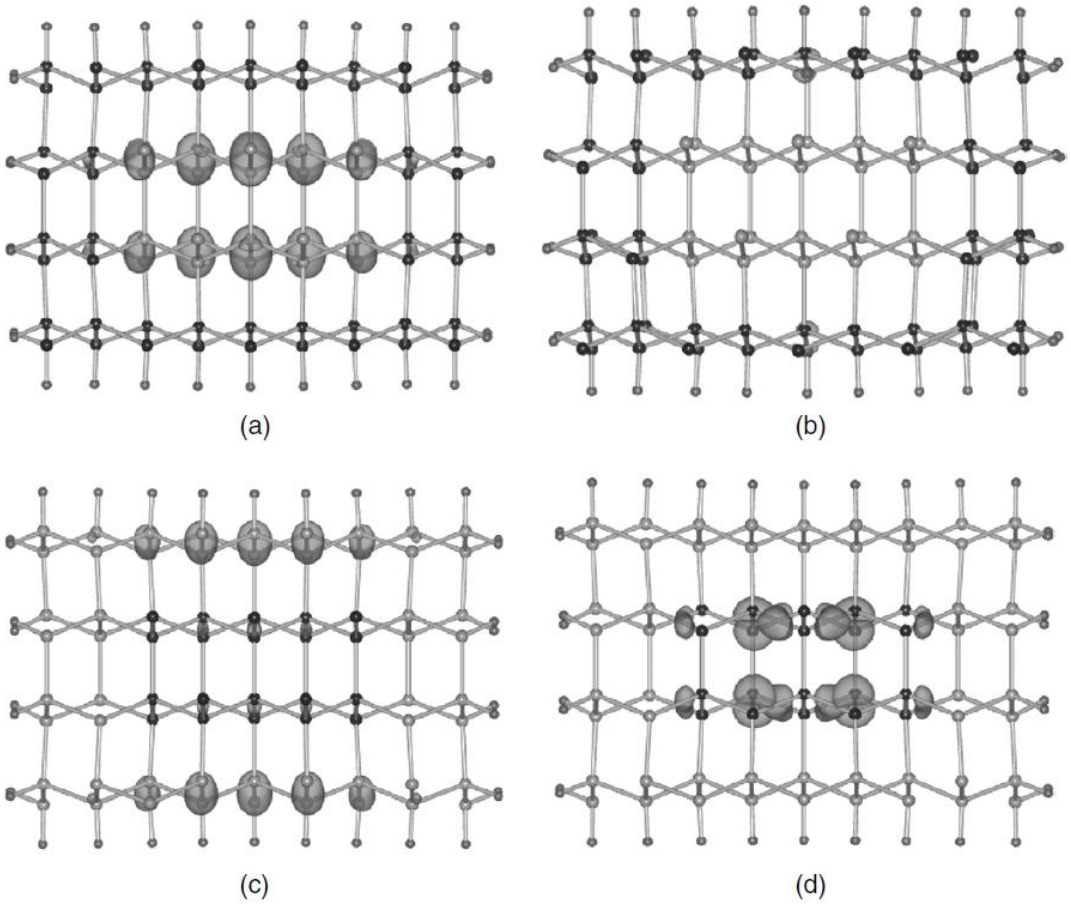

Figure 6.4. Cross-sectional view of the distribution of charge density plots at the isovalue of 0.002*e* for the top of valence band ((a) and (c)) and the bottom of conduction band ((b) and (d))in the Ge/Si core/shell structure and the Si/Ge one, respectively: (*a*) and (*b*) Ge/Si core/shell; (*c*) and (*d*) Si/Ge core/shell.

To gain more insights into the nature of the electronic states at the conduction band minimum (CBM) and valence band maximum (VBM), figure 6.4 presents the distribution of charge density corresponding to the electronic states at the CBM and VBM in real space. The charge densities are plotted at an isovalue of 0.0018*e* on the cross-section of the NWs. The distribution of charges at the VBM in the Ge/Si NW is mostly in the Ge core region (figure 6.4(*a)),* while charges at the CBM are mainly on the Si shell (figure 6.4(*b)).* Other studies on Ge/Si core/shell NWs along the [111] and [110] directions have shown a similar trend [29]. Since the electron cloud of the VBM is shared by Ge atoms in the core (see figure 6.4(*a)),* the electronic states of the VBM are confined in the core region.

The spatial charge density distributions strongly suggest that the lineup of the band structure of the Ge/Si core/shell NW is type II, i.e. $E_c^{Ge} > E_c^{Si}$ and $E_v^{Ge} > E_v^{Si}$. The determination of the band offsets from first principles cannot be achieved accurately from the average local potential by the doublemacroscopic average technique because it is impossible to get it far enough from the interface (bulk-like regions) for NWs. The schematic band lineup of the core/shell NW is shown in figure 6.5(*a*). The QCE due to band offsets can be realized in the Ge/Si core/shell NW along the [1 1 2] direction. It is noted that the band lineup shown in figure 6.5(*a*) is similar to the band lineup of the Ge/Si core/shell NWs in cylindrical shape along the [1 1 1] and [1 0 0] directions reported in [2].

For the Si/Ge core/shell NWs, figures 6.4(*c*) and (*d*) show the charge density distribution for the electronic states of the CBM and VBM. It appears that the charge localizations in the Si/Ge NW are different from that of the Ge/Si NW. We find that the charge distributes on Si atoms in the core region at the CBM and the charge for the VBM resides on Ge atoms in the shell region. This means that the effective band offsets relationship is also $E_c^{Ge} > E_c^{Si}$ and $E_v^{Ge} > E_v^{Si}$ as the case in the Ge/Si core/shell structure. Consequently, the qualitative band lineup of the NW is also defined as type II between Si and Ge. A schematic plot of the band lineup in the Si/Ge NW is given in figure 6.5(*b*).

It is worth noting that the quantum wells induced by the band offsets for a one-dimensional electronic gas (1DEG) at the bottom of the conduction band are located in the Si region for the two core/shell NWs. In other words, there are strong QCEs on the electronic states on Ge and Si. As a consequence, the electronic states can be filled with electrons near the CBM in the quantum well formed in the Si region. Thus, with electrons injected into the one-dimensional quantum well and 1DEG can be formed because of the energy band alignments although the NW is undoped, leading to the phenomenon of self-doping in the region. Noting that there is no scattering from charge dopants inside the one-dimensional quantum well, the core/shell structures can be used as the channel material for carriers with high mobility in devices working as a depletion type device. The second advantage for the core/shell NWs is the high average mean time. The electrons at the VBM can be excited to the CBM with increasing temperature, driving the separated one-dimensional hole gas (1DHG) into Ge and 1DEG into Si. The separation of charge density is very valuable for solar cells because the carrier collection efficiency can be improved with fewer bulk recombinations than in traditional p–n junction devices [1,2,40]. The third merit application is for the high electron mobility heterostructures like high electron mobility transistors (HEMTs). The type II band lineups make it possible that the carrier concentration in the quantum wells can be modulated by selected doping in the shell region. For the Ge/Si NW, p-type doping in the Si shell region generates a high concentration of holes in the Ge core and forms a depleted Si shell layer. With no dopant impurities, a high mobility is realized in the Ge core. Similarly, for the Si/Ge NW, n-type modulated doping in the Ge shell region can generate high mobile conducting electrons in the one-dimensional quantum well in the Si core.

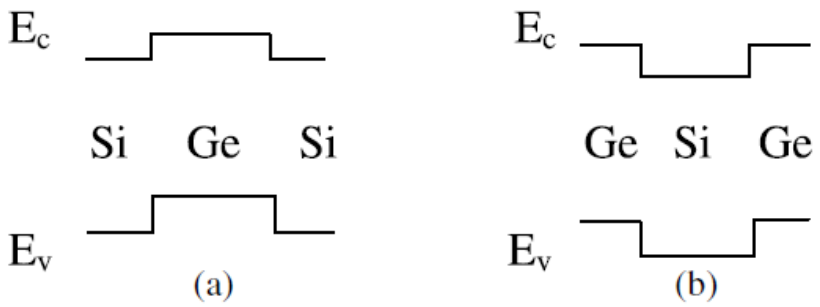

Figure 6.5. Band lineup models for (*a*) Ge/Si and (*b*) Si/Ge core/shell NWs along [112] orientation.

6.1.5 Summary

In conclusion, we have studied two possible SiGe core/shell NWs along the [112] orientation based on first-principles calculations. The band gaps are found to be indirect and larger than the bulk band gaps of Si and Ge apparently due to the QCEs in both NWs. A detailed analysis of the charge density distribution shows that the electrons are strongly localized on Si atoms in the CBM and on Ge atoms in the VBM for the two structures. The band offsets in the NWs are strongly modified by the QCE. The quantum well confinement effect in these NWs forms a type II lineup of band structures. The applications of core/shell NWs as self-doping channel materials, high efficiency solar cells and high mobility heterostructures are discussed.

References of Chapter 6.1

[1] Xiang J, Lu W, Hu J Y, Wu Y, Yan H and Lieber C M 2006, *Nature* **441** 489

[2] Lu W, Xiang J, Timko B P, Wu Y and Lieber C M 2005 *Proc.Natl Acad. Sci. USA* **102** 10046

[3] Koo S M, Fujiwara A, Han J P, Vogel E M, Richter C A and Bonevich J E 2004 *Nano Lett.* **4** 2197

[4] Cui Y, Zhong Z,Wang D,WangWand Lieber C M 2003 *Nano Lett.* **3** 149

[5] Hashemi P, Kim M, Hennessy J, Gomez L, Antoniadis D A and Hoyt 2010 *Appl. Phys. Lett.* **96** 063109

[6] Zheng G, Patolsky F, Cui Y, Wang W and Lieber C M 2005,*Nature Biotechnol.* **23** 1294

[7] Hahm J and Lieber C M 2004 *Nano Lett.* **4** 51

[8] Cui Y, Wei Q, Park H and Lieber C M 2001 *Science* **293** 1289

[9] Chen K J, Hung F Y, Chang S J and Hu Z S 2010 *J. Electrochem. Soc.* **157** H241

[10] Okyay A K, Nayfeh A M, Saraswat K C, Yonehara T, Marshall A and McIntyre P C 2006 *Opt. Lett.* **31** 2565

[11] Zimmler M A, Voss T, Ronning C and Capasso F 2009 *Appl.Phys. Lett.* **94** 241120

[12] Migas D B and Borisenko V E 2007 *Nanotechnology* **18** 375703

[13] Connors B J, Povolotskyi M, Hicks R and Klein B 2010 *Proc. SPIE* **7597** 75970-10

[14] Tian B, Zheng X L, Kempa T J, Fang Y, Yu N F, Huang J L and Lieber C M 2007 *Nature* **449** 885

[15] Kempa T J, Tian B, Kim D R, Hu J S, Zheng X L and Lieber C M 2008 *Nano Lett.* **8** 3456

[16] Hagfeldt A and Gr ̈atzel M 1995 *Chem. Rev.* **95** 49

[17] Lee M R, Eckert R D, Forberich K, Dennler G, Brabec C J and Gaudiana R A 2009 *Science* **324** 232

[18] Zheng G F, Lu W, Jin S and Lieber C M 2004 *Adv. Mater.* **16** 1890

[19] Lauhon L J, Gudiksen M S, Wang D and Lieber C M 2002 *Nature* **420** 57

[20] Qian F, Li Y, Grade ̆cak S, Park H G, Dong Y J, Ding Y,Wang Z L and Lieber C M 2008*Nature* **7** 701

[21] Kim Y H, Park H J, Kim K, Yun W S, Lee J W and KimMD 2009 *Appl. Phys. Lett.* **95** 033112

[22] Hei ß M, Gustafsson A, Conesa-Boj S, Peir ́o F, Morante J R, Abstreiter G, Arbiol J, Samuelson L and Morral A F 2009 *Nanotechnology* **20** 075603

[23] Tateno K, Zhang G, Nakano H 2008 *J. Cryst. Growth* **310** 2966

[24] Xiang J, Vidan A, Tinkham M, Westervelt R M and Lieber C M 2006 *Nature Nanotechnol.* **1** 208

[25] Hu Y, Churchill H O, Reilly D J, J Xiang and Lieber C M 2007 *Nature Nanotechnol.* **2** 622

[26] Musin R N and Wang X Q 2005 *Phys. Rev.* B **71** 155318

[27] Musin R N and Wang X Q 2006 *Phys. Rev.* B **74** 165308

[28] Nduwimana A, Musin R N, Smith A M and Wang X Q 2008 *Nano Lett.* **8** 3341

[29] Migas D B and Borisenko E V 2007 *Phys. Rev.* B **76** 035440

[30] Yang L, Musin R N, Wang X Q and Chou M Y 2008 *Phys.Rev.* B **77** 195325

[31] Pek ̈oz R and Raty J Y 2009 *Phys. Rev.* B **80** 155432

[32] Amato M, Palummo M and Ossicini S 2009 *Phys. Rev.* B **80** 235333

[33] Ma D D D, Lee C S, Au F C K, Tong S Y and Lee S T 2003 *Science* **299** 1874

[34] Wu Y, Cui Y, Huynh L, Barrelet C J, Bell D C and Lieber C M 2004 *Nano Lett.* **4** 433

[35] Kresse G and Hafner J 1993 *Phys. Rev.* B **47** 558

[36] Payne M C, Teter M P, Allen D C, Arias T A and Joannopoulos J D 1992 *Rev. Mod. Phys.* **64** 1045

[37] Vanderbilt D 1990 *Phys. Rev.* B **41** 7892

[38] Methfessel M and Paxton A T 1989 *Phys. Rev.* B **40** 3616

[39] Lu N, Ciobanu C V, Chan T L, Chuang F C, Wang C Z and Ho K M 2007 *J. Phys. Chem.* C **111** 7933

[40] Nduwimana A and Wang X Q 2009 *Nano Lett.* **9** 283

6.2 Strain effects in Ge/Si and Si/Ge core/shell nanowires

6.2.1 Introduction

Core/shell heterostructure nanowires (NWs) have been extensively studied in recent years,[1-9] as they are promising alternatives to planar heterostructures like MOSFETs and photon devices, due to their important performance such as higher carrier mobilities and unique electronic structures. Moreover, the electronic and optical properties of core/shell NWS can be tailored using band structure engineering. Ge/Si and Si/Ge core/shell NWs have the advantage of compatibility with conventional Si processes and potential for fabrication of future NW-based devices in many frontier fields. Many experimental and theoretical studies showed that low bias ballistic transport [2] and quantum confinement effect [3-9] can also be realized in Ge/Si and Si/Ge NWs by varying the size, geometry, orientation and composition of the core/shell NWs, Several computational studies using first-principles method have been reported for the structures, electronic states, spatial carrier confinement of hydrogen-passivated Si/Ge (Ge/Si) core/shell NWs along [111], [110], [100] and [112] orientations. The type II band lineup and charge separation in space for these core/shell NWs has also been reported .[1,2,6,10]

The use of strain is a powerful method through bottom-up approaches to tailor the electronic properties [11-13] and effective masses which determines incidence velocity and drain current in MOSFET. In addition, strain is desirable to reveal new physical mechanisms in the NWs. Recent studies showed that [110] Si NWs have a direct to indirect band gap transition under tensile strain [14]and the charge separation can also be realized in [011] Si NWs by applying partial strain.[15] However, few attention have been paid to [112] Ge/Si and Si/Ge core/shell NWs even though the [112] crystallographic orientation being one of the most preferred Si NWs.[16,17]

6.2.2 Calculation methods

Motivated by the recent progress in experimental and theoretical studies, in this work we investigated strain effects on the electronic structures in [112] Ge/Si and Si/Ge core/shell NWs in the future nano-devices. Our first-principle axial direction, and more than 10 Å vacuum spaces is used in the lateral directions to isolate the interactions between the NW and its replica. Six Monkhorst-Pack k points are used to sample the one-dimension Brillouin Zone along axial direction with Methfessel-Paxton smearing

method[20] in the total-energy calculations. The atomic positions and lattices parameters were fully optimized using the conjugate gradient relaxation. The calculations were converged to the order of 10^{-4} eV per cell. The adopted smearing width is 0.1 eV for the structure relaxation and 0.05 eV for the density of states calculations. Tests have been performed to make sure that all of the results are fully converged with respect to the energy cutoff, k-point sampling and vacuum spacing.

6.2.3 Electronic properties of the Si/Ge nanowires

We constructed the Ge-core/Si-shell and Si-core/Ge-shell NWs based on the [112] silicon NW structures found by genetic algorithm search in our previous works.[21] The axial lattice constants of the core/shell NWs are optimized by minimizing the total energy of the NWs by the conjugate-gradient (CG) method. The cross section of the NWs is a rectangle with {111} and {110} facets. Following the notation in our previous studies of Si NWs, we denote a (m, n) NW as a core/shell NW that has m layers parallel to the {110} facet and n layers parallel to {111} facet. The total number of atoms in the unit cell are 72 and 56 for (9, 4) and (7, 4) NWs, respectively. The core consists of 20 atoms. Starting from the relaxed structure, we applied uniaxial compressive and tensile strains ($\eta<0$ and $\eta>0$, respectively) by scaling the axial lattice constant of the wire. In this work, we will discuss in detail the (9, 4) and (7, 4) Ge/Si and Si/Ge core/shell NWs with [112] axial direction under strains from η = -3% to +3%.

The electronic energy band structures of the (9, 4) and (7, 4) Ge/Si and Si/Ge core/shell NWs under different strains are studied. The fully relaxed structures at zero strain have their valence band maximum (VBM) at the Γ point and the conduction band minimum (CBM) near the Z point, which make the band gap indirect. Under strain the VBM is still located at the Γ point, but the strain has noticeable effect on the CBM. There are two minima in the lowest conduction band, as shown in Figure 6.6(a), one near the Z point (CBM1) and another close to the Γ point (CBM2) which are quite sensitive to compressive strain. With increasing compressive strain, the CBM1 shifts upward slowly in energy while CBM2 shifts down for the structures studied here. As the strain reaches η = -3%, the CBM2 becomes lower than CBM1, resulting in a quasi direct band gap. In contrast, the tensile strain density function theory (DFT) calculations were performed using Vienna ab-initio simulation package (VASP) [18] with ultrasoft Vanderbilt pesudopotentials [19] and plane-wave basis sets. The DFT local density approximation (LDA) was applied.

The plane waves approach with kinetic energy cutoff of 260 eV was used. The dangling bonds on the [112] Si/Ge and Ge/Si core/shell nanowires are saturated with hydrogen atoms. The wires were constructed by periodically repeating the unit cell along has no effect on the position of CBM which is always located at the Z point. Figure 6.6 (b) shows the relative positions of CBM at different strains for the (9, 4) and (7, 4) structures, where Δ denotes the ratio of the distances k_Γ-k_{CBM} over k_Γ-k_Z. This ratio is found to be dependent on strain and an indirect to quasi-direct gap transition occurs near η = -3%. It is interesting to note that the changes of band gap type in these [112] structures under compressive strain is different from the previous results for [111] and [110] Si NWs whereas it is the tensile strain drives the NWs to have a direct band gap.[13] The strain-induced indirect to quasi-direct transition is shown in Figure 6.6 (c). The energy difference (ΔE) between CMB2 and CMB1 is used to describe the indirect to quasi-direct transition. A negative (positive) ΔE denotes quasi-direct (indirect) band gap. The horizontal dashed line at ΔE=0 gives a reference of the transition between indirect and quasi-direct band gap. The ΔE of the Ge/Si NW decreases with decreasing the diameter of the NW under η = -3%; ΔE is -0.2038 eV for the (9, 4) Ge/Si structure with diameter of 26.46 Å and changes to -0.1316 eV for the (7, 4) Ge/Si NW with diameter of 17.66 Å. These results demonstrate a noticeable quasi-direct band gap transition in Ge/Si structures with larger diameter. In contrast, for Si/Ge structure, ΔE is only -0.0027 eV and -0.0038 eV for (9, 4) and (7, 4) structures. Therefore, ΔE depends on the diameter and core material.

The variation of the band gap with strain is presented in Figure 6.7. Due to the quantum confinement effects, the gap of the (7, 4) core/shell NWs is bigger than that of the corresponding (9, 4) NWs. Although band gaps are underestimated by DFT calculation, it has been proven to be a sound way of predicting qualitative trends.[22] The slightly larger band gap in the Ge/Si core/shell NW in comparison with that of the Si/Ge NW of the same (m, n) could be attributed to the relatively larger number of Si atoms in the Ge/Si NW. As shown in the graph, the variation of band gap with tensile strain is small. In contrast to the case of tensile strain, we find that indirect to quasi-direct band gap occurs when the compressive stress increase from -2% to -3%. At the same time, the band gaps of Ge/Si core/shell NWs decrease, while that of Si/Ge structures increase because the CBM move upward in energy relative to VBM, especially for the (7, 4) structure.

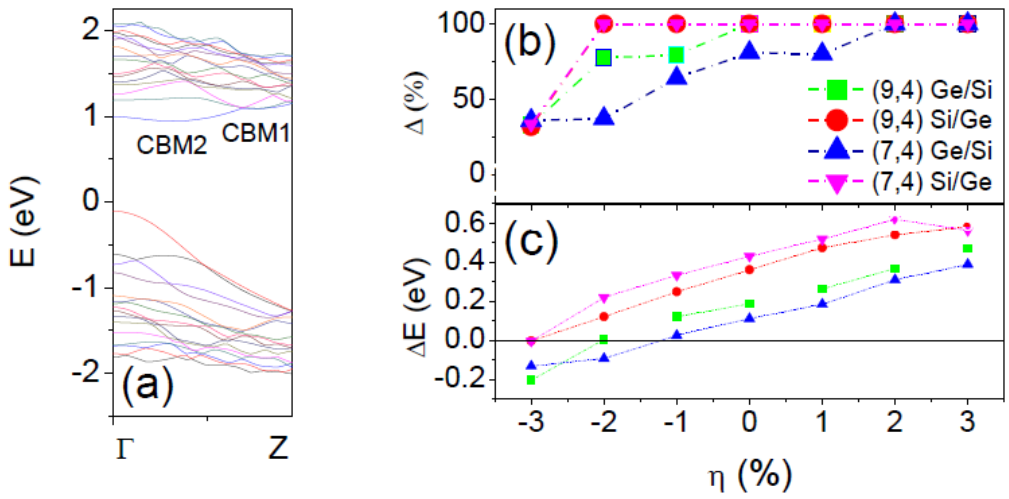

Figure 6.6. (a) The band structures of (9, 4) Ge/Si core/shell NW with -3% compressive strain. (b) The relative position (Δ) of CBM as the function of strain in [112] Ge/Si and Si/Ge core/shell NWs. Δ denotes the ratio of k_Γ-k_{CBM} over k_Γ-k_Z where k_{CBM} is the position of the conduction band minimum (CBM) along Γ to Z (see the band structure plots in FIGURE 6.6). (c) Indirect to quasi-direct band gap difference ΔE with strain, where indirect to quasi-direct transition occurring at ΔE=0 (the horizontal line).

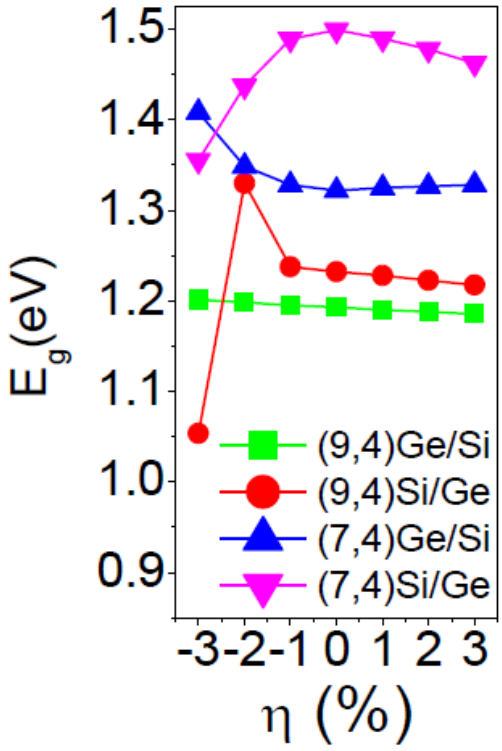

Figure 6.7. Band gap of the Ge/Si and Si/Ge core/shell NWs as the function of strain.

To further investigate the electronic properties under strain, we need to study the effective masses of the carriers. As shown in Figure 6.8, it is found that the electrons effective masses (m_n^*) decrease to small values in indirect band gap region for the studied NWs. The (9, 4) Ge/Si NW has the smallest quasi-direct band gap electrons effective mass, while that of (7, 4) Si/Ge NW are the smallest one in indirect band gap region. The holes effective masses (m_p^*) of (9, 4) Si/Ge and Ge/Si NWs keep almost independent of strain However, the m_p^* of (7, 4) NWs increase with the strain increase from -3 to +3%, and under the same strains (7, 4) Ge/Si NW always has the biggest absolute value of hole effective mass.

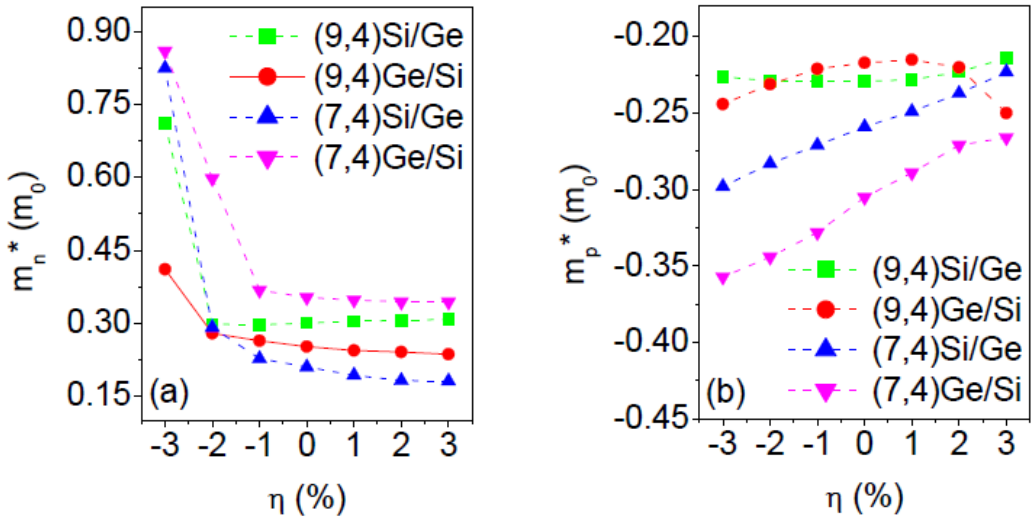

Figure 6.8. Electron effective masses (a) and hole effective masses (b) of the Ge/Si and Si/Ge core/shell NWs as the function of strain.

To obtain more details about the electronic structures of the strained NWs and provide insight into the physical mechanism of the indirect to quasi-direct transition, the projected density of states (PDOSs) are decomposed onto the atoms in core and shell region on the {110} and {111} facets, respectively, as presented in Figure 6.9. In order to get a direct comparison in Ge/Si and Si/Ge NWs, we give the PDOS of the atom at the same position in core and shell region parallel to {111} and {110} facets in (7, 4) NWs, respectively. The effects of the strain on the electronic structure of the NWs can be seen clearly from the shape and the distribution of the PDOS. It is interesting to note that the PDOSs from the atom on the {111} facets in core region (the red line in Figure 6.9) dominate the PDOSs near VBM for Ge/Si NWs with and

without strain. In contrast, the main contribution to the VBM in Si/Ge NWs is from the atoms on the {111} facets in shell region (the green line in Figure 6.9).

It is worthwhile to pay more attention to the PDOSs near CBM since the position of the CBM changes sensitively to the strain. For Ge/Si NWs, the most important features are that the contribution to the CBM from the atoms on the {111} facets in both core and shell regions are strong, while that from the {110} facets in shell region is the weakest. For the NWs with indirect band gap, the contribution to the PDOSs at the CBM is mainly due to the atom on the {111} facets in Si shell region. Contribution to CBM from the atoms on the same facets in Ge core region is also stronger than that on the {110} facets in the core region, as shown in Figure 6.9 (c1) and (d1) respectively. On the other hand, in the case of Ge/Si NWs with quasi-direct band gap (under compressive strain), the PDOSs near the CBM is quite different from that with indirect band gap. It is clear that the most strong contribution to the CBM is from the atoms on the {111} facets in Ge core region, followed by that from the atoms on Si shell of {111} facets and the atoms on the {110} facets in Ge core region (see Figure 6.9 (a1) and (b1)). When the contribution to the PDOS of CBM from atoms on the {111} facets in shell region is stronger than that on the {111} facets in the core region (as the strain $\eta > -2\%$), it is found that the CBM1 located at the Z point in band structures become the CBM and the type of the band gap is indirect. Moreover, the contribution from 4s and 4p orbitals of Ge are responsible for the quasi-direct band gap, while that from the mixture of 3p, 3d and 3s characters of Si atom on {111} facets dominate the states for the indirect band gap. These results suggest that the contribution from the atoms on the {111} facets of Ge control the type of the band gap in Ge/Si NWs.

For Si/Ge NWs, however, the behavior is different from that of Ge/Si NWs (see Figure 6.9 (a2)-(d2)). For all the NWs we studied, the CBM around ~1 eV is mainly governed by the atoms on {111} facets in Si core region. The contribution to CBM from the atoms on the {110} facets in Si core region is also niticible but it is much smaller than that from the {111} facets in Si core region. It is interesting to note that the intensity of the peak corresponding to the contribution of the atoms on {111} facets in Si core region to the CBM in the PDOS increases as the band gap changes from indirect to quasi-direct when the compressive strain is applied. Furthermore, the origin for the changes in the PDOSs near CBM can be understood by comparing the contributions from the 3s orbitals of Si atoms on {111} facets in the NWs with and without

strain. We found that the PDOSs of the Si 3s orbitals near the CBM is stronger in the NWs with indirect band gap and lower in the NWs that exhibit quasi-direct band gap. Therefore, the Si 3s orbitals of the atoms on {111} facets in core region are mainly responsible for controlling the different type of band gap under strain in Si/Ge NWs, and the {111} facets induced effects are the predominant factor of making the strain dependence of the type of the band gap. This is a remarkable and unique property of [112] Ge/Si and Si/Ge core/shell NWs in electronic band structures. Similar characteristics have also been observed in the pure Si NWs band structures.[23,24]

One valuable application is for the photon devices like high efficiency solar cells. It is found that the type II band lineup of the Si/Ge and Ge/Si NWs make the electrons and holes separate in space. Thus, the recombination of electrons and holes in solar cells is minimized. Moreover, the quasi-direct band gap of the strained NWs can decrease the number of phonons participating in the transition and improve the quantum efficiency. We expect that the NWs along [112] direction under compressive strain could allow a greater flexibility in optimizing the cell performance for much higher quantum efficiency in solar cells. Secondly, it is reported that both Si and Ge NWs have been demonstrated as the high charge capacity anode material for the new generation lithium ion batteries.[25,26] The Si/Ge core/shell NWs, not only with the high charge capacity, also with the Si core as an efficient conducting channel, can work as a superior anode material. The Ge shell region has higher resistance due to the lattice defects caused by Li^+ ions storage; however the electrons will mostly go through the Si core region with low resistance because of the type II band lineup. Therefore, it may also have some potential application as the anode material in the Lithium ion battery that is used for portable electronic devices, power tools and electric vehicles. Thirdly, for the application of light emitter, the frequency of light emission can be easily tuned by the strain and the diameter.

6.2.5 Conclusion

In summary, by using first-principle calculations we have studied the electronic band structures of Ge/Si and Si/Ge core/shell NWs along [112] orientation with and without strain. The band gap tunability is strain and size dependence. A transition from indirect to quasi-direct energy band gap is observed under compressive strain, which result from the {111} facets induced effect. Analysis of the PDOSs show that the

atoms on the {111} facets in core region is the key factors that make the band gap become quasi-direct gap. Significantly, given the quasi-direct band gap under compressive strain and their band lineup of type II, the core/shell NWs become promising candidates for the high efficiency solar cells，anode materials for batteries and light emission materials.

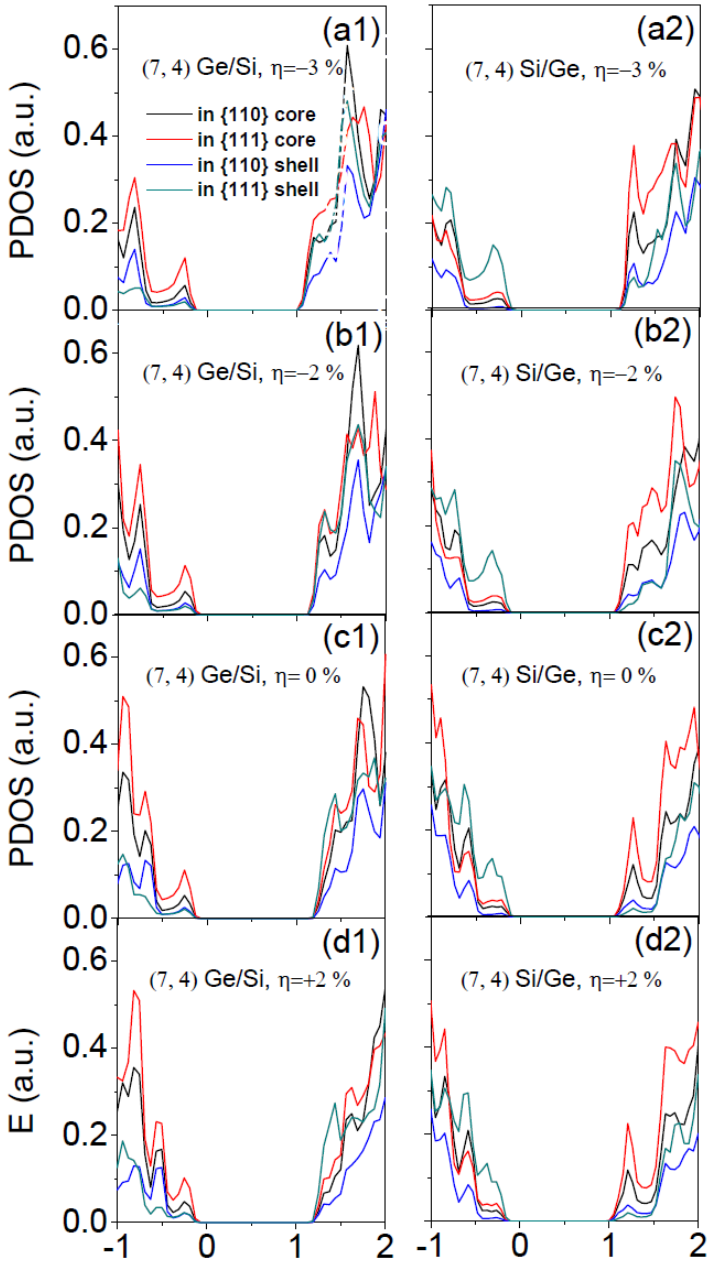

Figure 6.9 PDOSs of the (7, 4) Ge/Si ((a1)-(d1)) and Si/Ge ((a2)-(d2)) core/shell NWs as the function of strain.

References of Chapter 6.2

(1) J Xiang, W Lu, Y J Hu, Y Wu, H Yan, C M Lieber, Nature **2006**, 441, 489.

(2) W Lu, J Xiang, B P Timko, Y Wu, and C M Lieber, PNAS **2005**,102, 10046.

(3) R N Musin and X Q Wang, Phys. Rev. B **2005,** 71, 155318.

(4) R N Musin and XQ Wang, Phys. Rev. **2006**, B 74, 165308.

(5) A Nduwimana, R N Musin, A M.Smith, and X Q Wang, Nano Lett. **2008**, 8, 3341..

(6) D B Migas and E E Borisenko, Phys. Rev. B, **2007**, 76, 035440.

(7) L Yang, R N Musin, X Q Wang, and M Y Chou, Phys. Rev. B **2008**, 77, 19532.

(8) R Peköz and J Y Raty, Phys. Rev. B **2009**, 80, 155432.

(9) M Amato, M Palummo, and S Ossicini, Phys. Rev. B **2009**, 80, 235333.

(10) N Liu, Y R Li, N Lu, Y X Yao, X W Fang, C Z Wang, and K M Ho, J. Phys. D: Appl. Phys. **2010**, 43275404.

(11) L M Doris, B Kedzierski, J Rim K, and M Yang, Science **2004**, 306, 2057.

(12) C W Liu, S Maikap andC Y Yu, IEEE Circuits Devices Mag. **2005**, 21, 21.

(13) X H Peng, and P Logan, Appl. Phys. Lett. **2010**, 96, 143119.

(14) K H Hong, J Kim, S H Lee, and J K Shin, Nano Lett. **2008**, 8, 1335.

(15) Z G Wu, J B Neaton, and J C Grossman, Nano Lett. **2009**, 9, 2418.

(16) D D D Ma, C S Lee, F C K Au, S Y Tong, and S T Lee, Science **299**, 1874 (2003).

(17) Y Wu, Y Cui, L Huynh, C J Barrelet, D C Bell, and C M Lieber, Nano Lett. **4,** 433 (2004).

(18) G Kresse and J Hafner, Phys. Rev. B 47, 558 (1993); G. Kresse and J. Furthmuller, Phys. Rev. B **1996,** 54, 11169; M C Payne, M P Teter, D C Allen, T A Arias, and J D Joannopoulos, Rev. Mod. Phys. **1992**, 64, 1045.

(19) D Vanderbilt, Phys. Rev. B **1990**, 41, 7892.

(20) M Methfessel and A T Paxton, Phys. Rev. B **1989**, 40, 3616.

(21) N Lu, C V Ciobanu, T L Chan, F C Chuang, C Z Wang, and K M Ho, J. Phys. Chem. C **2007**, 111, 7933.

(22) X H Peng, S Ganti, A Alizadeh, P Sharma, S K Kumar, and S K Nayak, Phys. Rev. B **2006**, 74, 035339.

(23) A Hmiel and YQ Xue, Phys. Rev. B 2009, 80, 241410

(24) A J Lu, R Q Zhang, and S T Lee, Appl. Phys. Lett. **2008**, 92, 203109.

(25) C K Chan, H. Peng, G Liu, K Mellwrath, X F Zhang, R A Huggins and Y. Cui, Nat. Nanotechnol. **2008**, 3, 31.

(26) C K Chan, X F Zhang, and Y Cui, Nano Lett. **2008**, 8, 307.

6.3 Aspect ratio modulation effect in [112] Ge/Si core/shell nanowires

6.3.1 Introduction

Nanowires are one of the most interesting nano-structures since they could exhibit the quantum confinement effects (QCE) of the carriers in 2 directions. With different properties from the bulk materials due to the high aspect ratio, they become promising building blocks for the future nanoscale electronics and optical devices, such as field-effecttransistors,photovoltaic cell,sensors and light-emitting diodes.

Silicon nanowires (SiNW) have been extensived studied for several years because of their compatibility of the Si technologies. However,SiNWs are limited by 2 factors: (1) Schottky barriers from the metal contacts; (2) reduced carriers mobility from the dopants. Recently,Si/Ge(Ge/Si) core/shell nanowires have become the focuse of the nanowires community as they could overcome the problems of the pure Silicon NWs. In 2005, Lieber et al [13] presented that low bias ballistic transport can be achieved in Si/Ge (Ge/Si) core/shell heterostructured NWs.

The electronic and optical properties of the Si/Ge (Ge/Si) core/shell nanowires could be modified through precise control of the growth orientation,wires diameters, uniaxial strains and surface passivation. Recent studies showed that both [110] and [112] Si/Ge core/shell nanowires undergo an indirect-to-direct band gap transition under tensile strain [6]. In the present paper, we describe a systematic first principle investigation on the shape-tunable electronic properties of [112] Ge/Si core/shell nanowires. Our calculation indicate that varying the cross sectional aspect ratio could induce an indirect-to-direct band transition.

6.3.2 Methods and Structural Model

The calculation were performed in the framework of density-functional theory (DFT) with the plane-wave based Vienna ab initio package (vasp). The exchange-correlation energy of DFT was treated in the local density approximation (LDA). The ionic potentials are described by Vanderbilt ultra-soft pseudopotentials[18] with periodic boundary conditions. The calculations were done for H-terminated [112] Ge/Si and Si/Ge core/shell NWs so that the surface states are removed from the band gap with hydrogen

passivation. The lattice constants of the tetragonal supercell in the *x*-*y* plane are taken as *a* and *b*, with *c* along the *axial* axis. Plane waves are included up to a kinetic-energy cutoff of 260 eV which is sufficient for both structure optimizations and analysis of the resulting electronic structures. A 1×1×6 Monkhorst-Pack special *k* point grid is used for the Brillouin-zone integration with the Methfessel-Paxton smearing method in the total-energy calculations. The adopted smearing width is 0.1 eV for the structure relaxation and 0.05 eV for the density of states calculations. All atomic positions and lattice constants are optimized using the conjugate gradient method where total energy and atomic forces are minimized. The calculations are converged in energy to 10^{-4} eV. The unit cell is chosen so that the distance between the wires and its replica is more than 10 Å, so that their interactions are negligible[1-4].

In this work, we constructed the (m,n) Ge/Si NWs along [112] direction as the core/shell NWs that has m layers parallel to the {110} facet and n layers parallel to {111} facet. The rectangular cross sectional of the hydrogen passivated (4,7) and (7,4) Ge/Si core/shell NWs are based on the [112] Silicon NW structures found by global unbiased search with genetic algorithm in our previous works, see the inset in Fig. 6.9 (a) and (b) [5-7].

Note that the two structures have the same total number of atoms with $N_{Si}(4,7) = N_{Si}(7,4) = 36$ and $N_{Ge}(4,7) = N_{Ge}(7,4) = 20$, where N_{Si} and N_{Ge} represent the number of Si and Ge atoms. The axial lattice constants of the core/shell NWs are optimized by minimizing the total energy of the NWs with respect to the axial lattice constants c while allowing all atoms in the NWs to relax by the technique of conjugate-gradient. The optimum axial lattice constants for the two structures are listed in Table 6.2. For the two NWs studied in present work, we found that c is 6.83 Å for (4,7) Ge/Si core/shell NW with a diameter (defined as the diagonal length in the cross-section of the NW) of 23.87 Å and c is 6.62 Å for (7,4) one with a diameter of 17.89 Å, as shown in Table 6.2. This implies that the axial and radial expansion for the former is larger than that for the latter although the total number of atoms of the two structures is the same, because interlayer distance between {111} facets is larger than {110} facets.

Table 6.2 Calculated optimized lattice constant c along [112] direction in present work, diameter d of the NWs, effective band gap E_g; m_n^* and m_p^* are predicted effective masses of electron and hole; N_{Si} and N_{Ge} are the number of Si atoms and Ge atoms in the given NWs, respectively. c is the axial lattice constant of one unit cell. d is defined as the largest distance between two atoms in the same cross-sectional plane.

Ge/Si NW	c (Å)	d (Å)	E_g (eV)	m_n^* (m_0)	m_p^* (m_0)	N_{Si}	N_{Ge}	Type of band gap
(4,7)	6.83	23.87	1.71	2.50	-0.41	36	20	direct
(7,4)	6.62	17.89	1.45	0.35	-0.31	36	20	Indirect

6.3.3 Results and discussion

6.3.3.1 Band structures

The electronic band structures of the core/shell NWs from our calculations are plotted in Fig. 6.9 (a) and (b). We pay special attention to the changes of band structure around the Fermi energy level since the cross sectional aspect ratio (n/m) are reciprocal for the (4,7) and (7,4) core/shell NWs and the features of the bands are different from each other although they are oriented along the same direction. For the two structures, both of the two fully relaxed structures have their valence band maximum (VBM) at the Γ point (the center of the Brillouin zone). The conduction band minimum (CBM) is located at the Z point (the boundary of the Brillouin zone) for (7,4) structure, which make the band gap indirect. This means that the (7,4) structure is poor candidate for optoelectronics application. In contrast to the (7,4) one , it is direct band gap in the (4,7) one with the n/m is 4/7, in which its CBM located at the Γ point. The band gaps, which is defined by the energy difference between CBM and VBM, show (as listed in Table 1) that the (4,7) structure with its n/m is 4/7 (<1) has a gap of 1.71 eV while the (7,4) one with its n/m is 7/4 (>1) has 1.45 eV although the diameter of the (4,7) NWs is larger than that of the (7,4) one. Note the n/m of the latter is the reciprocal of the former one. The phenomenon related with n/m is different from the expected general quantum confinement effect that the band gap width increase as the diameter decrease for [100], [110], [111] and [112] Si NWs using density-functional theory, as shown in previous literature[8-10].

It is noted that both of the two NWs have the same number of Si and Ge atoms, say, the contribution from the two atoms to band gap are the same. We conclude a cross sectional aspect ratio dependence of the energy gap transition and band gap of the core/shell NWs. The same characteristics in pure [112] Si NWs were also found by Lu et al.

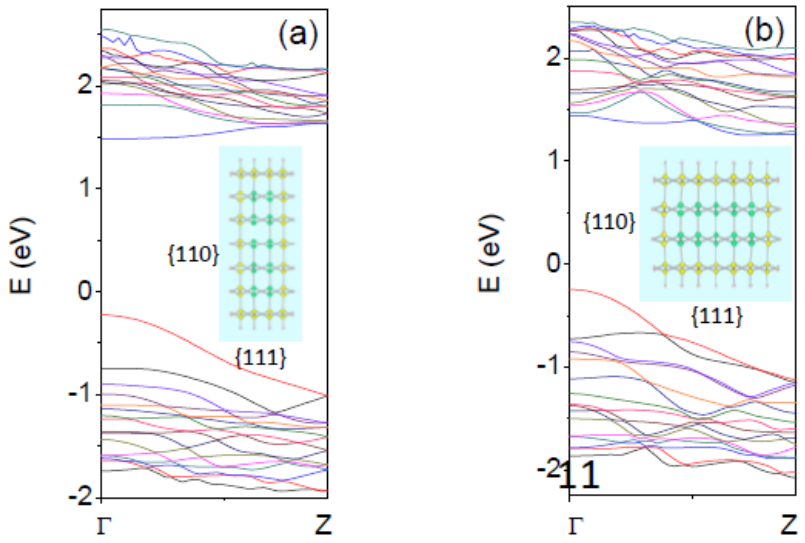

Figure 6.9 Band structures of the Hydrogen passivated (a) the (4,7), (b) the (7,4) Ge/Si core/shell NWs. The insets show the top view of the core/shell NWs. Green (yellow, small pink) balls represents Ge (Si, H) atom

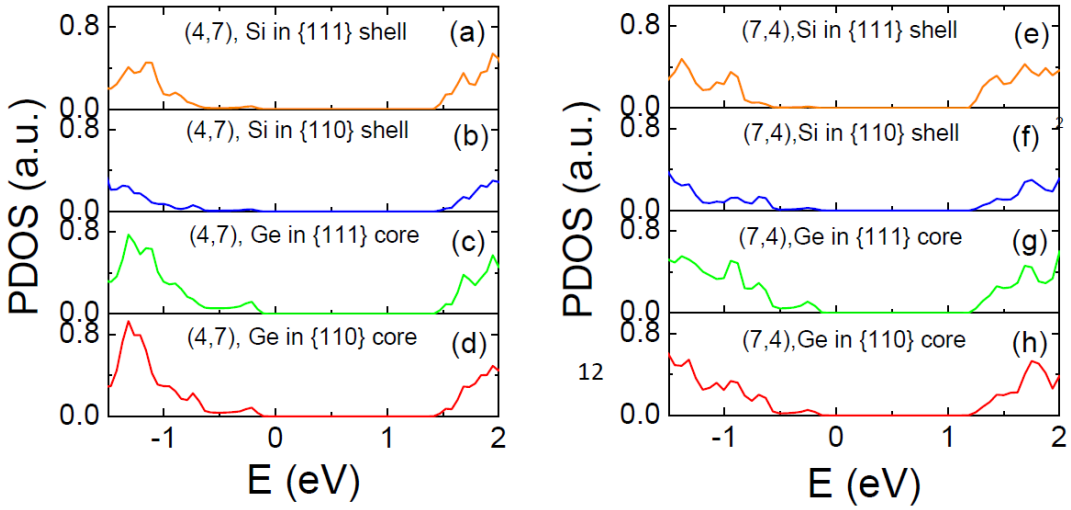

Figure 6.10 Projected density of states of the different atoms in the (4,7) ((a)-(d)) and the (7,4) ((e)-(h)) Ge/Si core/shell NWs.

As one of the two determining factors for the mobility of carriers, the effective masses are also calculated, as shown in Table 6.2, The (4,7) Ge/Si NW, which has an aspect ratio of 4/7 that is smaller than 0.58, has much larger effective masses of electron than the (7,4) one. While the effective masses of the holes is a bit bigger than that of (7,4) one, which is close to the heavy hole effective mass of bulk Ge value ($0.34m_0$). also reported the similar properties for the [111] and [110] oriented Ge/Si NWs. It indicate that the (4,7) NW with the n/m<0.58 is suit for the application of p-channel materials but not n-channel one

since the mobility of electrons could be small. Thus, the effective masses prove to be sensitive to cross sectional aspect ratio.

6.3.3.2 Density of states

The Projected Density of states (PDOSs) are decomposed further with respect to the atomic orbitals of each atom on the {110} and {111} facets in order to understand the physical mechanism of the band structures, as shown in Fig. 6.10. We find two obvious features exit in PDOSs near the CBM: (i) for each of the NWs we studied, the PDOS of the atom in shell region on the {110} facet are lower than that in the core region on the same facet; Both core and shell atoms on the {111} facets have almost equal contribution to the CBM, and stronger than that on the {110} facet, (ii) also importantly, the PDOS of the atom in shell region on the {110} facet in (4,7) NW is lower than that in the (7,4) NW; furthermore, the PDOS of the atom in core region on the {110} facet in the (4,7) NW is also lower than that in the (7,4) NW. Other study found only the surface atoms on {110} facets play the role in pure [112] Si NW.

It implies that this is the differences that control (decide) the band gap transition between core/shell NWs and pure NWs. Noting that there are structural difference between the two NWs in which the (4,7) NW have more Si and Ge atoms along {110} facets than the (7,4) one. It is obviously that the atoms along {110} facets are the key factors that make the CBM of the (4,7) NW at the Γ point and the (7,4) NW at the Z point. In another words, the direct band gap of the (4,7) NW mainly comes from the electronic states of the Si and Ge atoms on {110} facets. Therefore, the {110} facets induced effect are the predominant factor of making the cross sectional aspect ratio dependence of the type of the band gap and band gap. This is a remarkable and unique property of [112] Ge/Si core/shell NWs in electronic band structures.

6.3.3.3 Band offsets and spatially charge distribution

To gain more insights into the contributions of the atoms to the CBM and VBM and the origin of the charge separation in the real space, we show the distribution of the charge densities for the electronic states of CBM and VBM at an isovalue of 0.002e on the cross-section of the NWs in Fig 6.11. The charge densities arising from the VMB and CMB localized on Ge region (Fig 6.11 (a) and (c)) and Si region (Fig. 6.11 (b) and (d)), respectively. In one words, electronic states near VBM are mainly located in the Ge

region while the states near CBM reside in the Si region. When electrons in VBM are excited, the charge separation will take place in a way that one-dimensional electron gas (1DEG) are located in the shell part of Si atoms and the one-dimensional hole gas (1DHG) are distributed in the core region on Ge atoms. The spatial distribution of 1DEG and 1DHG in quantum wells strongly suggest that the band edge alignment of the quantum wells of Ge/Si NWs is $E_c^{Ge} > E_c^{Si}$ and $E_v^{Ge} > E_v^{Si}$, which agrees with the band offset of bulk Si and Ge. The Ge/Si core/shell NWs we studied is therefore the type II staggered band offset which is similar to our previous work for the (7,4) and (9,4) Ge/Si and Si/Ge structures along [112] orientation , Ge/Si core/shell NWs in cylindrical sharp along [111] and [100] direction and diamond shape along [110] direction.

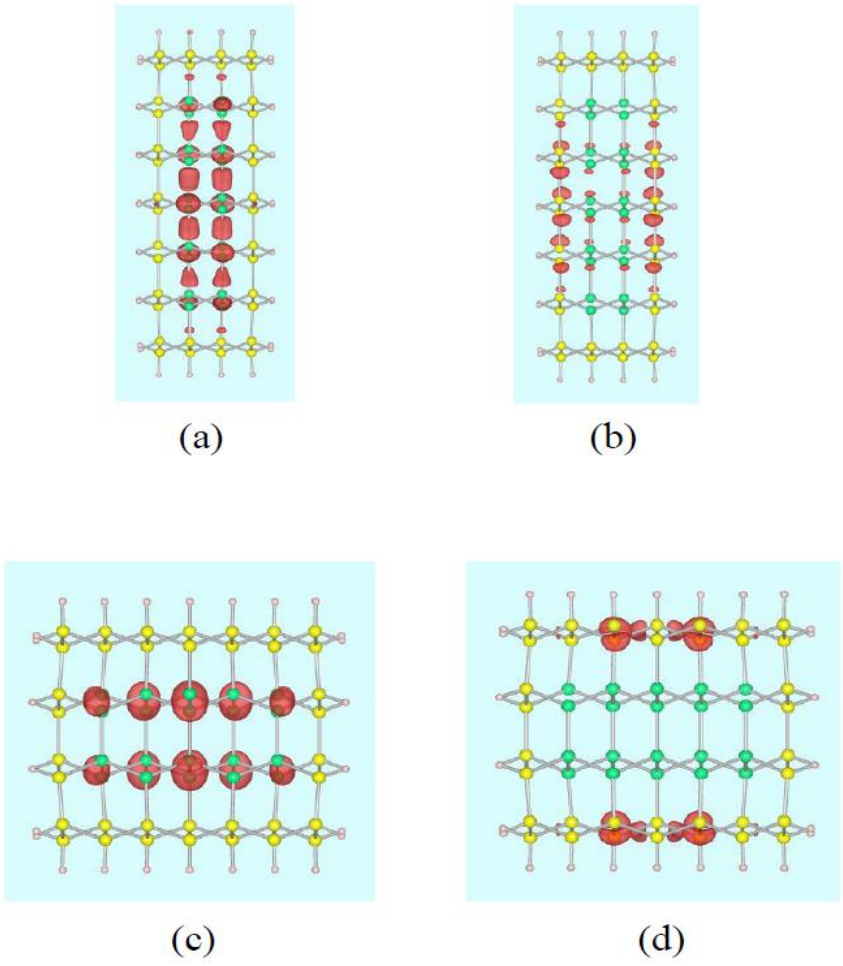

Figure 6.11 Cross sectional view of the distribution of charge density plots at the isovalue of 0.002e of the (4,7) ((a) and (b)) and the (7,4) ((c) and (d)) core/shell NWs. (a) and (c) the top of valence band, (b) and (d) the bottom of conduction band, respectively. Green balls are Ge atoms, yellow balls are Si atoms and pink small balls are H atoms.

It is observed [12] that the electronic states in the (7,4) Ge/Si NW are strongly localized in the quantum wells. However, some of the electronic states in the (4,7) Ge/Si NW spill out of the quantum wells, as shown in Figure 6.11. It implies that the depth of the quantum well (ΔE_c and ΔE_v) in the (7,4) structure is deeper than that in the (4,7) one. According to the difference of the charge localization between the (4,7) and (7,4) NWs, it comes out that the relationship of the band offset between the two NWs are $\Delta E_c(4,7) < \Delta E_c(7,4)$, while $\Delta E_v(4,7) < \Delta E_v(7,4)$. In other words, the quantum confinement effect in the (7,4) structure is stronger than that in the (4,7) one. The results make it clear that the charge localization in the core/shell NWs depend on the cross sectional aspect ratio.

Based upon the analysis, the separation of charges in the NWs can be used in solar cell since there are fewer bulk recombinations than in traditional p-n junction. Moreover, the direct band gap of (4,7) NW is valuable because the carrier collection efficiency in solar cell is much higher than that of (7,4) with indirect band gap due to the fact that there is not phonon scattering participating in the transition in (4,7) NW. On the other hand, p-channel devices could be made with this Ge/Si core/shell NWs because the type II band lineups make it possible that the concentration of holes in the core region can be controlled by p-type doping in shell region in modulation doping field effect transistors. Thus, the high mobility of holes can be realized due to the great reduction of scattering from the charged dopants, since the charged dopants in the shell region can be separated from the holes spatially. It is worth noting that there is a contrivance that the (4,7) structure has a direct band gap while has lower quantum well depth in energy than the (7,4) one, which limit its application in optoelectronic application since the lower quantum well depth would reduce the quantum confinement effect of the carriers in the well.

6.3.3 Conclusion

In summary, we have studied two possible Ge/Si core/shell NWs along [112] direction modulated by the cross-sectional aspect ratio based on first-principles calculations. It is found the aspect ratio induced effect control the type of band gap, the width of band gap and the depth of the quantum wells for NWs. The band gaps are found to be direct with width of 1.71 eV for [4,7] core/shell NW and indirect with width of 1.45 eV for [7,4] one. A detailed analysis of PDOS suggests that the contributions from {110} facet plays an important role in determining the electronic properties. This property is of great importance in the semiconductor process in that we could control the band gap and the quantum well depth in these NWs with type II band offset, and we could further modulate the concentration of carriers in the Ge atoms side by p-type doping in Si atoms side. The application of the NWs as high efficiency solar cells and high mobility of holes

References of 6.3

[1] G Kresse and J Hafner, Phys. Rev. B 47, 558 (1993); G. Kresse and J. Furthmuller,

[2] M C Payne, M P Teter, D C Allen, T A Arias, and J D Joannopoulos, Rev. Mod. Phys. 64, 1045 (1992).

[3] D Vanderbilt, Phys. Rev. B 41, 7892 (1990).

[4] N Lu, C V Ciobanu, T L Chan, F C Chuang, C Z Wang and K M Ho, 2007 J. Phys. Chem. C 111,7933

[5] N Liu, Y R Li, N Lu, Y X Yao, X W Fang, C Z Wang, and K M Ho, J. Phys. D: Appl. Phys. 43 275404 (2010)

[6] N Liu, N Lu, Y X Yao, Y R Li, C Z Wang, and K M Ho, (2010)submitted.

[7] X Y Zhao, C M Wei, L Yang, and M Y Zhou, Phys. Rev. Lett. 92,236805 (2004)

[8] A J Read, R J Needs, K J Nash, L T Canham, P D J Calcott and A Qteish, 1992 Phys. Rev. Lett 69,1232

[9] L Huang, N Lu, J A Yan, M Y Chou, C Z Wang and K M Ho, J. Phys. Chem. C 112,15680 (2008)

[10] A J Lu, R Q Zhang, and S T Lee, Appl. Phys. Lett. 92, 203109 (2008).

[11] G Dresselhaus, A E Kip, and F Qyafuso, Phys. Rev. 98, 368 (1995).

[12] R Peköz and J Y Raty, Phys. Rev. B 80, 155432 (2009).

[13] Lu W, Xiang J, Timko B P, Wu Y and Lieber C M 2005 *Proc.Natl Acad. Sci. USA* **102** 10046

ACKNOWLEDGEMENT

I would like to take this opportunity to express my appreciation to those who helped me with research and the writing of this thesis. First and foremost, Prof. Kai-Ming Ho and Dr. Cai-Zhuang Wang for their guidance, patience and support throughout my 7 years' research. I have benifited a lot from their erudite academic levels and conscientious research attitude. I would also thank Dr Tzu-Liang Chan, Dr Feng-Chuan Chuang, Dr Min Ji and Dr Shaogang Hao for sharing valuable experiences and opinions and being open-minded friends.

My gratitude also goes to Prof Robert Mcqueeney, Prof. Adams Kaminski, Prof. Curtis Struck and Prof. Matthew Kramer for serving as my graduate committee members and giving valuable reviews to my research and study. I would also like to give thanks to Prof. Pat Thiel for the experimental results and Dr Cristian Ciobanu for sharing discussion. I additionally thank all members in our group for all their help. They are Yongxin Yao, Maozhi Li, Li Huang, Nuo Liu, Xiaowei Fang, Shunqing Wu, Jian Zhang, Xiaojie Liu and Guiping Zhang.

I'm grateful to my parents, Lili Peng and Ms Yiying Ye. Without their support and encouragement, I would not have been able to come so far.

This work ws performed at Ames Laboratory operated for the US Department of Energy by Iowa State University under Contract No DE-AC02-07CH11358.